The flow in viscous Taylor droplets

PIV in microscopic two-phase flow

Miessner, U.P.

DOI
10.4233/uuid:19d23974-a28b-4061-901c-b92475afad0e

Publication date
2021

Document Version
Final published version

Citation (APA)
Miessner, U. P. (2021). *The flow in viscous Taylor droplets: PIV in microscopic two-phase flow*. [Dissertation (TU Delft), Delft University of Technology]. https://doi.org/10.4233/uuid:19d23974-a28b-4061-901c-b92475afad0e

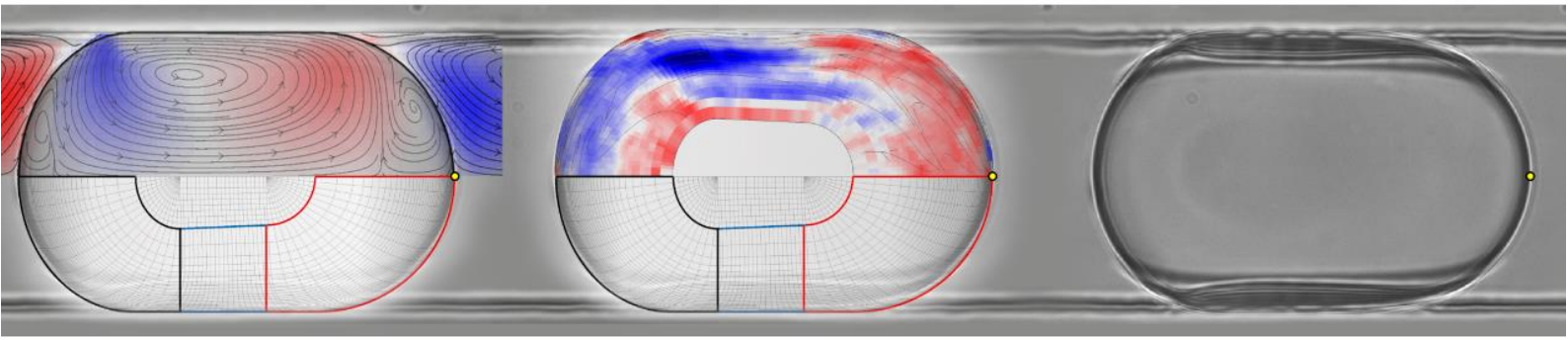

The flow in viscous Taylor droplets

PIV in microscopic two-phase flow

Ulrich Mießner

The flow in viscous Taylor droplets

PIV in microscopic two-phase flow

Dissertation

for the purpose of obtaining the degree of doctor
at Delft University of Technology
by the authority of the Rector Magnificus Prof.dr.ir. T.H.J.J. van der Hagen
chair of the Board for Doctorates
to be defended publicly on
Tuesday 1 June 2021 at 12:30 o'clock

by

Ulrich Peter MIEßNER

Diplom-Ingenieur, Universität Bremen, Germany
born in Bremen, Germany

This dissertation has been approved by the promotor.

Composition of the doctoral committee:

Rector Magnificus	chairperson
Prof. dr. ir. J. Westerweel	Delft University of Technology, promotor

Independent members:

Prof.Dr.-Ing. R. Lindken,	Hochschule Bochum, Germany
Prof.Dr.-Ing. J. Hussong,	TU Darmstadt, Germany
Prof.dr.ir. J.T. Padding,	Delft University of Technology
Prof.dr. P. Angeli,	U. College London, United Kingdom
Prof.dr.ir. C.R. Kleijn,	Delft University of Technology

The work presented in this thesis was supported financially by MicroNed: (Fluorescence on a Chip, WP II-F-3).

Keywords: Taylor flow; Taylor droplet; μPIV; interface shape; rectangular microchannel; excess velocity; pressure; energy loss

Printed by: Ridderprint | www.ridderprint.nl.

Front & Back: The evolution of investigating viscous Taylor droplets

ISBN 978-94-6416-636-1

An electronic version of this dissertation is available at `http://repository.tudelft.nl/`.

Lieke, Jan, Knud und Swantje

Preface

This thesis is based on experimental work performed at the Laboratory for Aero- and Hydrodynamics (Delft Technical University, Netherlands) from August 2005 to December 2009. The modeling work evolved later during the employment at the University of Bremen, Germany. Three reviewed articles directly arose from the combined work and represent the main contributions to this thesis:

- Mießner, U., Helmers, T., Lindken, R., Westerweel, J. An analytical interface shape approximation of microscopic Taylor flows. Exp Fluids 60, 75 (2019).
  https://doi.org/10.1007/s00348-019-2719-0

- Mießner, U., Helmers, T., Lindken, R., Westerweel, J. μPIV Measurement of the 3D velocity distribution of Taylor droplets moving in a square horizontal channel. Exp Fluids 61, 125 (2020).
  https://doi.org/10.1007/s00348-020-02949-z

- Mießner, U., Helmers, T., Lindken, R., Westerweel, J. Experimental investigation of the 3D pressure field of Taylor droplets moving in a square horizontal microchannel. Exp Fluids 62, 83 (2021).
  https://doi.org/10.1007/s00348-021-03189-5

The Chapters 4 (Modeling the Taylor droplet interface), 5 (Flow field of a viscous Taylor droplet) and 6 (Pressure field and energy dissipation) directly cite the introductions, results and discussions and the conclusions sections of the respective above-listed articles. However, all three papers are based on the same theory and set of measurements and therefore rely on identical methods and evaluation procedures. Thus, the Chapters 2 (The fluid mechanics of Taylor droplets) and 3 (Materials and methods) merge the according sections of the papers. The first Chapter 1 (Introduction) is based on the abstracts and introduction the three above listed articles. It connects the three papers,

provides the motivation and context of the work. The last Chapter 7 (Main conclusions and outlook) restates the important findings and provides an outlook on how to proceed with the results of this work.

Summary

Digital microfluidics emerged and established over the last 20 years. The scope of applications ranges from pharmaceutical to biological, chemical and even thermal processes. The practical use of Taylor droplets as individual reaction chambers, mixing vessels or simply as transportation vehicles on process engineered microfluidic devices allows for precise control and process intensification of precious materials or sparse samples. Despite this widespread use of Taylor droplets, some of the fundamental physics of this flow have not been investigated experimentally.

Continuous Taylor droplet chains in long rectangular microchannels exhibit a fluctuation of the droplet length, the droplet shedding frequency and the droplet velocity. The fluctuation of the droplet velocity is connected to the droplet length distribution in the Taylor flow. As a driving force for the difference between the droplet velocity and the mean flow velocity a pressure gradient is predicted that is inverted with respect to the main flow direction.

A multiplane approach of conventional μPIV is chosen to accurately measure and reconstruct the 3D3C velocity field and the 3D pressure distribution inside and outside of a mean quasi-stationary Taylor droplet. A new methodology to asynchronously record, extract and compile μPIV raw-images of a pulsating two-phase flow has been developed successfully to overcome the severe influence of the droplet length fluctuation.

An analytical interface shape approximation has been developed and verified, that allows to estimate the position of the motion-deformed dynamic Taylor droplet interface. This geometrical model uses the Laplace pressure between the Taylor droplet interface at rest and a moving droplet to deliver a quantitative relation between the flow related deformation of the caps and the geometry of the bypass flow of the droplet. Additionally, the interface

approximation serves as a projection surface to visualize and investigate the derived flow quantities.

The 3D velocity information allows the detailed investigation of the 3D flow features such as stagnation regions and the shear rate distribution. The maximum shear rate is located at the entrances and exits of the wall films and at the corner flow (gutter) bypassing the Taylor droplet. The regions of high strain correspond to the cap positions of the Taylor droplets. This experimental data set allows visualization of the streamlines of the velocity distribution on the interface of a Taylor droplet and to directly relate it to the main and secondary vortices of the droplet phase velocity field.

The 3D pressure field is derived and divided into a wall-proximate layer and a core-flow to describe the phenomenology. At the wall, the pressure decreases expectedly in downstream direction. In contrast, a reversed pressure gradient is present in the core of the flow as predicted. It drives the bypass flow of the continuous phase through the corners and causes the Taylor droplet's relative velocity between the faster droplet flow and the slower mean velocity of the flow. Based on the pressure field the driving pressure gradient of the bypass flow is quantified and verified with a simple estimation method: the geometry approximation of the gutter entrances delivers a Laplace pressure difference.

As a direct measure for the viscous dissipation, the 3D distribution of work done on the flow elements is calculated. It represents the necessary work to maintain the stationarity of the Taylor flow. The spatial integration of this distribution provides the overall dissipated energy and allows to identify and quantify different contributions of the individual fluid phases, from the wall-proximate layer and from the flow redirection due to presence of the droplet interface.

The work presented in this thesis provides detailed insight into the into the physics of viscous Taylor flow based on experimentally acquired 3D3C velocity data. The 3D3C velocity field, the 3D pressure field, the 3D distribution of work as well as the approximate interface model are supplied as electronic supplementary material of the publications to the fluid mechanics community to enable a benchmark for CFD and numerical simulations.

Samenvatting

Digitale microfluïdica is de afgelopen 20 jaar ontstaan en ontwikkeld. Het toepassingsgebied varieërt van farmaceutische tot biologische, chemische en zelfs thermische processen. Het praktische gebruik van Taylor-druppels als individuele reactiekamers, mengvaten of gewoon als transportvoertuigen op door het proces ontwikkelde microfluïdische apparaten maakt nauwkeurige controle en procesintensificatie van kostbare materialen of schaarse monsters mogelijk. Ondanks dit wijdverbreide gebruik van Taylor-druppels, is een deel van de fundamentele fysica van deze stroom niet experimenteel onderzocht.

Continue Taylor-druppelketens in lange rechthoekige microkanalen vertonen een fluctuatie van de druppellengte, de frequentie van druppel generatie en de druppelsnelheid. De fluctuatie van de druppelsnelheid hangt samen met de druppellengteverdeling in de Taylor-stroom. Als drijvende kracht voor het verschil tussen de druppelsnelheid en de gemiddelde stroomsnelheid wordt een drukgradiënt voorspeld die omgekeerd is ten opzichte van de hoofdstroomrichting.

Een multi-vlakken benadering van conventionele μPIV is gekozen om nauwkeurig het 3D3C-snelheidsveld en de 3D-drukverdeling binnen en buiten een gemiddeld quasi-stationaire Taylor-druppel te meten en te reconstrueren. Een nieuwe methodologie voor het asynchroon opnemen, extraheren en compileren van onbewerkte PIV-beelden van een pulserende tweefasenstroom die met succes is ontwikkeld om de invloed van de fluctuatie van de druppellengte te overwinnen.

Er is een analytische interface-vormbenadering ontwikkeld en geverifieerd, waarmee de positie van de bewegingsvervormde dynamische Taylor-druppel grensflakte kan worden geschat. Dit geometrische model gebruikt de Laplace-druk tussen het Taylor-druppel gresflakte in rust en een bewegende druppel

om een kwantitatieve relatie te leveren tussen de stroomgerelateerde vervorming van de doppen en de geometrie van de bypassstroom van de druppel. Bovendien dient de grensflakte benadering als een projectieoppervlak om de afgeleide grootheden te visualiseren en te onderzoeken.

De 3D-snelheidsinformatie maakt gedetailleerd onderzoek mogelijk van de 3D-stromingskenmerken zoals stagnatiegebieden en de verdeling van de afschuifsnelheid. De maximale afschuifsnelheid bevindt zich bij de in- en uitgangen van de grenslaag an de en bij de hoekstroom die de Taylor-druppel omstroomd. De gebieden met hoge spanning komen overeen met de dop-posities van de Taylor-druppeltjes. Deze experimentele dataset maakt visualisatie mogelijk van de stroomlijnen van de snelheidsverdeling op het grensvlakte van een Taylor-druppel en om deze direct te relateren aan de hoofd- en secundaire wervels van het snelheidsveld van de druppelfase.

Het 3D-drukveld wordt afgeleid en verdeeld in een laag in de buurt van de muur en een kernstroom om de fenomenologie te beschrijven. Bij de muur neemt de druk naar verwachting af in stroomafwaartse richting. Daarentegen is, zoals voorspeld, een omgekeerde drukgradiënt aanwezig in de kern van de stroom. Het drijft de bypass-stroom van continue fase door de hoeken en veroorzaakt de relatieve snelheid van de Taylor-druppel tussen de snellere druppelstroom en de langzamere gemiddelde snelheid van de stroom. Op basis van het drukveld wordt de aandrijvende drukgradiënt van de bypassstroom gekwantificeerd en geverifieerd met een eenvoudige schattingsmethode: de geometrische benadering van de bypass-ingangen levert een Laplace drukverschil op.

Als directe maat voor de viskeuze dissipatie wordt de 3D-verdeling van het werk op de stromingselementen berekend. Het vertegenwoordigt het noodzakelijke werk om de stationariteit van de Taylor-stroom te behouden. De ruimtelijke integratie van deze verdeling zorgt voor de totale gedissipeerde energie en maakt het mogelijk om verschillende bijdragen van de vloeistoffasen, van de grenslaag en van de stroomomleiding door de aanwezigheid van het druppelgrensvlakte te identificeren en kwantificeren.

Met het werk dat in dit proefschrift wordt gepresenteerd, wordt gedetailleerd inzicht verschaft in de fysica van viskeuze Taylor-stroming op basis van experimenteel verkregen 3D3C-snelheidsgegevens. Het 3D3C-snelheidsveld,

het 3D-drukveld, de 3D-werkverdeling en het benaderende grensflaktemodel worden als elektronisch aanvullend materiaal van de publicaties aan de stromingsleer-gemeenschap geleverd om een benchmark voor CFD en numerieke simulaties mogelijk te maken.

Contents

1 Introduction

Once there was a particle
It looked quite nice - just optical
Denied to move - unworkable
No push nor pull observable
It wouldn't move - that barnacle

This thesis addresses the fluid mechanics of viscous Taylor droplets in rectangular microchannels. This confined two-phase flow is established as a regular distribution of individual droplets translating in a steady droplet chain separated by compartments of continuous phase (Fig. 1.1). The droplets investigated in this work feature a thin film of bulk phase fluid prevents the droplet phase from contacting the wall.

An early application of small confined droplets or bubbles were flow meters. In channels of circular cross-section, the bubble is assumed to block almost the entire-cross section of the channel without fluid bypassing the bubble. Thus, the bubble velocity is used as a measure for the mean flow velocity. However, a thickening wall film establishes at rising viscous forces which

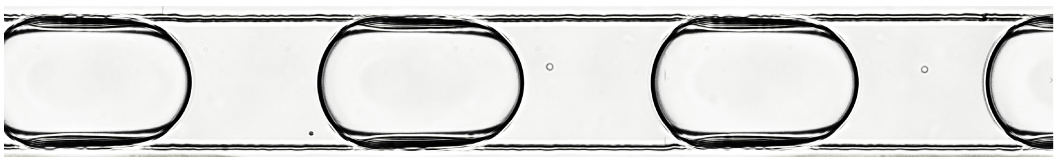

Fig. 1.1: Taylor droplets (water/glycerin mixture dispersed in 1-octanol) in a microchannel of $104\,\mu\mathrm{m}$ by $96\,\mu\mathrm{m}$ width and height. The surface tension forces dominate the viscous forces ($Ca_\mathrm{c} = 0.005$) and Stokes-flow conditions apply ($Re_\mathrm{c} = 0.051$)

needs to be accounted for. Fairbrother and Stubbs (1935) [27] delivered an empirical relation that describes the effect of the lubricating film at very low viscous forces in circular capillaries. Taylor (1961) [111] has significantly expanded investigations into the drops named after him. He extended the range of available measurements to more pronounced viscous forces and postulated a re-circulating vortex in the continuous phase. In the same year Bretherton (1961) [15] used lubrication analysis to describe the film formation at the transition region between the front cap of the droplet and the established film along the droplet body. The outcome of Taylor's and Bretherton's work was applied decades later to design complex multi-phase flow devices on the micro-scale.

Anticipating the importance of an emerging field of research, Feynman presented in 1959 [29] one of the first considerations of the potential of nano- and microtechnolgy. In the following decades, new ways of surface structuring evolved - mainly for production of electronic circuitry (Micro-Electro-Mechanical Systems - MEMS) and optics (Micro-Opto-Electro-Mechanical Systems - MOEMS). Emerging methods like photolithography, electroplating and molding opened the door for the development of modern microfluidic equipment. The idea to integrate complex dedicated laboratory processes onto miniaturized devices lead to the evolution of "lab-on-a-chip" (LOC) concepts and ultimately to the translation of entire analytic process sequences towards "micro total analysis systems" (μTAS). It is the lithographic nature of the production process of these microfluidic devices, that results the typical nearly rectangular shape of the microchannel cross section of these systems.

The term microfluidics refers to the research on and the technology of fluid handling in channels of microscopic dimensions. The geometric size of the structures ranges between $1\,\mu\mathrm{m}$ and $1\,\mathrm{mm}$. With microfluidic approaches sample volumes of femtoliter-size can be precisely handled [18, 106, 122] and processed. The translation of unit operations and unit processes into the micro-scale is called micro process engineering. In order to reliably analyze a series of samples of different origin or property, samples need to be kept separate from each other to avoid cross-contamination. One obvious solution to this issue is the usage of individual droplets and bubbles, which is referred to as digital microfluidics or microscopic multiphase flows. An extensive

overview on the evolution of microfluidics and the use of two-phase flow is given by Shang et al. [104].

In order to build a reliable analytic platform applying digital microfluidics, it is of major interest to keep the process properties constant. The comparability of individual flow segments is affected by the equality of the geometric and hydrodynamic conditions of individual droplets. The amount of segment volume, the magnitude of the available interface area and the adjoining flow fields strongly influence the gradients of the driving forces for heat and mass transfer.

Despite Taylor flows being simple to establish and easy to apply, the hydrodynamic interaction inside Taylor droplet chains is complex. The self-organized droplet and bubble formation and their subsequent motion through the microchannels are essentially pressure dependent. Compared to a single-phase flow of the same length, individual droplets or bubbles exert an increased pressure drop to the microchannel outlet [125] that rises with droplet length [46].

Given a fixed total pressure gradient that drives the flow through the channel, each droplet adds a length-specific pressure loss to the outlet channel. The elevated pressure loss in the outlet, causes a gradual formation of smaller droplets with each newly generated droplet that enters the outlet. Shorter droplets indeed cause less pressure loss but they have the tendency to translate faster through the channel than the average speed of the Taylor flow [41]. In extreme cases, when the pressure in the outlet is too high, the inflow of disperse phase is even stopped and recommences only after sufficient droplets have vacated the channel to allow for new droplets to be generated. Thus, depending on the microchannel length, an ascending number of droplets sensitively feedback on the formation [81] and cause a droplet size distribution and a residence time distribution [32].

This thesis intends to add a substantial step towards a better understanding of the physics of Taylor flows in rectangular microchannels. Experimental fluid dynamics has been chosen over a computational fluid dynamics (CFD) approach to establish well investigated reference data that provides a starting point for parameterized numerical simulations. A model for the approximation of the dynamic interface shape of moving Taylor droplets (Chap. 4)

allows to visualize and investigate physical quantities of the flow directly at the interface position and relates its deformation to the individual flow conditions. The experimentally measured data set of the flow field (Chap. 5) allows to derive the pressure field (Chap. 6) of an average droplet in the flow. The results of this thesis may improve the reactor design and operation for digital microfluidics and can be used as benchmark data for CFD-Studies.

1.1 Motivation

The resources of our planet are restricted. The unworried consumption-oriented way of satisfying mankind's needs already threatens the functionality of our biosphere. The coupled gaseous, liquid and solid emission streams interact with the ecological balance of our habitat [44]. From a process engineering perspective, the dissipation of energy and consumption of material resources is a key issue to address, when transforming our economic and ecological conduct into a sustainable development.

One technological way to address this issue is process intensification, which is defined as the targeted improvement of processes at the unit operations, tasks and phenomena level in order to increase process efficiency and improve sustainability [33]. The design and usage of innovative operating conditions or the combination of simultaneous physical (e.g. mixing) and chemical processes (reaction) aims at faster global kinetics [7]. Here, global reaction kinetics refer to the integral reaction kinetics of a entire unit process, where the intrinsic reaction rates of the educts is usually masked by e.g. limitations in mass transfer due to mixing inefficiency. In this context, well-controlled processes are essential e.g. to handle chemical reactions in their optimal operational window.

Constant isothermal conditions at the reaction optimum promote maximum yield and selectivity. In conventional macroscopic processes, reactor dimensions are on the scale of centimeters to several meters. In these larger reaction volumes a high reaction enthalpy causes temperature gradients that deviate from the isothermal ideal and decrease the yield. The resulting inefficient processes strongly increase the downstream processing effort to separate the main from the side-products.

Microscopic process engineering delivers an entire toolbox of effects and methods, that proved to be well-suited for process intensification [58]. It applies constrained flows of gases and liquids on a small scale. Unit operations and processes are realized on length scales of the flows that range typically between $1\,\mu\mathrm{m}$ and $1\,\mathrm{mm}$. Rather than miniaturization of the process, it is the objective of micro process engineering to use the striking physical advantages that arise from the application of processes on such small scales: small economical sample volumes, well-controlled laminar flow conditions, high surface to volume ratio and short diffusion and conduction distances. The latter advantages provide excellent precise mixing and promote heat and mass transfer [12] to achieve the desired optimal reaction conditions. They are the key to access process intensification potentials.

A major fraction of industrial processes involves multiphase flows. Thermodynamically, a phase is defined as a continuum of homogeneous properties – a gaseous, solid or liquid phase. Thus, multiphase flows necessarily consist of two or more immiscible simultaneously flowing phases. Multiphase flows in microchannels exhibit a variety of flow patterns (Fig. 1.2 a-h). The flow patterns can be observed in capillaries with vertical as well as in horizontal orientation, in circular as well as in rectangular microchannels. All flow patterns occur in pressure driven as well as in volume flow driven set-ups [118]. In this choice of flow patterns the Taylor flow stands out since it provides individually addressable reaction compartments with the continuous phase slugs separating individual droplets and a thin lubricating wall film preventing the contact between the wall and the disperse phase. The Taylor flow meets the required predictability and definiteness of intensified processes best.

Applications of droplet microfluidic approaches employ two-phase flows using either the continuous phase or the disperse phase of Taylor flows to implement thermal [52, 67, 76], chemical [35, 60, 66, 110], biological [69, 79, 123] or medical [53] processes. Taylor flows enable precise handling of small sample volumes [30, 122] and Seemann et al. [103] propose the application of Taylor droplets as consequtive encapsulated process vessels to enable high-speed processing and circumvent cross-contamination. Chou et al. [22] published a overview on Taylor flow applications.

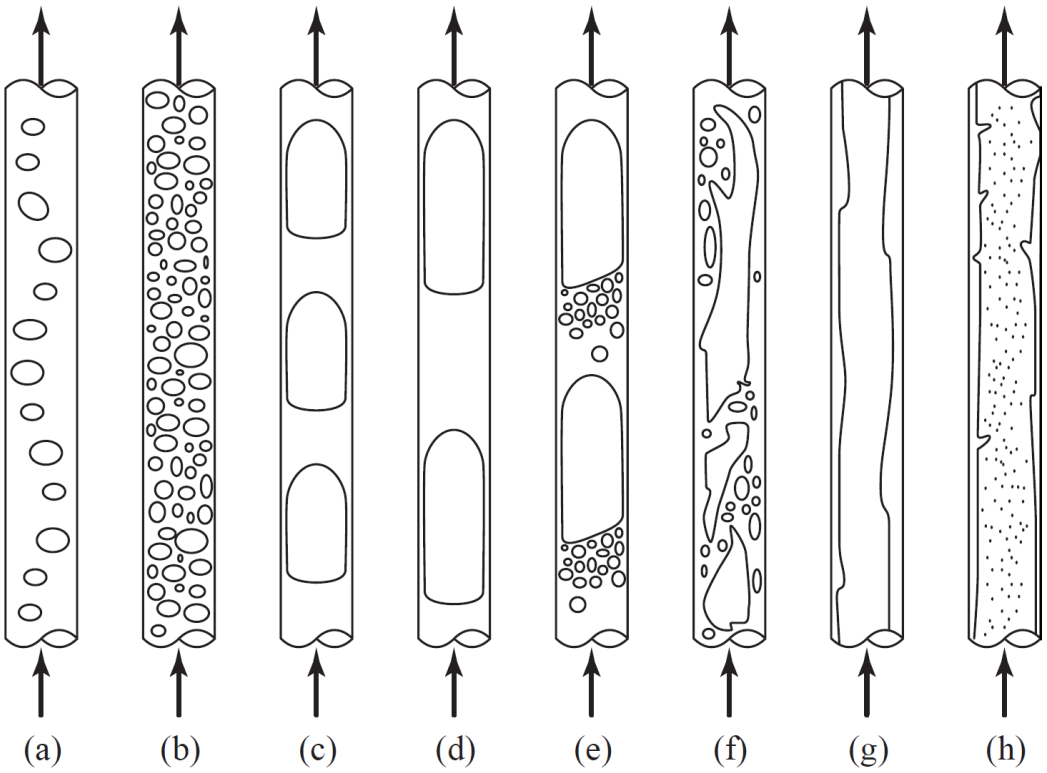

Fig. 1.2: Sketch of observed flow patterns in capillary channels. (a,b): bubbly flow, (c,d) segmented flow (a.k.a. bubble train flow, Taylor flow, capillary slug flow), (e) transitional slug/churn flow, (f) churn flow, (g) film flow (downflow only), (h) annular flow. Reprinted from Kreutzer et al. (2005) [60] with permission from Elsevier

Constant stable optimal process conditions in microfluidics are the key to achieve process intensification. Driving a quasi-stationary Taylor flow requires a profound understanding the interaction of convection-advection conditions inside and outside the Taylor droplets. Comprehension of the hydrodynamics enables to control the flow, narrow the residence time distribution, distribute the flow evenly in a network of channels, and to adjust the extent of available interface area for heat and mass exchange.

1.2 Objectives and scope

Microchannel fabrication often necessitates the realization of Taylor flows in rectangular cross section geometries. The channel structures are integrated in microfluidic chips, that facilitate pressure driven flows. The entire droplet chain accumulates a total pressure drop from the generation to the microchannel outlet: each unit of slug and droplet experiences an individual local driving pressure field in the frame of reference of a single droplet in that chain.

Besides the lubricating wall films, Taylor flows in rectangular microchannels feature a bypass flow through the continuous phase-filled corners [60], the gutters [107]. Depending on the flow conditions, this flow through the gutters (Fig. 2.3) causes the Taylor droplet velocity to deviate significantly (up to $\pm 30\%$) from the mean velocity of the flow [41, 50]. The droplets are slower than the average flow velocity e.g. if de-wetting occurs at the wall films [62] and the proceeding three-phase contact line adds additional restraining forces to the droplet motion. The droplet can only be faster than the mean velocity if the local pressure gradient along the Taylor droplet is reversed with respect to the overall flow direction, i.e. continuous phase is transported from the frontal slug of the droplet to the slug on the back [3]. A thoroughly conducted measurement of the 3D-flow field inside and outside of a Taylor droplet would allow to investigate the volume flow through the gutters and to derive the driving pressure field.

The locally inverted pressure gradient also affects the shape of the droplet. In a microscopic channel, the shape of a static confined droplet at rest emerges due to the energy minimization of the interface. Any flow will exert forces

on the interface and causes the droplet to dynamically deform. The flow-related dynamic deformation of Taylor droplets is experimentally observed by Sauzade and Cubaud [101] and Helmers et al. [40] and qualitatively explained by Abiev [3].

Controlling the behavior of droplets in a Taylor flow needs thorough understanding of the pressure field of the individual Taylor droplet. The pressure field of Taylor droplets

- causes the convection in the flow supporting heat and mass transfer.
- drives the inner and outer flow field, and with them e.g. the shear stresses on fragile educts and products.
- forces the by-pass volume flow through the gutters and thus controls the droplet excess velocity for achieving a narrow residence time distribution.
- generates the overall pressure drop that effects the even dispersion of droplets in chains.
- feedbacks sensitively on the droplet shedding frequency and thus on the available exchange interface area.

The shape and the flow field of Taylor droplets are interdependent. They are connected via the Laplace pressure distribution on the interface. Both shape and flow are optically accessible with direct digital imaging. In case of a mismatched index of refraction between the phases, the droplet shape can be assessed [40]. The flow field may be investigated by means of microscopic particle image velocimetry (μPIV) [57], when the refractive indices are matched [39] and tracer particles are added.

In this thesis, a carefully conducted 3D2C μPIV measurement is the basis to accurately reconstruct the third velocity component of a Taylor flow. Based on the complete 3D3C velocity field the Navier-Stokes equation permits to derive the underlying 3D pressure field of a mean Taylor droplet. Additionally, a 3D model for the dynamically deformed Taylor droplet shape enables to access the flow and pressure conditions directly at the interface position and allows to calculate and verify local pressure gradients. A discussion of the governing forces and the fluid mechanics theory behind this investigation is

given in Chapter 2. The experimental methods and verification procedures applied in this thesis are explained in Chapter 3.

In Chapter 4, the three dimensional geometric model to approximate the interface shape of Taylor bubbles and droplets moving in rectangular microchannels is developed to describe and quantify the dynamic deformation of the Taylor droplet. The accuracy of the interface shape model is benchmarked with averaged μPIV raw-images of the statistical distribution of the particulate tracer. In the related experiments, the fluidic material system, the aspect ratio of the channel cross section, and the droplet length are varied. The model is found to predict the 3D interface position of Taylor droplets with less than 3% deviation if the viscous forces govern the surface tension forces.

Chapter 5 presents the results of the multiplane μPIV measurement of the 3D2C velocity distribution of Taylor droplets moving in a square horizontal microchannel. The third velocity component is reconstructed from the 2D measurement by means of intergrating the continuity equation [16, 17, 98] and an accuracy assessment of the reconstruction is presented based on a volume flow balance of the 3D3C velocity field. The velocity field allows a detailed investigation of the 3D flow features, such as stagnation regions and the shear rate distribution. The maximum shear rate is located at the entrances and exits of the wall films and at the corner flow (gutter) bypassing the Taylor droplet. The regions of high strain correspond to the cap positions of the Taylor droplets. This experimental data set allows the visualization of the streamlines of the velocity distribution on the interface of a Taylor droplet and to directly relate it to the main and secondary vortices of the droplet phase velocity field.

Based on the 3D velocity distribution, the 3D pressure field of a Taylor droplet is accessed in Chapter 6. The pressure field is divided in a wall-proximate part and a core-flow to describe the phenomenology. At the wall, the pressure decreases as expected in downstream direction. In contrast, a reversed pressure gradient is present in the core of the flow that drives the bypass flow of continuous phase through the corners (gutters) and causes the Taylor droplet's relative velocity between the faster droplet flow and the slower mean flow. Based on the pressure field the driving pressure gradient of the bypass flow is quantified, and a simple estimation method is verified: the

geometry of the gutter entrances and the interface tension deliver a Laplace pressure difference. As a direct measure for the viscous dissipation, the 3D distribution of work done on the flow elements is calculated, that is necessary to maintain the stationarity of the Taylor flow. The spatial integration of this distribution provides the overall dissipated energy and allows to identify and quantify different contributions from the individual fluid phases i.e. from the wall-proximate layer and from the flow redirection due to presence of the droplet interface. For the first time, deep insight is provided into the 3D pressure field and the distribution of the energy dissipation in the Taylor flow based on experimentally acquired 3D3C velocity data. The 3D pressure field and the 3D distribution of work is provided online as supplementary material to enable a benchmark for CFD and numerical simulations.

The accumulated results of this thesis - the velocity field, the pressure field and the interface approximation - allow a unique and dense visualization and investigation of the fluid dynamics of a viscous Taylor droplet. The interplay of the work done on the flow, the pressure, the flow and the interface shape displayed for this single reference case provides deep insight in the physic of this setting. The data-set is provided online to the fluid mechanics community as a benchmark case for parametric numeric studies.

2

Fluid mechanics of Taylor droplets

Once there was a particle
It felt no urge - no lousy prickle
it stopped and waited tearily
It had to move - in theory
I wish it'd helped to tickle

In the following chapter, a theoretical background to understand and describe the fluid mechanics of Taylor droplets is provided. At first a very brief supporting overview of the geometrical setting of a Taylor flow, it's properties, directions and orientation is given. Secondly, a discussion of the governing forces identifies the dominating forces of the addressed flow situation. Subsequently, a force balance at the interface relates the forces of the flow field to the interfacial tension forces of the dynamically deformed Taylor droplet. Finally, the derivation of the investigated quantities of higher order with respect to the velocity field is briefly explained.

2.1 Setting of the Taylor flow

A Taylor droplet with a length L_d moves along a microchannel of width W_ch and height H_ch (Fig. 2.1). The cross section area of the microchannel spans along the y- and z-axis and is given by $A_\mathrm{ch} = H_\mathrm{ch} \cdot W_\mathrm{ch}$. The droplet's absolute flow direction coincides with the positive x-axis and the droplet

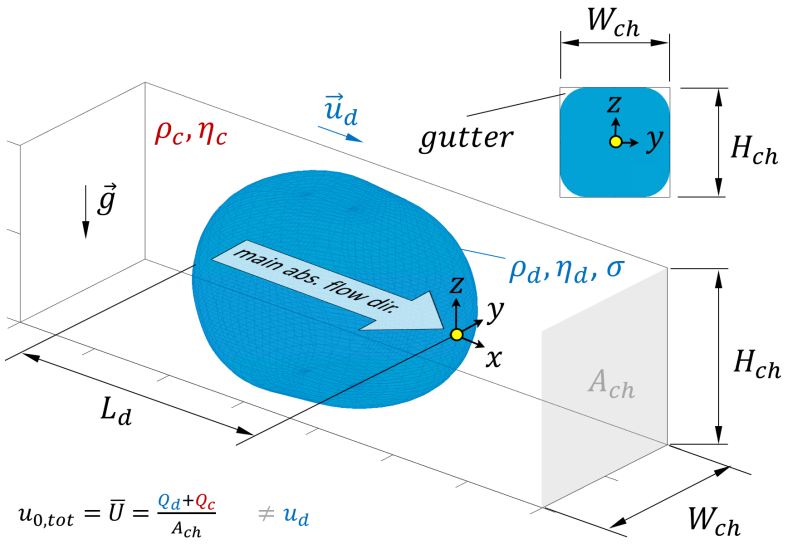

Fig. 2.1: Setting of the Taylor flow. Provides information on the geometrical dimension of the Taylor flow as well as on the denomination of the material properties, the coordinate system, the main absolute flow direction, the mean velocity of the entire flow and Taylor droplet velocity. Please note, that the droplet velocity u_d is commonly not equal to the mean velocity. The mechanism of this phenomenon is in part subject of this work.

translates through the microchannel with a droplet speed u_d. The mean velocity of the flow $\bar{U}$ is also denoted as the total superficial flow velocity $u_{0,\mathrm{tot}} = \bar{U} = \frac{Q_\mathrm{d}+Q_\mathrm{c}}{A_\mathrm{ch}}$ to distinguish it from the superficial velocities of the single phases feeding the Taylor droplet chain. Herein Q_d and Q_c denote the volume flow of the disperse and the continuous phase respectively. The gravitational acceleration points in negative z-direction. The material properties density ρ_i and dynamic viscosity η_i are indexed d and c assigning to the disperse and the continuous phase respectively. The interface tension between the immiscible phases is denoted with σ. Please note, that the droplet velocity u_d is commonly not equal to the mean velocity. The mechanism of this phenomenon is in part subject of this work.

2.2 Consideration of the governing forces

Bubbles or droplets in motion are subject to forces arising from gravity, interface tension, inertia and viscosity. For macroscopic freely moving two-

phase flows the Morton number Mo is a pure material parameter utilized to characterize the shape and the velocity of the dispersed phase.

$$\begin{aligned} Mo &= \frac{g\,\eta_{\mathrm{c}}^4\,\Delta\rho}{\rho_{\mathrm{c}}^2\,\sigma^3} \\ &= Bo\,Oh_{\mathrm{c}}^4 \end{aligned}$$

Herein, $\Delta\rho$ is the density difference between the interacting phases. The Morton-Number also applies to confined flows with Taylor droplets, since the same forces are relevant. A decomposition allows to distinguish between the weak influence of buoyancy forces on the droplet shape in case of the Bond-number Bo

$$Bo = \frac{g\,\Delta\rho\,H_{\mathrm{ch}}^2}{\sigma},$$

and the strong influence of the viscous and inertia forces on the droplet shape in case of the Ohnesorge-number Oh_{c}^4

$$\begin{aligned} Oh_{\mathrm{c}} &= \frac{\eta_{\mathrm{c}}}{\sqrt{H_{\mathrm{ch}}\,\rho_{\mathrm{c}}\,\sigma}} \\ &= \sqrt{\frac{Ca_{\mathrm{c}}}{Re_{\mathrm{c}}}}, \end{aligned}$$

A subdivision of the purely material related Ohnesorge-number into the capillary-number Ca_{c} and Reynolds-number Re_{c} shows the relation between the ratio of the viscous and interface forces, and the ratio of the inertia and viscous forces respectively. The Reynolds-number is defined as follows

$$Re_{\mathrm{c}} = \frac{\rho_{\mathrm{c}}\,u_{0,\mathrm{tot}}\,H_{\mathrm{ch}}}{\eta_{\mathrm{c}}}.$$

A Taylor droplet translates with a velocity u_{d} that is not necessarily equal to the total superficial velocity. Depending on the flow conditions (e.g. wetting/ no-wetting of the disperse phase), the droplet can be faster or slower than the

mean motion, because in a relative frame of reference the fluid is transported towards the droplet back or towards its front respectively. Three different concepts exist to quantify the relative movement of the disperse phase with respect to the mean motion of the entire flow.

i) Bretherton [15] introduced a "droplet mobility" m in his pioneering work on Taylor flow, which was later also used by Jakiela et al. [46].

$$m = \frac{u_{\mathrm{d}}}{u_{0,\mathrm{tot}}}$$

ii) The velocity difference between the droplet and the mean velocity is normalized with the droplet velocity. This approach is described in different terms by different authors: ("slipping velocity" [70], "relative droplet velocity" [8], "relative droplet velocity" [1], "dimensionless drift velocity" [43])

$$u_{\mathrm{slip}} = \frac{(u_{\mathrm{d}} - u_{0,\mathrm{tot}})}{u_{\mathrm{d}}}.$$

However, this description uses a flow dependent reference to describe the relative velocity difference between the droplet and the mean flow velocity. As the droplet velocity changes based on an outer independent parameter such as the total superficial velocity the denominator of the fraction changes as well. The result is a distorted relation.

iii) Helmers et al. [41] eliminate the issue by establishing a dimensionless "excess velocity".

$$u_{\mathrm{ex}} = \frac{(u_{\mathrm{d}} - u_{0,\mathrm{tot}})}{u_{0,\mathrm{tot}}}$$

The velocity difference between the droplet and the mean flow velocity is based on an independent variable and does not bias the description of the effect. In the presented work the term *excess velocity* will be used throughout to describe the velocity difference between the disperse phase and the mean flow.

The Capillary-number Ca_c determines the flow regime of the microscopic two-phase flow. For Taylor flows, the Capillary number relates to the changes of the droplet shape [40, 109].

$$Ca_c = \frac{\eta_c \, u_{0,\mathrm{tot}}}{\sigma}$$

The experimental parameters concerning this thesis (see Chapter 3 in Tab. 3.2) result the following range of dimensionless numbers:

$$\begin{aligned} Ca_c &= 0.004 - 0.005 \\ Re_c &= 0.014 - 0.055 \\ Bo &= 0.003 - 0.004 \end{aligned} \tag{2.1}$$

The above consideration allows to arrange the occurring forces in descending order of their importance to the phenomenology of the Taylor flow:

$$\text{surface tension forces} \gg \text{viscous forces} \gg \text{inertia forces} \gg \text{buoyancy forces}$$

2.3 Force balance at the interface

The interface shape of a Taylor droplet changes from static conditions (without flow) to dynamic conditions [40, 82]. At steady state, a clean droplet interface dA between two immiscible phases is subject to the following balance of normal forces (Fig. 2.2).

$$-F^j_{\mathrm{LP,c}} + F^j_{\mathrm{p,c}} + F^j_{u,\mathrm{c}} + F^j_{\mathrm{LP,d}} - F^j_{\mathrm{p,d}} - F^j_{u,\mathrm{d}} = 0. \tag{2.2}$$

Herein, $F^j_{u,i}$ refers to the normal forces induced by the adjoining flow conditions, $F^j_{p,i}$ indicates the normal forces exerted by the pressure and $F^j_{\mathrm{LP,i}}$

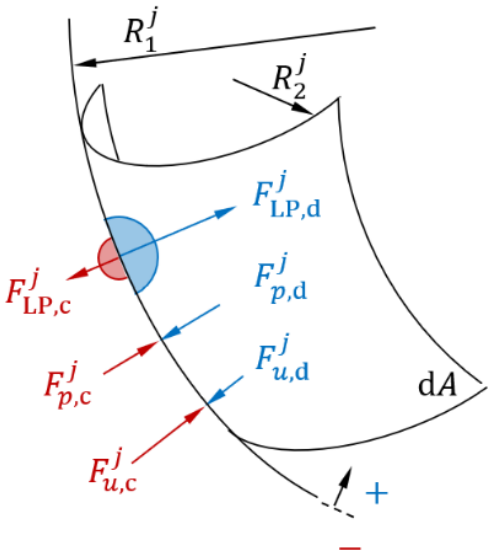

Fig. 2.2: Forces F_k^j at a curved interface $\mathrm{d}A$ between two immiscible phases (d - disperse phase, c - continuous phase) in combination with the principle radii $R_{1,2}^j$ to link the Laplace-pressure to the adjoining flow field. The superscript j refers to static (j = stat.) versus dynamic (j = dyn.) flow conditions. The positive reference direction points into the disperse phase

represents the normal forces that arise from the energetic molecular interaction inside the individual phases. The latter macroscopically results in the surface tension forces and is related to the Laplace-pressure. The index j refers to the flow conditions with $j = \mathrm{stat}$ denoting the static case (without flow) and $j = \mathrm{dyn}$ representing the influence of velocity field. The index i refers to either the disperse phase $i = \mathrm{d}$ or the continuous phase $i = \mathrm{c}$. Tangential forces immediately induce flow on ideal clean interfaces and do not contribute to this balance. The experimental results of Mießner et al. [83] (Chap. 5) clearly show interface mobility and support the assumption of a minor interface contamination and an ideal interface behavior.

Eq. 2.2 allows to compare the force balance at static conditions (j = stat) with the force balance at dynamic conditions (j = dyn). A consideration of the individual terms simplifies the equation. The forces exerted by the pressure on the respective sides of the interface cancel out ($F_{p,\mathrm{d}}^j = F_{p,\mathrm{c}}^j$). Without flow, the velocity forces of the static conditions vanish ($F_{u,i}^{\mathrm{stat}} = 0$). the forces across the interface are combined to a resulting force that can be calculated from the Laplace-pressure $\Delta F_{\mathrm{LP}}^j = +F_{\mathrm{LP,d}}^j - F_{\mathrm{LP,c}}^j$. A separation

between the flow-induced forces and the interface tension forces links the shape deformation directly to the adjoining flow field:

$$\Delta F_{\mathrm{LP}}^{\mathrm{stat}} - \Delta F_{\mathrm{LP}}^{\mathrm{dyn}} = +F_{u,\mathrm{c}}^{\mathrm{dyn}} - F_{u,\mathrm{d}}^{\mathrm{dyn}} \tag{2.3}$$

A division of the forces by the interface area $\mathrm{d}A$ results in a relation between the flow-induced pressure field and the Laplace-pressure difference between the static and the dynamic interface shape:

$$\begin{aligned} (\Delta p_{\mathrm{LP}}^{\mathrm{stat}} - \Delta p_{\mathrm{LP}}^{\mathrm{dyn}}) &= +p_{u,\mathrm{c}}^{\mathrm{dyn}} - p_{u,\mathrm{d}}^{\mathrm{dyn}} \\ \Delta p_{\mathrm{LP}}^{(\mathrm{stat}\mapsto\mathrm{dyn})} &= +p_{u,\mathrm{c}}^{\mathrm{dyn}} - p_{u,\mathrm{d}}^{\mathrm{dyn}} \end{aligned} \tag{2.4}$$

In disregard of the involved material parameters of the Taylor flow ($\sigma, \rho_{\mathrm{d}}, \rho_{\mathrm{c}}, \eta_{\mathrm{d}}, \eta_{\mathrm{c}}$) the left hand side of Eq. 2.4 consists of geometry information, while the right hand side is based on the flow field. This allows a direct quantitative comparison between the curvature-dependent Laplace-pressure of the interface geometry and the velocity field dependent pressure difference at the interface.

2.4 Derived Quantities

The derivation of the investigated quantities of higher order with respect to the velocity field is briefly explained. Herein, the relative coordinate system is defined (Fig. 2.3). Its origin is set to the downstream tip of Taylor droplet's frontal cap. The x-axis points downstream into the direction of motion. The y-axis is the perpendicular direction of imaged measurement plane, while the z-axis represents the out-of-plane transverse direction.

At first the momentum thickness is calculated, the shear rate distribution in the flow is quantified and the λ_2-criterion is introduced to visualize the main and secondary vortices. Next the pressure field is quantified based on an integration of the Navier-Stokes equation and the pressure distribution on the interface is calculated from the pressure field. Finally, the derivation of

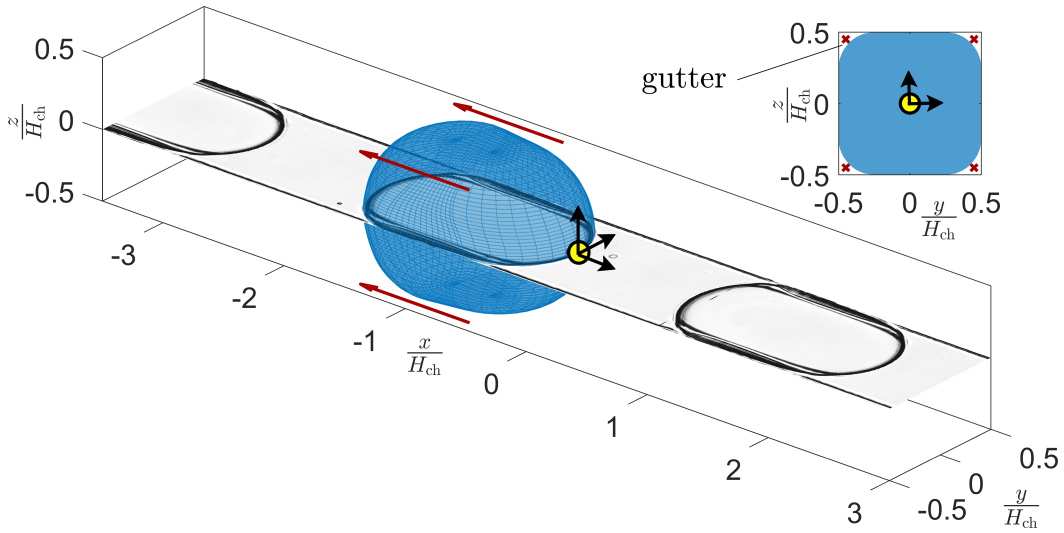

Fig. 2.3: Sketch of the a coordinate system for the Taylor flow investigation: The downstream motion of the Taylor flow is oriented along the x-axis. The origin of the coordinate System is set to the tip of the Taylor droplet's frontal cap (yellow dot). The y-axis is the perpendicular direction of the imaged measurement plane ($x-y$ plane through the origin). The z-axis represents the out-of-plane transverse direction along which the focal plane can be moved. The red arrows visualize the relative volume flow through the gutters

the distribution work done on the flow is derived and methods to estimate the overall energy loss of the investigated flow are presented.

2.4.1 Momentum thickness

The pressure field is divided in a wall-proximate part and a core-flow to support the description of the Taylor flow phenomenology. The simple flow field of a laminar single-phase flow through a straight pipe solely evolves due to the wall contact of the fluid. In contrast, the flow in and around a Taylor droplet is more complex due to the additional presence of the droplet interfaces.

Thus, the momentum thickness δ_2 of a reference Poiseuille flow in a circular microchannel (Fig. 2.4) is calculated to geometrically discriminate between an immediate wall influenced region and the remaining core of the flow. Details on the momentum thickness are provided by Schlichting and Gersten [102].

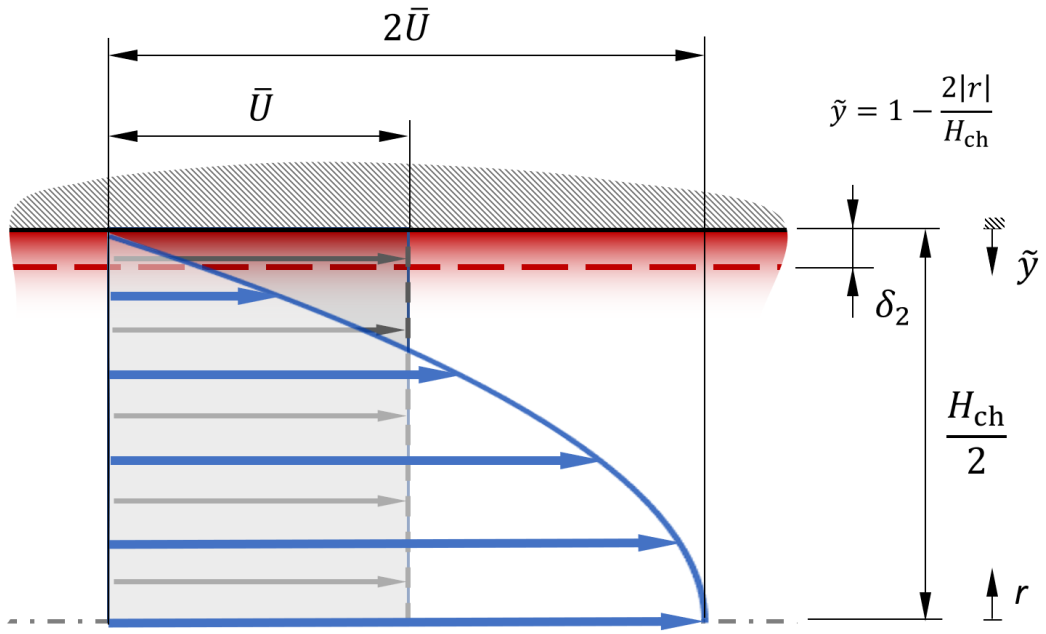

Fig. 2.4: Sketch of laminar flow conditions in circular pipe flows. Here r denotes the radial coordinate of the pipe and $\tilde{y}$ is the dimensionless wall distance. The momentum thickness δ_2 quantifies a distance in which the flow is dominated by the presence of the wall. The thickness enables to geometrically discriminate between wall-influenced flow regions and the core of the flow. The layer thickness amounts to $\delta_2 = \frac{1}{15} H_{\mathrm{ch}}$

The calculation of momentum thickness δ_2 returns a defined length scale at a fixed geometric fraction of the channel height

$$\delta_2 = \frac{1}{15} H_{\mathrm{ch}}. \tag{2.5}$$

Three cases set the momentum thickness δ_2 into perspective to qualitativly show the validity of the approach: The normalized analytical 2D velocity profile of the single-phase Poiseuille flow through the cross-section of a circular microchannel (Fig. 2.5a), through a square mircochannel (Fig. 2.5b) and a measured stream-wise velocity profile at the central cross-section of a Taylor droplet's main vortex (Fig. 2.5c). For the latter case, half of the microchannel is depicted, since the measurement data covers only half of the flow volume. The selected cases verify the use of the momentum thickness as reference to distinguish between wall-proximity and the core of the flow.

For better comparability, the 2D shear distributions are normalized with wall shear stress of a laminar flow in a circular microchannel $\tau_{\mathrm{ref}} = \frac{8\bar{U}}{H_{ch}}$. Values close to one show regions where the shear profile of the respective case equals the reference value (Fig. 2.5d-e).

A dashed line represents the border of the wall-influenced flow layer. As expected, the reference shear and the wall-shear agree at the wall in the circular channel (Fig. 2.5d, dotted line). The normalized shear distribution in the laminar single-phase flow of a square channel shows increased shear at the center of the side walls compared to the circular channel (Fig. 2.5e, dotted line). The equality of the shear profile to the reference-shear moves inwards to the position of the momentum thickness δ_2. The same observation holds true for the measured case of the Taylor droplet (Fig. 2.5f). The solid black line indicates the interface position. In the gutter, additional shear is present outside the droplet due to the by-pass flow and the high ratio λ between droplet viscosity η_{d} and bulk viscosity η_{c} ($\lambda = \frac{\eta_{\mathrm{d}}}{\eta_{\mathrm{c}}} = 2.625$). The magnitude of the shear distribution is not ideally symmetric in the y-direction at the top wall, because the reconstruction of the velocity z-component is subject to integration error and integration of noise error. A comparison of the well-resolved measurement in the y-direction with the reconstructed results in the z-direction shows a similar trend of an increased shear in proximity of the momentum thickness. Therefore, the layer thickness δ_2 is a

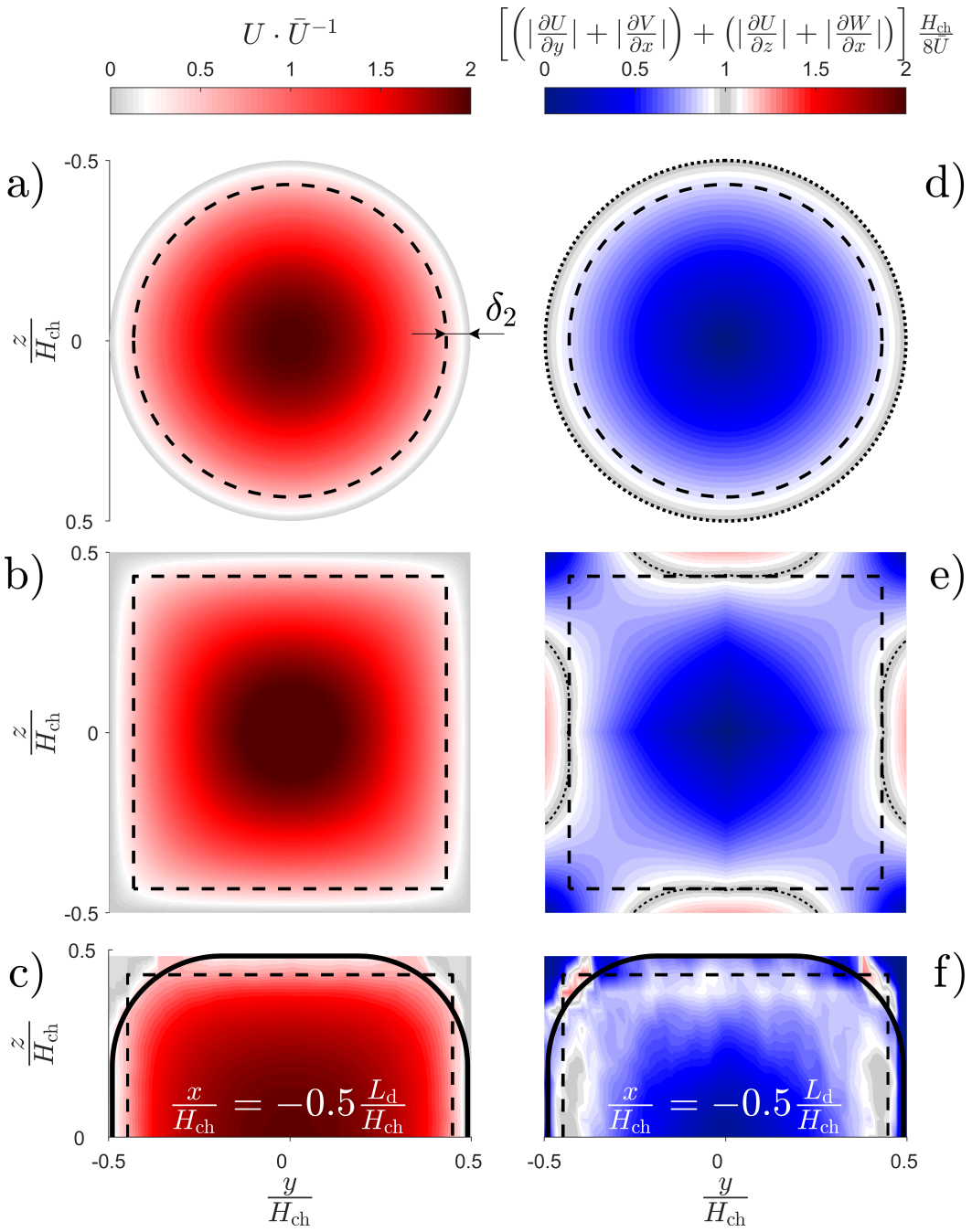

Fig. 2.5: Cross-sectional comparison between the analytical solutions of laminar single-phase flows in circular (a,d) and square channels (b,e) with measurements of a Taylor flow in a square channel in one half of the symmetric channel (c,f). The cross-section of the droplet flow is placed at the center of the main vortex in the droplet, where the velocities are mainly directed in flow direction (see streamlines Fig. 6.4a). The interface is marked with a solid black line. The velocity distribution is shown on the left (a-c) and the shear rate distribution is given on the right (d-f). The dashed black line indicates the momentum thickness δ_2. The shear rates in the square channel for single-phase flows (e) and for the two-phase flow (f) equal the wall-shear rate of the pipe flow at a distance of $\approx \delta_2$ on the y- and z-axis

valid measure to discriminate between wall-dominated regions and the core of a Taylor flow.

2.4.2 Shear rate distribution

Based on the reconstructed 3D flow field of the Taylor droplet, the shear rates of the flow are used to visualize the location of high strain of the investigated Taylor droplets.

$$\dot{\gamma}^* = \frac{H_{\mathrm{ch}}}{8u_{\mathrm{d}}} \left(\left(\left| \frac{\partial u}{\partial y} \right| + \left| \frac{\partial u}{\partial z} \right| \right) + \left(\left| \frac{\partial v}{\partial x} \right| + \left| \frac{\partial v}{\partial z} \right| \right) + \left(\left| \frac{\partial w}{\partial x} \right| + \left| \frac{\partial w}{\partial y} \right| \right) \right)$$

As reference shear rate $\dot{\gamma}_{\mathrm{ref}}$ the wall shear rate of laminar flow in a circular channel with a diameter of H_{ch} is applied: $\dot{\gamma}_{\mathrm{ref}} = \frac{8u_{0,\mathrm{tot}}}{H_{\mathrm{ch}}} \approx \frac{8u_{\mathrm{d}}}{H_{\mathrm{ch}}}$. To locate the strain maximum, the directional influence of the derivatives is omitted and only absolute values are used.

2.4.3 Vortex visualization applying the λ_2-criterion

The λ_2-criterion [48] visualizes the vortical structures in and around the Taylor droplet. In their concept, a vortex is defined as a connected region with two negative eigenvalues i.e. the second eigenvalue $\lambda_2 < 0$, which corresponds to a vortex pressure minimum. This specific vortex visualization is applied to the experimental results, since the method omits the effects from unsteady straining and viscosity.

2.4.4 3D pressure distribution

Two approaches are available to compute the pressure distribution from the μPIV measurements. One is based on the solution of the Poisson equation and requires a set of (Neumann/ Dirichlet) boundary conditions to derive the pressure field [36, 54, 59]. The second approach involves the direct integration of the momentum equation by means of finite differences. The main

problem with the latter method is related to the accumulation of noise and integration error, which is successively incorporated into the derived pressure field [13, 47, 71, 112]. Recently, Cai et al. [20] proposed a variational formulation for the pressure-from-velocity problem in two dimensions.

Charonko et al. [21] reported that line integral methods perform better for the internal flow, while the pressure Poisson equation is superior for the external flow. Kat and Oudheusden [54] proposed guidelines for the temporal and spatial resolution of the PIV-data. While the acquisition frequency has no relevance in the investigated quasi-stationary Taylor flow, the interrogation window size is supposed to be 5 times smaller than the flow structures to properly resolve the pressure features. In the presented case the interrogation window size is about 14 times smaller than the vortex features.

In contrast to the applications of the above stated papers, the μPIV-study incorporated into this work deals with Taylor droplets at low Ca_{c} and Re_{c}, i.e. the surface tension forces dominate the viscous forces and inertia plays a subordinate role. Thus, a direct integration scheme is applied to obtain the pressure, since an internal flow is addressed and the second velocity derivatives of the viscous dissipation need to be considered.

The Navier-Stokes equation for stationary incompressible viscous flows with negligible influence of body forces reads as follows:

$$\rho\left(\vec{u}\cdot\nabla\right)\vec{u} = -\nabla p + \eta\nabla^2\vec{u} \tag{2.6}$$

Based on the measured velocity field, the velocity gradient tensor is calculated together with the second derivatives. For the estimate of the pressure from the flow field, the Navier-Stokes equation is directly integrated. Since a reference pressure for the flow field is not available, the integration constant ($c = 0$) is omitted.

$$\begin{aligned} p_{u,i}^{\mathrm{dyn}} = \quad & -\rho_i \int_V \left(\vec{u}\cdot\nabla\right)\vec{u}\,\mathrm{d}\vec{x} \\ & +\eta_i \int_V \left(\nabla^2\vec{u}\right) \quad \mathrm{d}\vec{x} \end{aligned} \tag{2.7}$$

The direct integration procedure is done separately for the convective and the dissipative velocity contributions. Each integration step with respect to a coordinate axis is performed twice: Along and against the axis-direction. The two respective results are averaged to reduce the influence of error accumulation [21]. The consideration of 3D3C-velocity field of a two-phase flow requires to discriminate between the material properties of the individual phases. The interface approximation of Mießner et al. [82] (Chap. 4) serves as a logical discriminator to attribute the material properties to the according phases. The convective contributions are added to the viscous terms to receive the entire 3D pressure field.

2.4.5 Pressure distribution on the droplet interface

In this section, two ways are described to retrieve information on the pressure on the surface of a moving Taylor droplet. A geometric consideration that is based on the geometric curvature information of the interface approximation and the flow based pressure information across the interface. The geometry-based quantity is later (Fig. 6.2a) compared to the pressure difference across the interface that is reconstructed from the 3D velocity information (Fig. 6.2b).

The energetic minimization of the adhesion and cohesion forces between the molecules along and across the clean interface $\mathrm{d}A$ of the contacted phases (Fig. 2.2) determine its curvature at static flow conditions. The Laplace-pressure describes the macroscopic effect that relates the interface tension with the curvature of $\mathrm{d}A$ to the pressure in the disperse phase.

$$\Delta p_{\mathrm{LP}}^{j} = \sigma \left(\frac{1}{R_1^j} + \frac{1}{R_2^j} \right) \tag{2.8}$$

When the flow field close to the interface exerts normal forces onto the interface $\mathrm{d}A$, the curvature is deformed from the static shape ($j = \mathrm{stat}$) and the Laplace-pressure is altered ($j = \mathrm{dyn}$).

The pressure difference between both geometric states equals the pressure contribution exerted by the flow (Eq. 2.4). Thus, there are two methods

to derive the pressure distribution on a moving Taylor droplet: i) With knowledge of the geometry of the interface shape, the curvature distribution is calculated and the Laplace-pressure distribution is determined. ii) The evaluation of the 3D velocity field of a moving Taylor droplet delivers the pressure difference across the interface at the location of the interface.

i) The approximation of the Taylor droplet interface [82] (Chap. 4) provides the necessary primary and secondary geometry information. Primary information means e.g. location, volume, interface area, while secondary information refers to e.g. the curvature distribution. The static and the dynamic shape of the droplet deliver the respective curvature distributions to calculate the curvature difference distribution $\Delta\kappa$. For the latter step, the Matlab script "Surfature" [@23] is applied:

$$\begin{aligned}
\Delta p_{\mathrm{LP}}^{(\mathrm{stat}\mapsto\mathrm{dyn})} &= \sigma\left(\frac{1}{R_1^{\mathrm{stat}}}+\frac{1}{R_2^{\mathrm{stat}}}\right)-\sigma\left(\frac{1}{R_1^{\mathrm{dyn}}}+\frac{1}{R_2^{\mathrm{dyn}}}\right)\\
&= \sigma\left(\frac{R_1^{\mathrm{dyn}}-R_1^{\mathrm{stat}}}{R_1^{\mathrm{stat}}R_1^{\mathrm{dyn}}}+\frac{R_2^{\mathrm{dyn}}-R_2^{\mathrm{stat}}}{R_2^{\mathrm{stat}}R_2^{\mathrm{dyn}}}\right)\\
&= \sigma\left(\Delta\kappa_1^{(\mathrm{stat}\mapsto\mathrm{dyn})}+\Delta\kappa_2^{(\mathrm{stat}\mapsto\mathrm{dyn})}\right) \qquad (2.9)
\end{aligned}$$

The expression in Eq. 2.9 is a direct geometric measure for the pressure exerted onto the interface. This scalar quantity is projected onto the interface and easily compared to the pressure derived from the velocity field.

ii) To receive the flow-related pressure on the moving Taylor droplet interface, the pressure of the disperse phase $p_{u,\mathrm{d}}^{\mathrm{dyn}}$ is subtracted from pressure of the continuous phase $p_{u,\mathrm{c}}^{\mathrm{dyn}}$ (Eq. 2.4). The equation is valid only at the position of the interface, because here the Laplace-pressure emerges from the material property changes. The interface approximation [82] (Chap. 4) is used to determine the interface location of the moving droplet. The resulting pressure difference is a scalar quantity that is also projected onto the interface and compared to the curvature-based Laplace-pressure distribution.

2.4.6 3D field of the work done on the flow

Macroscopically, work is added to the flow by a syringe pump that builds up a pressure gradient to establish the flow (kinetic energy) in the microchannel. To maintain this flow stationary, the overall work added to the flow system needs to compensate for directional changes, potential energy changes and frictional losses. In the considered case, the system is quasi-stationary, isothermal and incompressible, volume forces have no effect and Stokes-flow conditions apply for a Newtonian fluid ($Re_c = 0.52$). Thus, the work added by the pump to the stationary flow solely compensates for the total friction losses in the system.

The work to drive a single average quasi-stationary Taylor droplet through a microchannel is calculated by volume integration of the work done on individual fluid elements $\mathcal{W}$. The work done on the fluid elements composes a scalar field. For an individual element, the work is calculated from the forces $\vec{F}$ acting along its path $\vec{s}$.

$$\mathcal{W} = \vec{F} \cdot \vec{s} \tag{2.10}$$

The forces are derived from the total change of momentum $\vec{I}$ over time, with m, ρ and V being the mass, density and volume of the fluid element, respectively.

$$\vec{F} = \frac{\mathrm{D}\vec{I}}{\mathrm{D}t} = \frac{\mathrm{D}m\vec{u}}{\mathrm{D}t} = V\rho\frac{\mathrm{D}\vec{u}}{\mathrm{D}t} \tag{2.11}$$

The above stated flow conditions (stationary Stokes-flow, etc.) simplify the Navier-Stokes equation in (2.6) to

$$\vec{\nabla}p = \eta\vec{\nabla}^2\vec{u}. \tag{2.12}$$

Thus, the only forces that cause a pressure change in the considered Taylor flow are the friction forces. The work done on a fluid element to compensate the friction forces is expressed as

$$\mathcal{W} \quad = \quad \vec{F} \cdot \vec{s} = \left(V \eta \vec{\nabla}^2 \vec{u} \right) \cdot (\vec{u} t) \, . \tag{2.13}$$

Herein, the vector of the element's path $\vec{s}$ is estimated with its velocity and a short period of reference time $\vec{s} = \vec{u}t$. A non-dimensional representation of the work done per fluid element emerges after division by a reference work. As reference serves the work done on a laminar pressure-driven ($\Delta p_{\mathrm{HP,c}}$) single-phase flow (Hagen-Poiseuille flow - HP) of continuous phase ($Q = Q_{\mathrm{tot}}$) through the same square cross section A_{ch}.

$$\mathcal{W}_{\mathrm{ref}} = \vec{F} \cdot \vec{s} = \left(\Delta p_{\mathrm{HP,c}} \cdot A_{\mathrm{ch}} \right) \left(\frac{Q_{\mathrm{tot}}}{A_{\mathrm{ch}}} t \right) \tag{2.14}$$

The scalar 3D field of dimensionless work $\mathcal{W}^*$ reads as follows:

$$\mathcal{W}^* \quad = \quad \frac{\mathcal{W}}{\mathcal{W}_{\mathrm{ref}}} = \frac{\left(V \cdot \eta \vec{\nabla}^2 \vec{u} \right) \cdot (\vec{u} t)}{\left(\Delta p_{\mathrm{HP,c}} \, Q_{\mathrm{tot}} \right) t} \tag{2.15}$$

Negative values of the work indicate deceleration of the flow, while positive values represent acceleration of fluid elements.

The duration of the reference time can be chosen arbitrarily, since the considered Taylor flow is quasi-stationary in the relative frame of reference. This leads to the conclusion, that the dimensionless work $\mathcal{W}^*$ calculated above is equal to the dimensionless power loss P^* and the dimensionless pressure drop Δp^*.

$$
\begin{aligned}
P^* &= \frac{P}{P_{\mathrm{ref}}} &&= \frac{\left(V \cdot \eta \vec{\nabla}^2 \vec{u}\right) \cdot (\vec{u})}{\left(\Delta p_{\mathrm{HP,c}}\, Q_{\mathrm{tot}}\right)} \\
\Delta p^* &= \frac{\Delta p}{\Delta p_{\mathrm{ref}}} &&= \frac{Q_{\mathrm{tot}}^{-1} \left(V \cdot \eta \vec{\nabla}^2 \vec{u}\right) \cdot (\vec{u})}{\Delta p_{\mathrm{HP,c}}} \\
\mathcal{W}^* &\cong P^* &&\cong \Delta p^*
\end{aligned}
\tag{2.16}
$$

Despite the equivalence of the dimensionless quantities, the presentation of this work is based on the above introduced concept of work that needs to be done on the flow to overcome the viscous losses in order to maintain the flow stationary.

2.4.7 Quantification of the overall energy dissipation

The overall energy loss of the Taylor flow is quantified by determination of the work $\mathcal{W}_i^*$ that is necessary to keep the observed flow section stationary (Sec. 2.4.6). To obtain a dimensionless quantity, the work done to keep up the Taylor flow is divided by the work that is necessary to maintain a Hagen-Poiseuille flow of continuous phase with the same total volume flow through the same cross section. The experimental data set offers three different derivation possibilities for the overall energy loss of a moving Taylor droplet:

i) The shear forces $F_{\tau,x}$ at the wall and the drag forces $F_{\Gamma,x}$ at the droplet interface along the droplet deliver the total resisting force. The 2D distribution of the pressure on the surface of a moving Taylor droplet is used to estimate the drag forces of the droplet interface. The interface-grid is re-sampled into cylindrical coordinates (Fig. 2.6a) in order to correspond to the x-axis grid of the velocity data. The x-axis points in downstream direction. The cumulated resistance forces in the flow direction are calculated for the gutter region and the film region separately. The pressure Δp_Γ on a surface area element $\mathrm{d}A$ (Fig. 2.6b) results in a force normal $\vec{n}_0$ to the area element. Its projection in flow direction $\vec{e}_{x,0}$ contributes to the drag of the droplet (Fig. 2.6c). A

summation of all resistance forces $F_{i,x}$ along the ϕ-direction of the flow delivers the drag force distribution at the droplet interface $F_{x,\mathrm{res}}$. A cumulative sum of the latter provides the drag force evolution along the Taylor droplet $\sum_V F_{\Gamma,x}$ (Fig. 2.6d).

$$\mathcal{W}_F^* = \frac{\left(\sum_V F_{\tau,x} + \sum_V F_{\Gamma,x}\right) L_\mathrm{d}}{\left(\Delta p_{\mathrm{HP,c}} A_\mathrm{ch}\right) L_\mathrm{d}} \tag{2.17}$$

ii) The pressure profile at the wall of the channel is an indicator for the pressure loss of the flow. The flow loses energy in the same rate as the profile changes. Thus, a linear fit of the inverted mean pressure profile at the wall serves as reference for the evolution of the pressure loss $\Delta\bar{p}_\mathrm{wall}(x)$ along the droplet in flow direction. A measure for the drag forces is established after multiplication with the area of the channel cross section. The work done on the flow is received from the forces acting along the droplet path of length L_d.

$$\mathcal{W}_{\Delta p,\mathrm{wall}}^* = \frac{\left(\Delta\bar{p}_\mathrm{wall}(x) A_\mathrm{ch}\right) L_\mathrm{d}}{\left(\Delta p_{\mathrm{HP,c}} A_\mathrm{ch}\right) L_\mathrm{d}} \tag{2.18}$$

iii) The work distribution in the viscous flow field inside and outside the droplet is derived in Sec. 2.4.6. A summation of the work in transverse direction and a calculation the cumulative sum in flow direction delivers the evolution of the flow field-related work done along the droplet.

$$\mathcal{W}_u^* = \sum_V \frac{\left(V \cdot \eta \vec{\nabla}^2 \vec{u}\right) \cdot \vec{u}\, \Delta t}{\left(\Delta p_{\mathrm{HP,c}}\, Q_\mathrm{tot}\right)\, \Delta t} \tag{2.19}$$

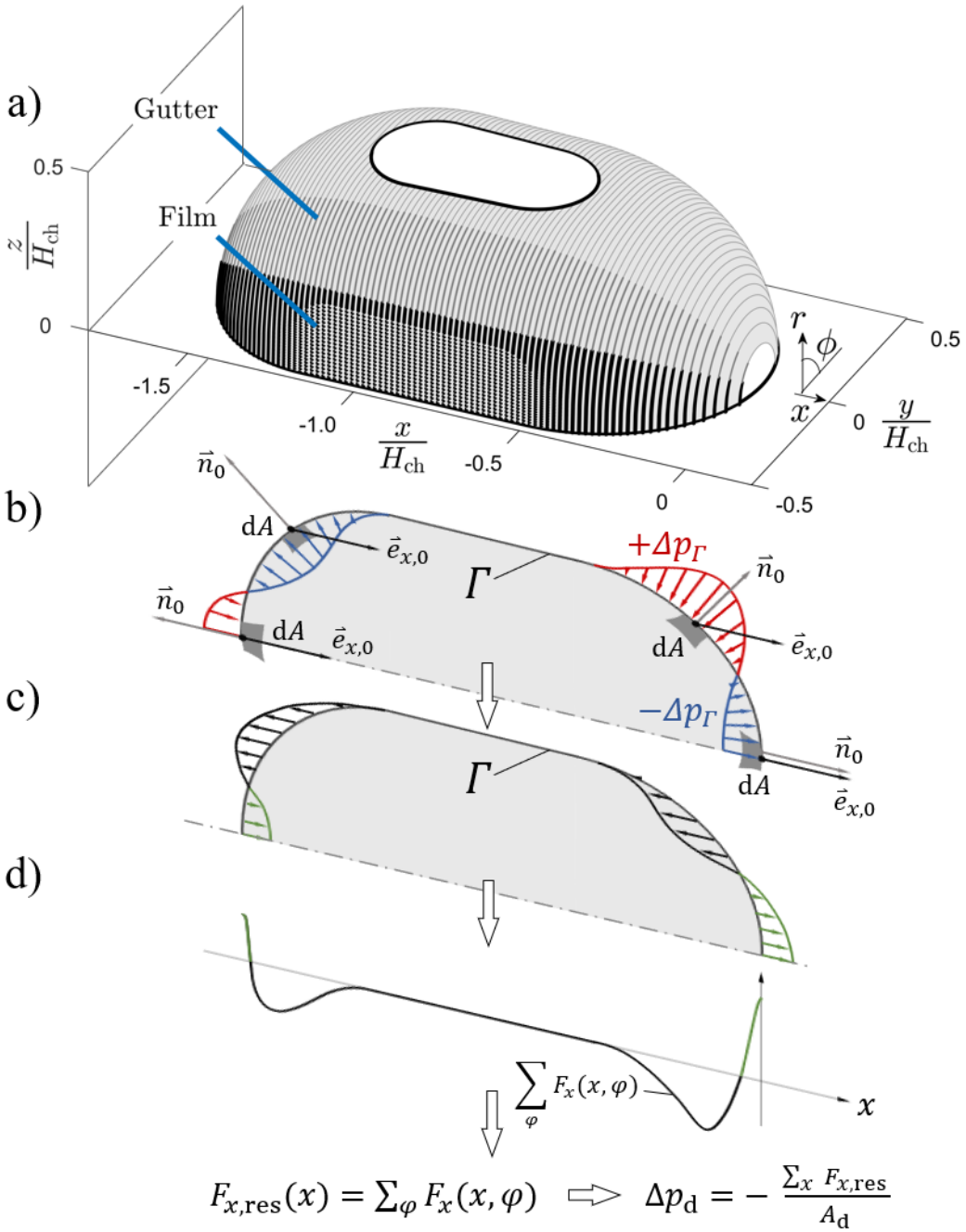

Fig. 2.6: Evaluation scheme of forces acting on the Taylor droplet interface. a) Redefinition of the droplet interface grid into cylindrical coordinates to enable a calculation of the drag force, since the velocity data grid and the nodes of the interface do not coincide. The common x-axis allows to compare the obtained profiles. The interface forces are evaluated in a gutter region and in a film region. The symmetry of the measurement domain is used to calculate the total drag force. b)-c) show the conversion scheme of the pressure at the interface Γ of a moving Taylor droplet b) into a drag force distribution in flow direction c) to calculate the total drag force along the Taylor droplet length L_d d).

3

Materials and Methods

Once there were some particles
No lonely one - comfortable
Their number grew proportional
In bulk they were transportable
This method seemed reportable

In order to investigate the flow in and around Taylor droplets at low capillary-numbers, two sets of experiments were conducted: The first set involves a parameter variation for the validation of the interface approximation [82] (Chap. 4), while the second set investigates the flow at a fixed parameter vector to perform an in-depth μPIV case study. The general experimental setup and the raw-image pre-processing is identical for both parts of the investigation. However, the microchannel geometry, the fluidic parameters and material properties are detailed separately.

The experimental materials and methods are presented in this chapter. At first, the micro fluidic and optical part of the set-up in which the experiments are performed is described. Secondly, the two-phase material system is detailed and subsequently the applied refractive index matching method is provided. Next, the image processing methods for the particle image based interface position measurement are explained with respect to the in-plane droplet recognition as well as the out-of-plane alignment in z-direction. Succeedingly, the ensemble correlation technique of the μPIV measurement approach is described. Finally, the reconstruction of the third velocity component is given with a validation of the result.

3.1 Experimental set-up

The continuous Taylor flow is established in micro fluidic polydimethylsiloxane (PDMS) devices featuring a flow-focusing channel layout with a pinhole at the junction to form the droplets (Fig. 3.1a). A glass wafer of $200\,\mu\mathrm{m}$ thickness is spin-coated with a 50μm layer of PDMS to create micro channels with PDMS on all inner surfaces. Therefore, equal wetting conditions are established on the lid and the channel walls. SEM-imaging and visual inspection suggest that the surface roughness ($\mathrm{R_A} \lessapprox 0.2\,\mu\mathrm{m}$) is small in relation to the channel hight. The ductility of the PDMS material causes the channel to slightly dilate upon the onset of the Taylor flow.

The cross section of the microchannel has a slight trapezoidal deviation from the rectangular shape (e.g. $W_{\mathrm{ch},1} = 104\,\mu\mathrm{m}$, $W_{\mathrm{ch},2} = 96\,\mu\mathrm{m}$, $H_{\mathrm{ch}} = 96\,\mu\mathrm{m}$). The cross section forms a convex isosceles trapezoid with the channel side walls enclosing an angle of $4.7°$ in comparison to an angle of $0°$ between the parallel side walls of a rectangular microchannel. The trapezoidal deviation from an ideal rectangle is a result of the fabrication process. This shape deviation is considered to be small and the cross section is treated as being rectangular.

The pinhole section is the narrowest part of the FF-junction and has a width of $W_{\mathrm{pin}} = 50\,\mu\mathrm{m}$. The channel layouts offer aspect ratios $A_{\mathrm{r}} = 1$ and 2 and the dimensionless channel length $\frac{L_{\mathrm{ch}}}{H_{\mathrm{ch}}}$ is about 500. An overview of the geometrical channel parameters is given in Tab. 3.1.

Tab. 3.1: Geometry parameters of the FF-channels used for all experiments

Geometry parameter		Unit
Channel width W_{ch}	0.104	mm
	0.208	mm
Channel height H_{ch}	0.096	mm
Channel length L_{ch}	50.000	mm
Pinhole width W_{pin}	0.050	mm
Channel length ratio $\frac{L_{\mathrm{ch}}}{W_{\mathrm{ch}}}$	500.000	-
Channel aspect ratio A_{r}	1.082	-
	2.167	-

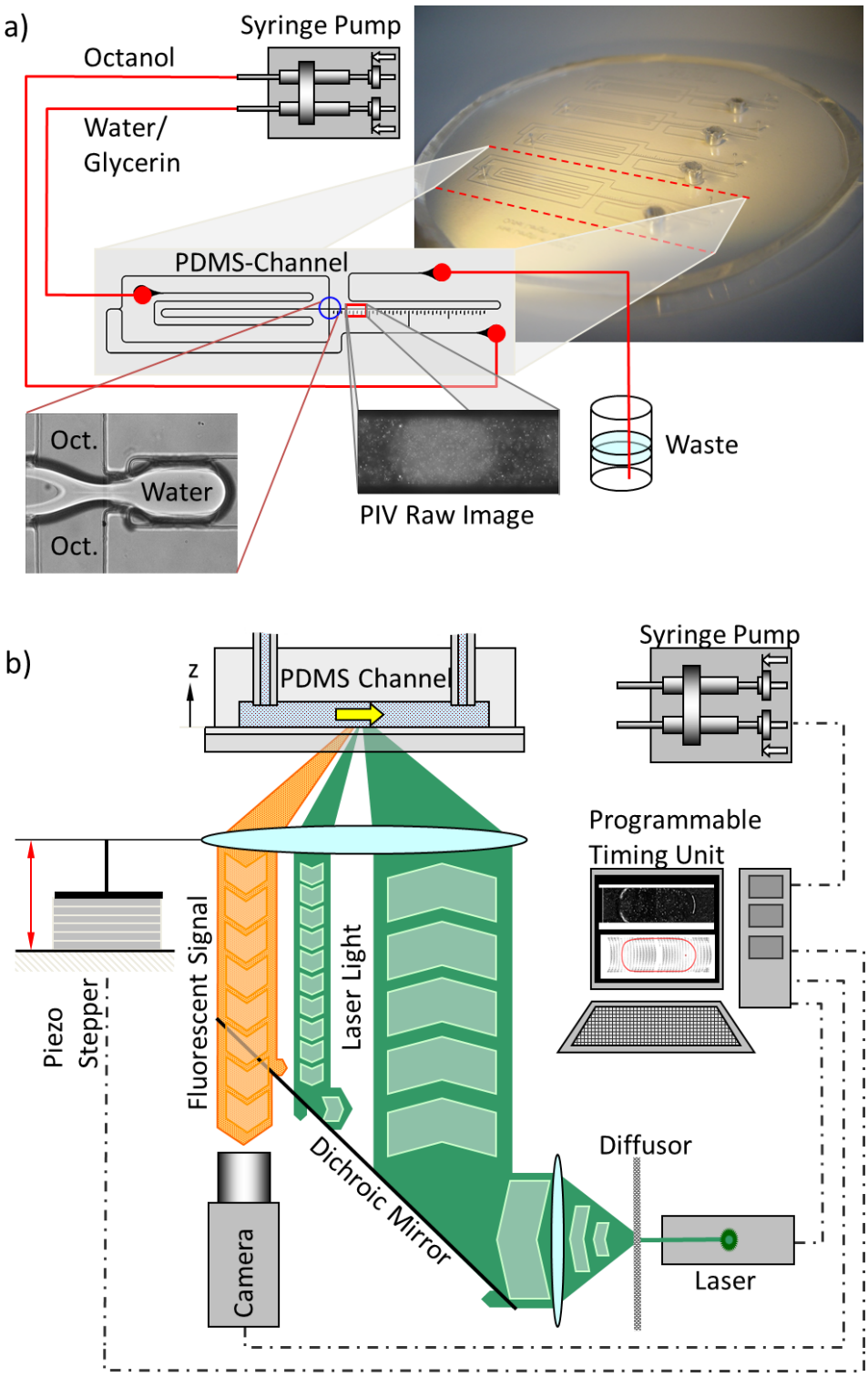

Fig. 3.1: a) A programmable timing unit coordinates the measurement set-up. A syringe pump establishes the flow, while a piezo stepper addresses the measurement plane. Laser light excites the fluorescent tracer particles. The fluorescent signal results in a particle image. b) The syringe pump establishes a continuous steady flow rate. On the fluidic PDMS-chip the octanol continuum and an immiscible aqueous droplet are contacted in a flow-focussing junction to form a Taylor flow. The particle images are recorded at about a 1/100 $\times L_{\mathrm{ch}}/W_{\mathrm{ch}}$ downstream of the junction.

Tab. 3.2: Fluidic parameter variation of the experiments to asses the accuracy of the interface approximation [82] (Chap. 4)

	H_2O/ DMSO	H_2O/ DMSO	H_2O/ Gly.	H_2O/ Gly.	H_2O/ Gly.	
A_r	1	1	1	1	2	-
$\frac{L_d}{W_{ch}}$	1.66	1.04	1.44	1.04	1.31	-
Q_d	0.41	0.22	1.24	0.67	2.25	$\mu L\,min^{-1}$
Q_c	0.34	0.52	1.01	1.57	2.25	$\mu L\,min^{-1}$
$u_{0,tot}$	1.25	1.25	3.76	3.76	3.76	$mm\,s^{-1}$
α	1.22	0.43	1.22	0.43	1.00	-
ε_d	0.55	0.30	0.55	0.30	0.50	-
Re_c	0.014	0.014	0.042	0.042	0.055	-
Ca_c	0.004	0.004	0.005	0.005	0.005	-
We_c	$\ll 1$	$\ll 1$	$\ll 1$	$\ll 1$	$\ll 1$	-
Bo	0.004	0.004	0.003	0.003	0.005	-

A pulsation free syringe pump (Cetoni Nemesys) establishes the droplet volume flow rate Q_d and the continuous phase volume flow rate Q_c such, that the flow ratio $\alpha = \frac{Q_d}{Q_c}$ can be freely adjusted (Fig. 3.1a). At the flow-focussing (FF) junction the continuous phase squeezes the partially blocking droplet, to form a continuous Taylor droplet stream. The droplet fluid is seeded with Rhodamine B coated polystyrene (PS) tracer particles (microparticles GmbH) with a nominal particle diameter of $d_{part} = 1.3\,\mu m$. Both liquids are collected in a waste reservoir. An overview of the hydrodynamically relevant parameters applied in the experimental set for the verification of the interface approximation is given in Tab. 3.2. The relevant parameters for the μPIV investigation and the pressure reconstruction are given in Tab. 3.3.

The optical set-up is located $5\,mm$ downstream of the FF-junction (Fig. 3.1b). A frequency-doubled Nd:YAG laser with a wavelength of $\lambda_L = 532\,nm$ is used to excite the fluorescent tracer particles inside the droplet. The laser light is coupled into the light path of an inverted microscope (Zeiss AxioVert 100). A dichroic mirror reflects the laser light through the objective (LD LCI Plan-APOCHROMAT 25x/0.8) into the PDMS-channel. The fluorescent light emitted by the tracer particles has a peak intensity around a wave length of about $\lambda_{peak} = 600\,nm$ (Rhondamine-B). The depth of correlation of the objective determines the measurement plane thickness for the μPIV measurements of Chap. 5 to about $5\,\mu m$.

Tab. 3.3: Flow conditions of the μPIV experiment of the Taylor flow [83] (Chap. 5 and 6). Geometric parameters, fluidic and material parameters, and the governing dimensionless numbers are displayed. The refractive index matched material system is octanol and water/gylcerin for the disperse and the continuous phase respectively. The denomination is given in the list of symbols

Dimensionless numbers			Geometric parameters			Fluidic / material parameters		
Ca_c	0.0050	-	W_ch	104	μm	Q_d	1.5	$\mu\mathrm{l\,min^{-1}}$
Re_c	0.0511	-	H_ch	96	μm	Q_c	1.5	$\mu\mathrm{l\,min^{-1}}$
Oh	0.3107	-	A_ch	9984	$\mu\mathrm{m}^2$	Q_tot	3.0	$\mu\mathrm{l\,min^{-1}}$
Bo	0.0043	-	V_FF	1038336	$\mu\mathrm{m}^3$	$\bar{U}$	5.0	$\mathrm{mm\,s^{-1}}$
We_c	0.0003	-	A_r	1.08	-	u_d	4.7	$\mathrm{mm\,s^{-1}}$
Mo	0.0004	-	$L_\mathrm{d}/W_\mathrm{ch}$	1.58	-	η_d	0.021	$\mathrm{Pa\,s}$
α	1.0	-	$L_\mathrm{g}/W_\mathrm{ch}$	0.34	-	η_c	0.008	$\mathrm{Pa\,s}$
ε_d	0.5	-	$L_\mathrm{ch}/W_\mathrm{ch}$	500	-	ρ_d	1186	$\mathrm{kg\,m^{-3}}$
$\lambda = \eta_\mathrm{d}/\eta_\mathrm{c}$	2.625	-	$W_\mathrm{o}/W_\mathrm{ch}$	0.5	-	ρ_c	830	$\mathrm{kg\,m^{-3}}$
$\mathcal{K} = \rho_\mathrm{d}/\rho_\mathrm{c}$	1.427	-	$L_\mathrm{o}/W_\mathrm{ch}$	0.5	-	σ	0.008	$\mathrm{N\,m^{-1}}$

This tracer particle position-signal passes through the dichroic mirror towards a recording CCD-Camera (PCO SensiCam qe). Camera and laser are synchronized with the programmable timing unit of the PIV-system (LaVision). A piezo stepper (MIPOS500SG, Piezosystem Jena GmbH with a precision of 8 nm) precisely adjusts the z-position of the objective with respect to the x-y direction of the micro channel. Thus, the z-position of the focal plane can be controlled to scan through a representative measurement volume of the flow field in view.

3.2 Two-phase system

The curvature of a droplet interface causes optical distortions, when the refractive indices between disperse and continuous phases do not match (Fig. 3.2). Thus, it is necessary to use fluids with matching refractive indices (RI) [19, 84, 88, 90].

1-octanol is chosen as continuous phase (RI = 1.428). The RI of the droplet is adjusted to that of the continuous phase. The disperse phase is a mixture

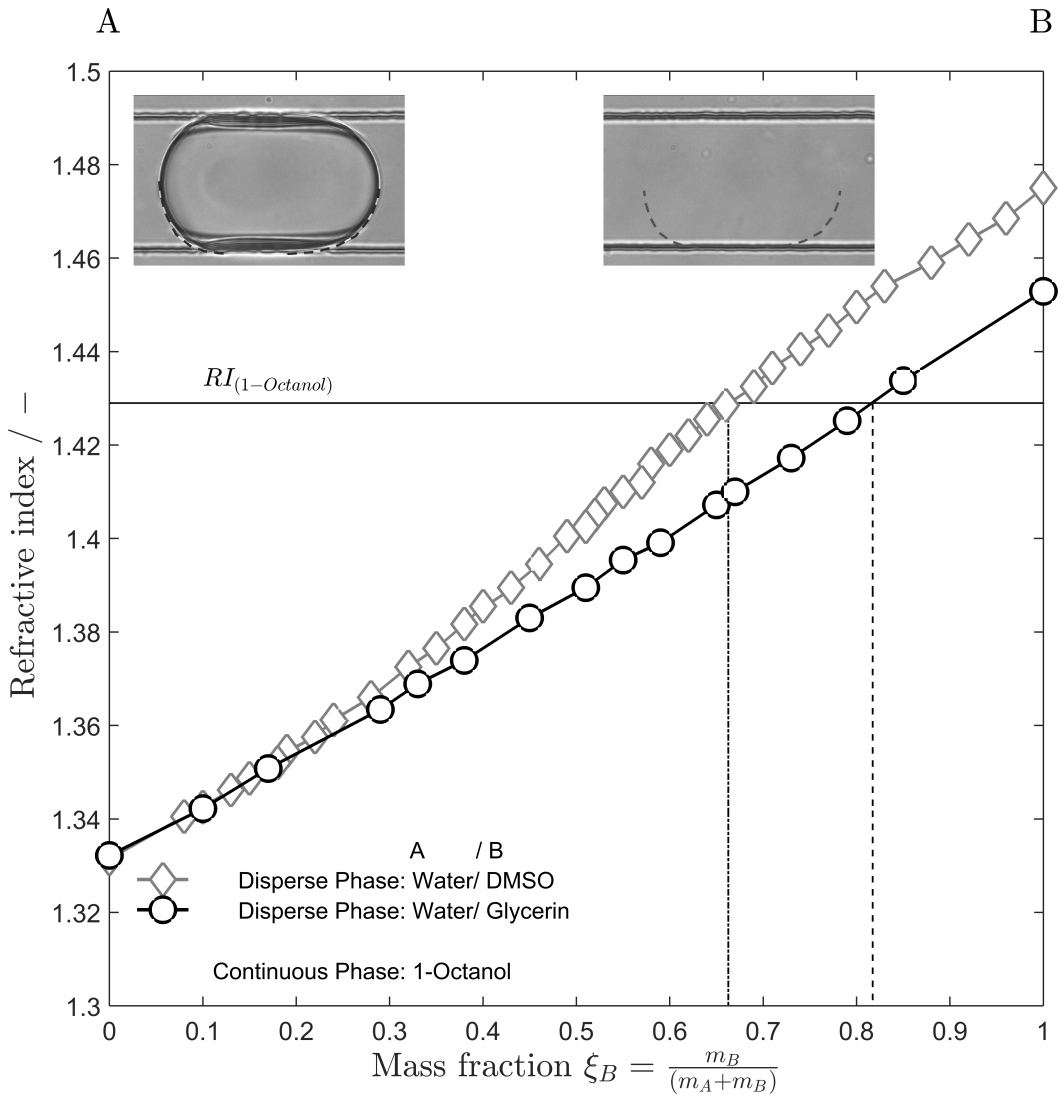

Fig. 3.2: The refractive index (RI) of the aqueous droplet is matched to the optical density of octanol as continuous phase by adding a sufficient mass fraction ξ_B of glycerin or DMSO. Thus, the curved interface does not influence the optical path.

Tab. 3.4: Material parameters of the liquids used are based on own measurements. Surface and interfacial tensions are obtained with the pendant drop method. All combinations are used for the validation experiments of the interface approximation. For the μPIV experiment only the combination of octanol and water/glycerin is used as disperse and continuous phase respectively

Material	RI -	Visc. $\mathrm{mPa\,s}$	Dens. $\mathrm{g\,mL^{-1}}$	Surf. Tens. (air) $\mathrm{mN\,m^{-1}}$	Interf. Tens. (Oct.) $\mathrm{mN\,m^{-1}}$
H_2O	1.333	0.9	1.00	72.7	7.8
Glycerin	1.474	1412.0	1.26	-	-
DMSO	1.476	2.0	1.10	44.6	2.6
Octanol	1.428	7.4	0.82	29.1	-
H_2O/ Gly.	1.428	22.1	1.18	69.1	5.9
H_2O/ DMSO	1.428	3.7	1.09	56,4	2.3

of water (RI = 1.333) and either glycerin (RI = 1.474) or dimethylsulfoxide (DMSO, RI = 1.476). Both materials can be used to tune the index of refraction of the droplet to the RI of 1-octanol. In case the matching has been performed successfully, no droplet interface is visible at the wavelength range of the fluorescent signal. The RI variation along the fluorescence emmission spectrum of Rhodamine B can be neglected. It amounts to 0.41% with respect to the RI of the Rhodamine B peak emission in water. Mixing the respective liquids does not exclusively result in a change of RI, but also affects the droplet viscosity, density and interfacial tension between the phases. An overview of the material properties is provided in Tab. 3.4.

3.3 Image acquisition and image processing

The symmetry of the Talyor flow in straight rectangular microchannels allows to conduct measurements in one half of the channel to reduce the amount of processed data. After initiating the flow, it takes about 2 minutes for droplet size fluctuation to reduce to a reasonable level. A ten-fold time ensures the decline of the initial fluctuation. After this transient of $20\,\mathrm{min}$, the flow is

considered to be quasi-stationary: for the moving droplets the flow inside and around each droplet is similar for all droplets.

The μPIV setup is not synchronized to the flow and freely records a number of 600 double frames per measurement plane. The measured Taylor droplet train exhibits a droplet size distribution that varies 10% in length. The recording frequency of PIV double frame images f_{rec} is fixed at $12\,\mathrm{Hz}$, while the droplet frequency oscillates around $f_{\mathrm{d}} \approx 14\,\mathrm{Hz}$. The temporal distance between the double frames is set to $1.5\,\mu\mathrm{s}$.

The depth of correlation determines the measurement depth of the optical setup to $5.4\,\mu\mathrm{m}$. A detailed consideration of the DOC is given in Sec. 3.4. Half of the channel height is divided into 11 equidistant ($\Delta H = 5.4\,\mu\mathrm{m}$) measurement planes to avoid recording redundant flow information. The chosen z-positions of the focal planes include the center symmetry plane and a measurement plane directly at the bottom cover of the microchannel.

Beginning with the center plane, the μPIV system is programmed such, that after recoding 600 images the piezzo stepper moves the objective and thus its focus to the next plane. The procedure is repeated until the measurement is completed at the bottom lid position of the microchannel. Fig. 3.3 shows a sketch of the measurement plane position with respect to the Taylor droplet interface.

Due to the asynchronous recording and the strong length variability of the observed flow, pre-processing of the recorded data is applied to receive a quasi-stationary representation of the velocity distribution inside and around an average Taylor droplet. The pre-processing involves image selection (e.g. a statistical approach to reduce the droplet length variation), processing (in-frame image shifting in x-y-direction) and vertical alignment (in z-direction). The method is explained in detail later in Sec. 3.3.2 and Sec. 3.3.3. The pre-processing reduces the droplet length deviation from 10% to about 3%. This increased precision enables to determine the droplet velocity at the stagnation points and allows to accurately change to a moving frame of reference with respect to the droplet motion.

For each measurement plane, the identified double images of suitable droplets are selected such that at least 60 image pairs are further processed. To increase the data density, the flow symmetry is used along the center axis

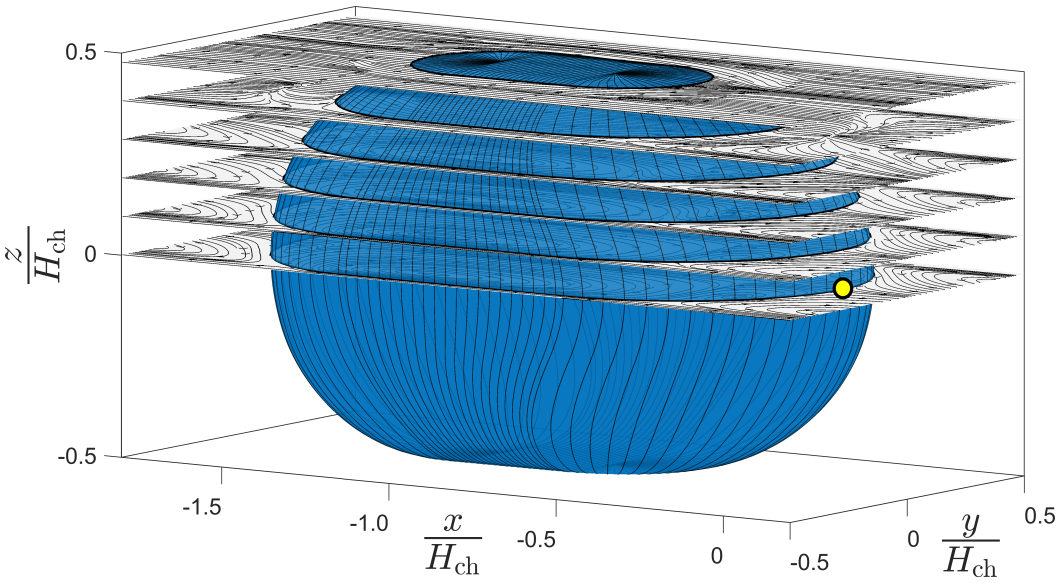

Fig. 3.3: Sketch of the measurement planes on which ensemble correlation μPIV is performed. For clarity only 6 out of 11 measurement planes are depicted. The approximate Taylor droplet model [82] (Chap. 4) indicates the position of the interface (light blue surface). The Taylor droplets translate in positive x-direction and the droplet's front tip is placed at the origin of the Cartesian coordinate system (yellow dot)

of the measured Taylor droplets. The selected image set is extended by additionally processing the mirrored data set in the μPIV-analysis. This results in at least 120 post-processed image pairs per measurement plane, which are subsequently evaluated with an ensemble correlation PIV algorithm.

3.3.1 Recording mode

Once the syringe pump has started, the volume driven Taylor flow establishes at the FF-junction and stabilizes. Depending on the volume flow ratio α or disperse phase fraction ε_{d} Taylor droplets of a certain length are formed. The parameter α is chosen such that the mean droplet length fits well within the field of view of the recording camera. It turned out that the effective field-of-view was insufficient to capture Taylor bubbles with L/W = 2. The length of the droplets is reduced to $\frac{L_{\mathrm{d}}}{W} = 1.66$.

The measurement plane thickness (DOC = $5.4\,\mu\mathrm{m}$) results 21 potential measurement planes along the z-direction between the bottom plane and the

channel top. Using symmetry conditions around the channel center, the amount of raw data can be reduced to 11 planes – beginning with the wall plane and successively shifting the focus towards the z-directional center plane of the microchannel. After the Taylor flow is established and stabilized, the camera records up to 600 images per measurement plane and the piezo stepper automatically translates towards the subsequent measurement plane.

In order to deal with the droplet length fluctuation and the resulting droplet shedding frequency fluctuation of the established continuous Taylor flow in combination with the asynchronous recording, a sorting and image-translation approach was applied in the post-processing of the image data to yield the quasi-instantaneous representation of an average Taylor droplet. The image processing is explained in Sec. 3.3.2 and Sec. 3.3.3.

3.3.2 In-plane image processing (xy-direction)

An average image of each z-position measurement plane is generated from about $i = 600$ initial source images $I(x, y, i)$. The mean perimeter shape is calculated from the average images of the particle distribution in order to enable a quantification of the spatial deviation of the model.

In a first step, each raw image (index i, Fig. 3.4a) is analyzed with respect to the droplet position in the image and the apparent length of the droplet $L_{\mathrm{d}}^{*}(i)$ (Fig. 3.4b). The apparent droplet length is determined by an analysis of the blurred fluorescence information of out-of-focus tracer particles. In order to reduce noise, the two-dimensional image is averaged normal to the main flow direction and a one-dimensional fluorescence intensity distribution in the main flow direction is calculated (Fig. 3.4b):

$$I^{*}(x,i) = \frac{\sum_y I(x,y,i) - \langle \sum_y I(x,y,i) \rangle_{\min}}{\left[\sum_y I(x,y,i) - \langle \sum_y I(x,y,i) \rangle_{\min} \right]_{\max}}. \tag{3.1}$$

Applying a dynamic threshold, the front and back ends are determined along with the droplet center position and the droplet length. In case the droplet front or back is detected too close to the image frame border the droplet

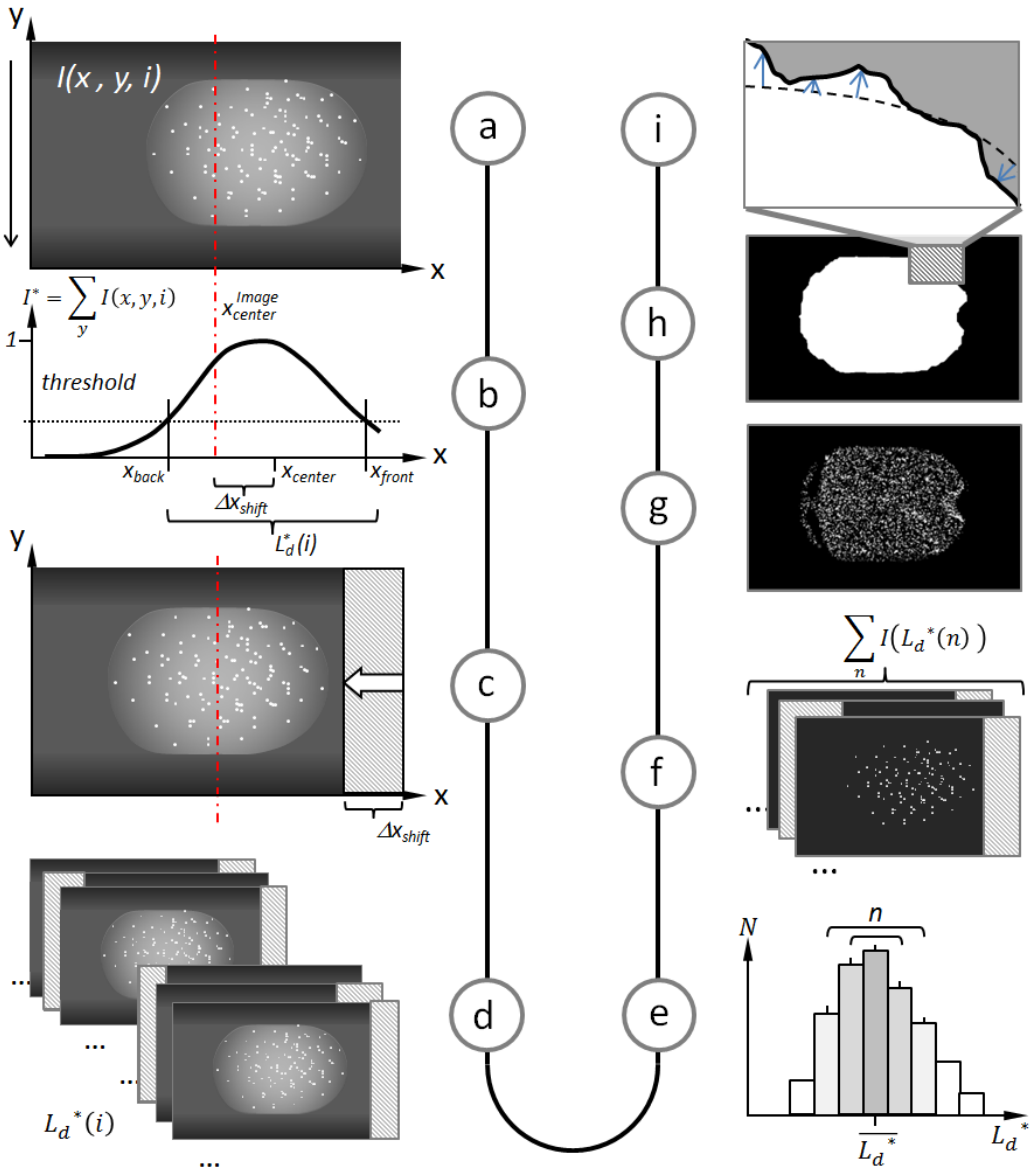

Fig. 3.4: Image processing pipeline. a-d) Single image processing: Intensity threshold analysis to locate the droplet within the image and to calculate its downstream off-set with respect to the image center $\Delta x_{\mathrm{shift}}$. e-i) Subsequent image averaging procedure using all tracer information for an in-plane droplet shape representation.

image is discarded. A margin of 15% of the image width W_{image} is sufficient to establish a stable evaluation performance. The droplet center position is shifted to the image center (Fig. 3.4c). Although the determination procedure of these droplet attributes offers a limited accuracy, it is sufficient for the upcoming sorting step (Fig. 3.4d), because the method relies on relative droplet information $L_{\mathrm{d}}^{*}(i)$.

Since the recorded Taylor flow does not produce mono-disperse droplets, the number distribution of the detected apparent droplet length allows to sort the droplet images such, that a minimum number of images is chosen around the peak of a droplet length histogram (Fig. 3.4e). With this strategy the flow related variation in apparent droplet length is decreased to a necessary minimum because the more images n are taken into account, the less accurate the result tends to be.

The fluorescent signal of the focused tracer particles is significantly brighter than the out-of-focus background intensity, and it contains precise information on the droplet shape in that measurement plane, since all located tracers are necessarily inside the droplet. After removing the low intensity background signal with a two-dimensional fast-Fourier transform (FFT) high-pass image filter, only the steep intensity gradients of the in-focus information remains in the n sorted images (Fig. 3.4f).

In order to increase the information density of the sparsely seeded droplet images, an average image of all droplets in a measurement plane is created (Fig. 3.4g). At least n = 70 – 100 images need to be collected to create an average particle image with sufficiently dense seeding information.

The last in-plane processing step uses binary image operations (dilation and erosion) to generate a continuous droplet perimeter shape: After normalizing the average image, thresholding leads to a binary representation of the droplet with a value of 1 labeling the droplet (Fig. 3.4h). Additional image dilation with a circle as structuring element closes occasional gaps in the binary droplet section.

Finally, the distance normal to the model contour of the corresponding measurement slice is calculated based on the nodes of the model grid. In this way a plane-by-plane quantification of interface shape model accuracy

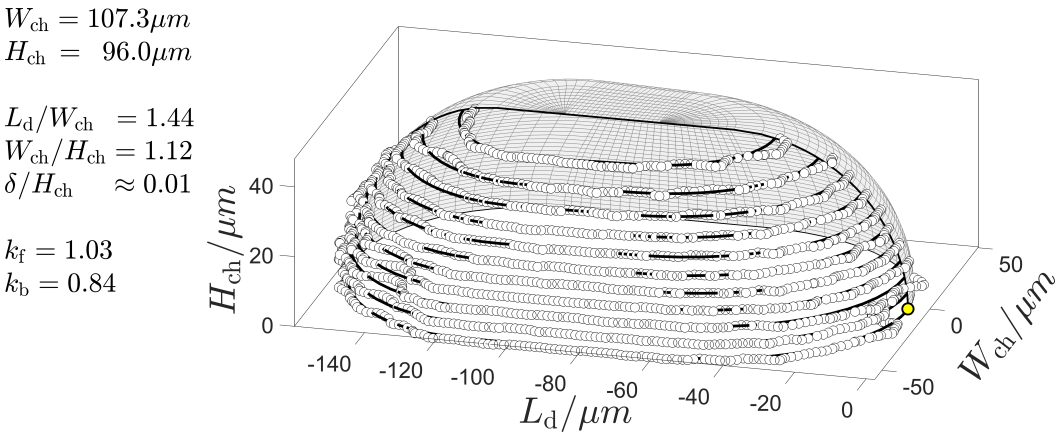

Fig. 3.5: Interface position comparison of measured and modeled Taylor droplet data. Qualitatively, the overall impression of the shape does agree well. The alignment procedure of the average tracer particle images in z-direction is valid.

as well as the assessment of the overall accuracy with respect to the entire droplet shape is possible (Fig. 3.4h).

3.3.3 Out-of-plane image alignment (z-direction)

After alignment of the different frames to the droplet center for each measurement plane, the summed images for each plane should be aligned appropriately along the direction normal to these planes (in z-direction). A comparison of the fluorescent out-of-focus signal of the sections through the tracer seeded droplets, shows that the background information is similar on all measurement planes.

Thus, the z-directional alignment of the frames for each measurement plane consists of a shift of the recorded droplet center towards the image frame center. Exemplary, the measurement results of the in-plane droplet section and the corresponding contour of the droplet shape model are shown in Fig. 3.5. The representation of the measured droplet surface is found to be sufficient for the following validation purpose.

3.4 Ensemble correlation µPIV

Particle image velocimetry, or PIV, refers to a class of methods used in experimental fluid mechanics to determine instantaneous fields of the vector velocity by measuring the displacements of numerous fine particles that accurately follow the motion of the fluid [6]. PIV is an optical measurement technique that is usually applied to transparent setups and flows. In standard macroscopic planar 2D2C PIV, a thin light sheet is formed inside the depth of focus of the flow observing digital camera. In a microscopy setup for μPIV, volume illumination of the flow in combination with a small depth of focus of the objective forms the thin measurement plane (Fig. 3.1). Two spatially calibrated raw images of the illuminated instantaneous particle distribution in the considered flow section are recorded with a well defined short temporal distance Δt.

The displacement of particles Δs between the two consecutive particle image frames is calculated with a cross-correlation algorithm: Both particle image frames are equally divided into small overlapping interrogation windows. The interrogation window size, position and overlap determine the spacial resolution of the resulting planar vector field. A cross-correlation between all corresponding interrogation windows of the first and second image frame calculates the most probable vector of spatial particle displacement. The respective correlation data for all interrogation window pairs is stored in a correlation map (correlation plane). A division of the received 2D2C vector field of displacement by the time interval Δt results an 2D2C velocity field of the flow in the measurement plane. In the presented setup, μPIV-measurements are repeated on several measurement planes throughout the flow volume to receive a 3D2D velocity field.

In microscopic flows the magnitude of Brownian motion can be considerably high with respect to the strength of the flow. Additionally, the introduction of image noise from the digital cameras impacts the particle image quality in the low light conditions of microscopy setups. To overcome these influences for the investigated quasi-stationary flow, an elevated number of image pairs is recorded, selected and processed (Sec. 3.3): On each measurement plane, the image pairs are evaluated using ensemble correlation [26]. The method relies on averaging coinciding correlation planes from a sequence of image

pairs of a stationary flow [95]. After passing through the post-processing (Sec. 3.3.2), the images fulfill this requirement. Stochastic influences such as Brownian motion are suppressed since randomly deviated correlation peaks are averaged out in favor of the recurring correlation peaks of the stationary flow. Additionally, this technique increases the information density of the sparsely seeded flows [6]. Depending on the particle density, Vennemann et al. [113] estimated 50 image pairs to be sufficient to obtain close to 100% reliable vectors (for interrogation areas of 64×64 px).

For the μPIV evaluation of this thesis, a cycle of decreasing square interrogation windows sizes [256 128 96 64 32 16 16] px was used with an overlap of 50% applying ensemble correlation for each iteration. The resulting vector field of each cycle is used as input information for the next iteration step. The last evaluation step is performed twice to further increase the accuracy of the resulting ensemble correlated vector field.

The depth of correlation (DOC) is $z_{\mathrm{corr},0} = 5.4\,\mu\mathrm{m}$ [68, 94, 100]. However, the flow in the setup is subject to shear: Olsen [92, 93] introduced an approximation to describe the shear dependency of the DOC. In-plane shear increases the DOC, while to a less extend out-of-plane shear decreases the DOC. The statistics of the in-plane shear (Fig. 3.6) show that the DOC-increase in the setup ranges between 1.12 and 2.35 at most, depending on whether 68% or 95% of the shear rate distribution data is included in the estimation.

An analysis of the correlation between the in-plane shear distribution of the downstream velocities and the reconstruction error distribution reveals, that the error increases with rising shear rates. In fact, the increase could be explained with the shear increase of the DOC. Anyway, given the relative low mean absolute reconstruction error presented in Sec. 3.5.2, the change of the DOC due to shear is acceptable and the chosen measurement plane distance is valid.

Evaluating the particle image data sets of all measurement planes results in a 3D2C velocity distribution with an in-plane spatial resolution $\Delta x = \Delta y = 1.8\,\mu\mathrm{m}$ and an out-of-plane distance of $\Delta z = 5.4\,\mu\mathrm{m}$. The number of measurement nodes of $171 \times 71 \times 11$ amounts to 133551 regularly spaced vectors in one of the symmetric halves of the quasi-stationary Taylor flow.

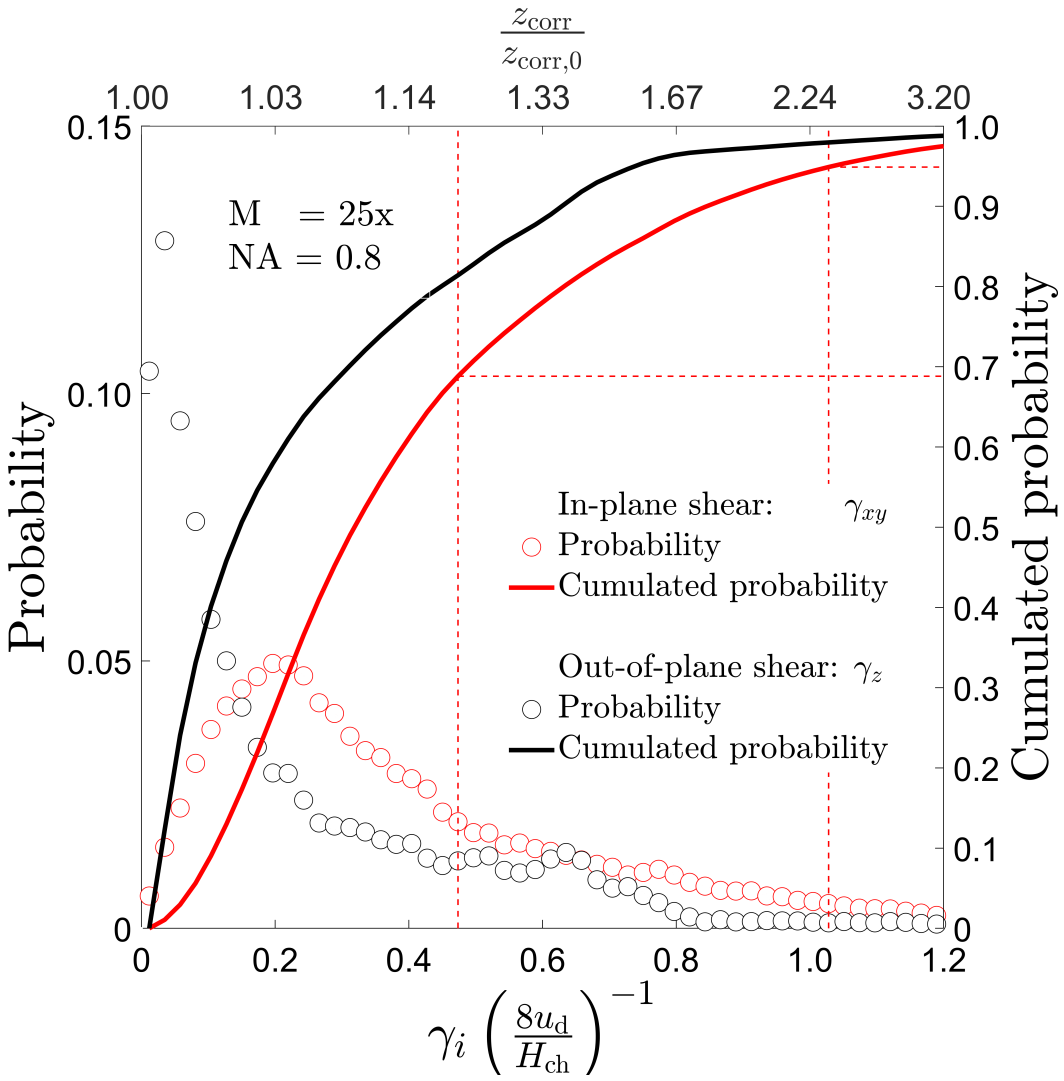

Fig. 3.6: Based on the probability distribution of the in-plane shear rates (red) on the left y-axis, the cumulated probability on the right y-axis allows to estimate the amount of included values of the shear rates distribution. The bins of the shear rate distribution (x-axis) are converted into the shear related depth of correlation (DOC) variation [93], to simplify the reading of the graph

3.5 The out-of-plane velocity component

The μPIV measurement delivers a 3D2C velocity field, which lacks the third velocity component w in z-direction. In the following the reconstruction of the missing velocity is described and a assessment of the accuracy of the method is provided.

3.5.1 Reconstruction of the velocity z-component (w)

The reconstruction method retrieves the missing velocity component based on the available measured 3D2C field information. The 2D in-plane velocity components u and v are used in the continuity equation for incompressible flows. A 2nd order central difference scheme delivers the derivatives of the 2D velocity field [6].

Beginning with the supposedly divergence-free symmetry plane (i.e. with $dw/dz = 0$ and $w = 0$) of Taylor droplets and proceeding towards the bottom cover of the microchannel, the integration of the divergence in z-direction delivers an estimate for the out-of-plane velocity component w. A more detailed description of the method is given by Brücker [16, 17] and Robinson and Rockwell [98]. No boundary condition for the velocity in z-direction at the cover is imposed. Instead, the deviation from $w = 0$ allows to asses the accuracy of the reconstruction.

Prior to reconstruction, an approach based on the normalized median test [120, 121] is applied to detect, remove and replace outliers of the measured velocities u and v and their derivatives. Additionally, a 2D median filter with a 3×3 neighborhood for velocities and a 5×5 neighborhood for the derivatives is applied to suppress random noise [6, 119].

3.5.2 Validation of the reconstructed 3D3C flow field

The validation of the reconstruction is segmented in three steps. First, a quantitative analysis is conducted based on a comparison of the probability density distributions of the velocity components. Secondly, a quantitative

measure for the reconstruction accuracy is established and investigated. Finally, the conservation of volume allows to quantitatively evaluate the overall accuracy of the reconstruction of the out-of-plane velocity component w.

Qualitative assessment

The transverse velocities v (measured) and w (reconstructed) are considered to be symmetric for a perfect aspect ratio of $A_\mathrm{r} = 1$. Therefore, a comparison of the probability density distribution (PDF) of the transverse velocities (Fig. 3.7) offers a visual qualitative impression of the reconstruction accuracy. The shape of the probability density function representing the reconstructed velocities (red solid line) is similar to that of the measured component (black solid line). The deviations between the peaks and the flanks are attributed to the measurement uncertainties and the reconstruction.

The PDF of the normalized stream-wise relative velocity (black dotted line) represents measurement data only. The two peaks at a normalized velocity amplitude of -1 and 0 are related to the velocities at the wall and the stagnation regions of the flow, respectively. The broad positive and negative flanks of the graph result from the bi-directional stream-wise flow of the main wall-driven vortices inside and outside the Taylor droplet.

Quantitative assessment of the velocity field

The symmetry of the flow enables to compare the measured y-components in the first quadrant of the cross section ($+y$, $+z$) with the reconstructed z-component of the second quadrant ($-y$, $+z$): Rotating the measured 2D velocity field by +90° and performing a linear interpolation of the rotated measured transverse velocity component on the grid of the reconstructed velocities gives $v^\perp$. Subtracting the measured values from the reconstructed velocity components in quadrant two results a 3D residue distribution, that serves as an estimate of the reconstruction accuracy:

$$\mathcal{R} = \frac{\left(w - v^\perp\right)}{u_\mathrm{d}}$$

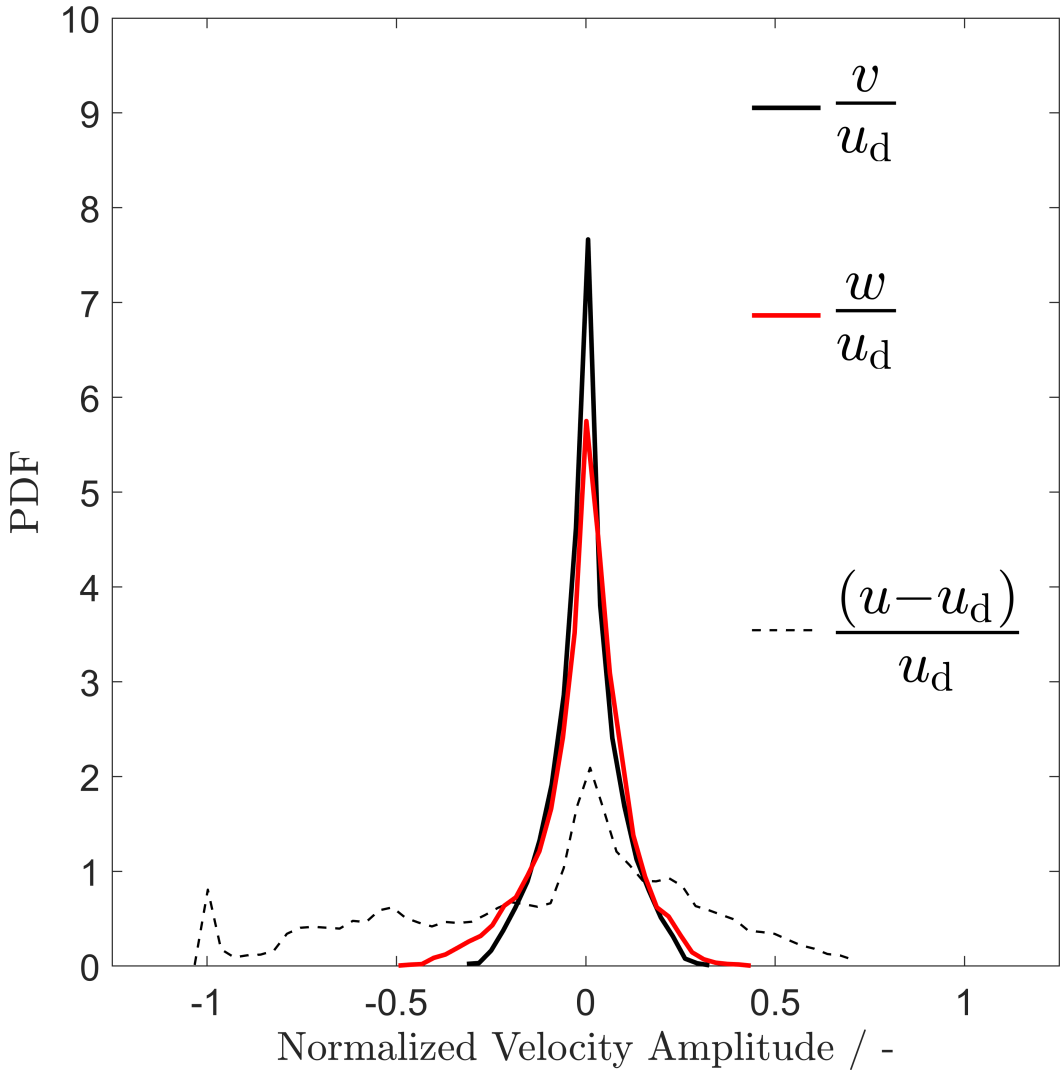

Fig. 3.7: Normalized velocities u (stream-wise direction, measurement), v (transverse direction, measurement), w (transverse direction, reconstruction). Qualitatively, the PDF of the reconstructed transverse velocity is similar to the measured transverse component PDF. The deviations at the peak and the flanks are at first attributed to the measurement uncertainties, the median filter application and the calculation of the derivative used for the reconstruction

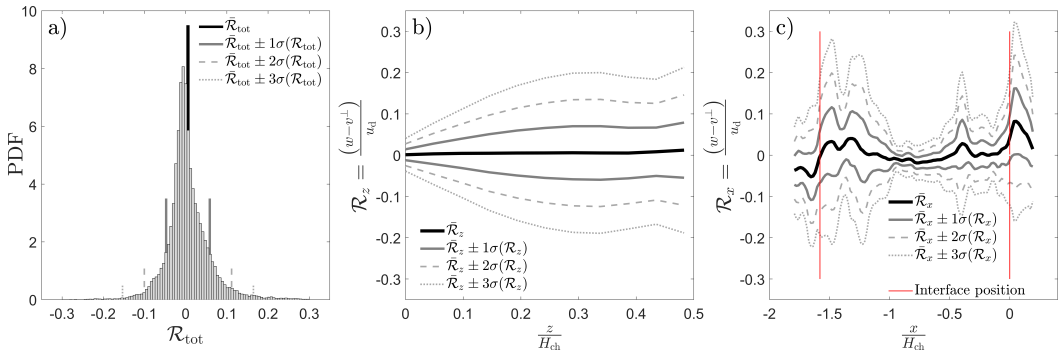

Fig. 3.8: Quantification of the reconstruction error. a) Probability density distribution (PDF) of the residue in the entire domain. The total mean reconstruction error amounts to $\bar{\mathcal{R}}_z \pm 1\sigma(\mathcal{R}_z) = 0,6 \pm 5.3\%$. b) Mean residue $\bar{\mathcal{R}}_z$ distribution and its standard deviation in dependence of the channel height $\frac{z}{H_{\mathrm{ch}}}$. c) Mean residue $\bar{\mathcal{R}}_x$ distribution and its standard deviation in flow direction $\frac{x}{H_{\mathrm{ch}}}$

The overall reconstruction accuracy of the domain is expressed as a probability density function (Fig. 3.8a) and it is estimated to be $\bar{\mathcal{R}}_z \pm 1\sigma(\mathcal{R}_z) = 0,6 \pm 5.3\%$. A perfect reconstruction would result a mean value and a standard deviation of zero. Thus the general reconstruction process works well. However, considering 95% (2σ) of all residues, the reconstruction shows a deviation of $\pm 10.6\%$.

Fig. 3.8b shows the mean residue $\bar{\mathcal{R}}_z$ and its standard deviation in dependence of the channel height $\frac{z}{H_{\mathrm{ch}}}$. The residue grows with the distance to the xy-symmetry plane. The maximum deviation can be found at a channel height of $\frac{z}{H_{\mathrm{ch}}} \approx 0.30$, where the maximum out-of-plane velocities in z-direction are found.

Analyzing the mean reconstruction error in flow direction (Fig. 3.8c) shows again the relation between the amplitude of the out-of-plane velocity and the reconstruction error. At the cap regions (red lines), the strong out-of-plane motion coincides with an increased error. At the center of the main vortex less out-of-plane movement is present, which results a decreased error.

Sec. 3.4 stated that the depth of correlation (DOC) is dependent on the shear of the flow. Plotting the reconstruction residues versus the according in-plane shear rates allows to analyze the magnitude of the effect in the presented experiment. Fig. 3.9 is based on a 2D-histogram of the reconstruction error (x-axis) and the normalized shear rate distribution (y-axis). For each shear

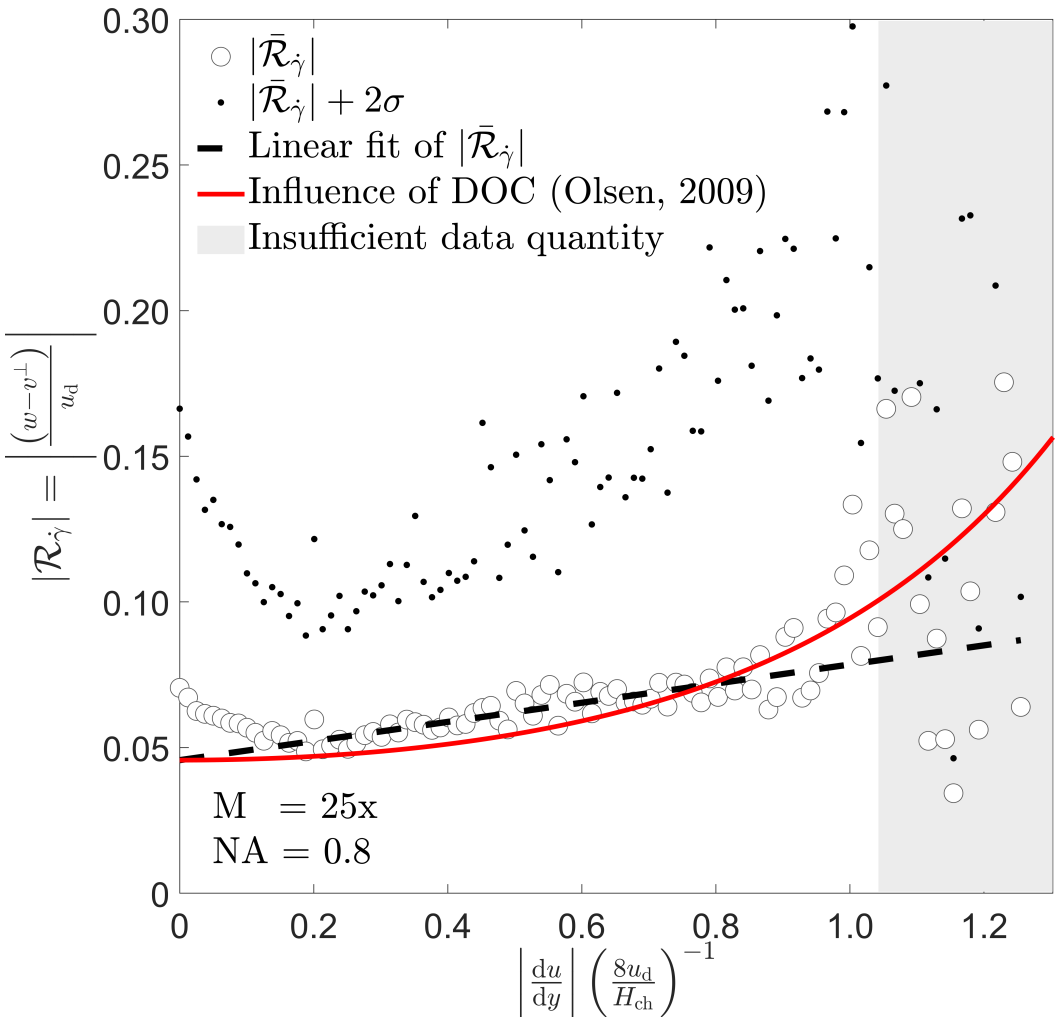

Fig. 3.9: Correlation of the reconstruction residues and the according in-plane shear rates. Shear could be reason the rising mean absolute reconstruction error. The rate of change is similar to the influence suggested by Olsen [93]

rate bin the mean reconstruction residue (○) and its standard deviation is calculated (•). The gray area indicates a region of high shear with insufficient data quantity. The mean error rises linearly from 5.2% to 7.2% between a normalized shear of 0.2 and 0.8 respectively. As comparison the model of Olsen [93] for the shear influence on the DOC is applied, transformed and added to the graph (red line). The influence of shear on the DOC is identified to be a possible reason for the observed evolution of the mean absolute reconstruction error.

Quantitative assessment of the volume flows

An analysis of the stream-wise and transverse volume flow inside and outside the Taylor droplets in Fig. 3.10 confirms the coherence of the measured flow data. The mean volume flux distribution Q_x, Q_y and Q_z along the center axis of the channel is calculated with the reconstructed 3D3C absolute velocity field and the corresponding reference areas $\mathrm{d}A_x = \Delta y \Delta z$, $\mathrm{d}A_y = \Delta x \Delta z$ and $\mathrm{d}A_z = \Delta x \Delta y$. The mean volume fluxes in x-direction (Fig. 3.10 a), y-direction (Fig. 3.10 b) and z-direction (Fig. 3.10 c) are non-dimensionalized with the superimposed total volume flow $(Q_{\mathrm{tot}} = Q_{\mathrm{d}} + Q_{\mathrm{c}})$. The total volume flow of a direction is marked blue, while the continuous phase and the disperse phase are shown as black and red lines respectively. The volume flux $Q_{i,\mathrm{c}}$ and $Q_{i,\mathrm{d}}$ of each of the two phases is extracted by applying the approximate interface model as an logical discriminator [82] (Chap. 4).

The measured mean stream-wise volume flux distribution along the x-axis is given in Fig. 3.10 a). The blue graph corresponds to the superficial volume flux in x-direction, while the black and red graph depicts the mean continuous and mean disperse phase flux per channel cross section respectively. The mean superficial volume flow deviates with -5.56% at most from the nominal flow rate, which is set by the syringe pumps ($Q_{\mathrm{tot}} = 3.0\,\mu\mathrm{l\,min}^{-1}$). Ruling out defective equipment or leakage flow, the deformation of the channel material (polymethyldisiloxane - PDMS) explains the deviation. Taylor droplets are found to exert pressure peaks to the wall while passing [2] and the ductility of the channel material allows the wall to subside, while being pressurized [31]. Thus, the pressure drop related channel expansion causes a decrease of the mean velocity: the microchannel dilates. When recalculating the volume flux Q_i from the flow field by applying the reference areas $\mathrm{d}A_i$, the volume flow per cross section appears to be too small. Assuming a correct measurement procedure, this relates to an estimated cross section expansion rate of 2.9% in channel width $(3.3\,\mu\mathrm{m})$ and height $(2.8\,\mu\mathrm{m})$.

Proceeding along the x-axis towards the droplet's back cap (Fig. 3.10 a), the volume flux of the continuous phase (black graph) decreases as the droplet phase (red graph) occupies more space. The volume flux in the gutter and in the wall film is present as well: the dimensionless volume flow of continuous phase never drops below 2.1% at $\frac{x}{H_{\mathrm{ch}}} \approx -1$. Towards the droplet tip the

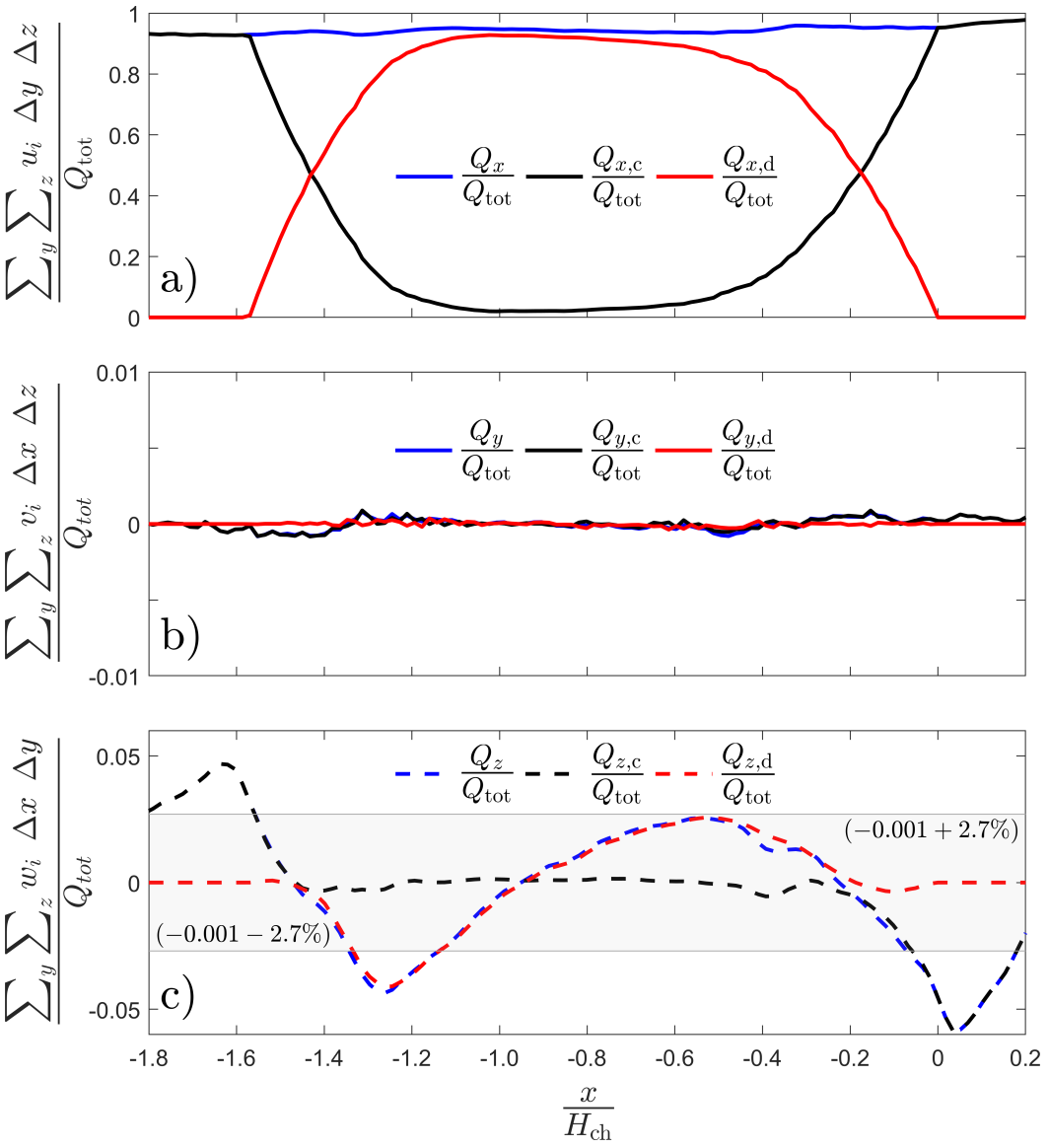

Fig. 3.10: Analysis of the dimensionless volume flow in stream-wise $Q_{x,i}/Q_{\mathrm{tot}}$ and in transverse direction inside and outside the Taylor droplets ($Q_{y,i}/Q_{\mathrm{tot}}$ and $Q_{z,i}/Q_{\mathrm{tot}}$) to demonstrate the coherence of the flow data. Depicted are volume flows occurring through cross sections perpendicular to the main flow direction (along the x-axis). The total volume flow ($Q_{\mathrm{tot}} = Q_{\mathrm{d}} + Q_{\mathrm{c}}$) is expected to match the measurement volume flow measurement in x-direction ($Q_x/Q_{\mathrm{tot}} = 1$), while the volume flows in transverse direction are expected to be zero due to conservation of mass ($Q_y/Q_{\mathrm{tot}} = Q_z/Q_{\mathrm{tot}} = 0$). The indices d and c refer to the disperse and continuous phase respectively. The stream-wise volume flux a) and the transverse volume flux in y-direction b) represent the results of the 3D2C μPIV measurement, while c) depicts the reconstructed transverse out-of-plane volume flux in z-direction. The stream-wise flux deviation is attributed to the channel deformation $(94.44\% \pm 1.2\%)\, Q_{\mathrm{tot}}$, while the deviation in y-direction highlights the accuracy of the μPIV measurement. The reconstruction of the third velocity component carries a standard deviation of $\pm$ 2.7% of Q_{tot} along the longitudinal axis of the droplet.

volume flux development reverses until only continuous phase is present from $\frac{x}{H_{\mathrm{ch}}} > 0$ on.

Fig. 3.10 b) shows the mean transverse volume flux in y-direction along the Taylor droplet main axis, that is expected to be zero. All fluctuations in y-direction remain below 0.1%. This consideration reflects the measurement error introduced by the applied μPIV measurement technique.

The mean volume flow based on the reconstructed (dashed lines) transverse velocity component in z-direction is shown in Fig. 3.10 c). Due to the symmetry of Taylor flows, the mean flux per cross section is expected to cancel out. However, the mean residual flux amounts to $-0.001\% \pm 2.7\%$ of Q_{tot}. The maximum deviation amounts to -6% of Q_{tot}. The result reflects the accuracy of the applied reconstruction method, since the measurement planes are carefully positioned with respect to the symmetry planes of the microchannel. The subdivision of the channel volume into disperse and continuous phase reveals that the deviation is located in both phases.

The error sources are identified to be the data filter (low pass filter for data noise) and the determination of the derivatives (which acts as a high pass filter for data noise) in addition to the dilation of the PDMS microchannel. From this analysis, the standard deviation of the reconstruction error is $\pm 2.7\%$ of the total volume flux Q_{tot}, which is half as big as the reconstruction error estimation in Fig. 3.8. The difference results from the integration step taken to derive the absolute volume flow.

4

Modeling the Taylor droplet interface

Once there were some particles
Being lonely and anarchical
Intensely loved an interface
- liked strongly to adhere
Never could I break that brace
- even not with shear
That bond is quite remarkable

This chapter presents a geometric model to approximate the interface shape of Taylor bubbles and droplets moving in rectangular micro channels. In order to deduce the entire 3D interface geometry the following a-priori knowledge is required: the cross sectional channel geometry, the droplet/ bubble length and the flow related front and back cap deformation ratios retrieved e.g. from instantaneous images of translating interfaces. The accuracy of the interface shape model is benchmarked with experimentally generated average images of the statistical distribution of a particulate tracer. In the experiment, the fluidic material system, the aspect ratio of the channel cross section and the droplet/ bubble length is varied. The mean overall deviation between the model and the experimental data remains below 2%. The interface shape model is applicable for horizontal pressure-driven liquid-liquid and gas-liquid fluid systems in a range of $Ca_c < 0.01$, $Re_c \lesssim 1$ and $Bo \ll 1$ with the liquid continuous phase wetting the wall. The model can be applied e.g. to guide the 3D flow field reconstruction of multiplane μPIV-measurements of Taylor flows.

4.1 Overview

A number of microfluidic applications employ two-phase flows using either the continuous phase or the disperse phase of Taylor flows to implement thermal [52, 67, 76], chemical [35, 60, 110] or biological processes [69, 123]. Chou et al. [22] published a recent overview on Taylor flow applications. The validity range of the approximation is in the scope of dimensionless numbers, which is addressed in theoretical work on microscopic Taylor flow [**V lahovska.2019**, 9, 25].

For modeling purposes the volume and surface area is usually deduced e.g. from optical images. Musterd et al. [87] delivered a detailed method to extract this information from various commonly used channel geometries, including a rectangular cross section. Their work assumes static flow conditions (non-moving droplets/ bubbles) to calculate the droplet/ bubble shape. Please note that in the following when referring to 'droplets' also gas-liquid fluid systems are addressed.

In droplet-based microfluidics, the droplet shape is strongly related to the pressure drop during the transport of droplet trains [78]. For low capillary numbers $Ca_\mathrm{c} = \frac{u_{0,\mathrm{tot}}\eta_\mathrm{c}}{\sigma}$ the surface tension forces dominate the viscous forces. The droplet front and back caps are deformed from their static spherical shape when set into motion, due to the fluid forces exerted on the interface.

The accuracy of the interface shape model is benchmarked with particle images of a Taylor flow investigation at a capillary number $Ca_\mathrm{c} = 0.005$. The material system of the two-phase flow is varied as well as the aspect ratio A_r of cross sectional channel geometry and the droplet length L_d.

The purpose of this geometrical interface approximation is to establish model-based guidance for the 3D flow field reconstruction for multiplane μPIV-measurements of Taylor flows. Thus, extensive CFD-modelling may be avoided in favor of the presented analytical approximation. Furthermore, the interface can be used e.g. to derive an analytical model for the relative velocity of the droplets with respect to the total superficial flow velocity [1, 5, 43, 70].

4.2 Modeling approach

Taylor droplets in rectangular micro channels do not occupy the entire cross section of the channel [60]. The remaining fraction of continuous phase in the channel corner is referred to as gutter [107]. The interface curvature in the longitudinal direction of the gutter is assumed to be negligible and propose a straight connection between the gutter entrances. The perpendicular interface curvature at the gutter cross section is assumed to be circular [87]. This curvature can be expressed as the inverse of the local radius, named gutter radius R_{g}. Thus at this location, solely the gutter radius itself relates to the Laplace pressure via the interfacial tension σ.

The dynamic interface shape of moving Taylor droplets is not only linked to the channel geometry and the free surface energy but also to flow-induced forces [78]. The presence of the curved interfaces (caps) between translating immiscible fluids causes flow deflection and recirculation in a frame of reference moving with the droplet velocity. This change of flow direction inside and outside the droplet exerts forces onto the interface. For surfactant-free materials (gases/ liquids), the deformation of the droplet caps is directly related to the interaction of the surface tension with the fluid forces normal to the interface, while tangential fluid forces induce surface movements. Thus, the actual droplet length determines the location of the flow deflection at the caps, but not their deformation.

The wall film related forces determine the wetting conditions of the continuous phase and thickness of the deposited fluid. Kreutzer et al. [62] provide a description to assess the de-wetting conditions of the wall film. For the investigated case optimal wall wetting of the bulk phase and a regular deposition of the Landau-Levich-Bretherton films with an evenly distributed wall film thickness is assumed. The reported dimple between the gutter and the thin film is neglected in the model to reduce complexity. Sobieszuk et al. [105] summarize models of the lubricating liquid film at the channel walls and the thickness of the gutter, which they refer to as the diagonal film thickness.

The correlations of Han and Shikazono [37] describe the dimensionless side wall film thickness δ/H_{ch} of Taylor flows in rectangular channel geometries in case of low Reynolds numbers $Re_{\mathrm{c}} = \frac{\rho_{\mathrm{c}} u_{0,\mathrm{tot}} H_{\mathrm{ch}}}{\eta_{\mathrm{c}}}$, where ρ_{c} denotes the density

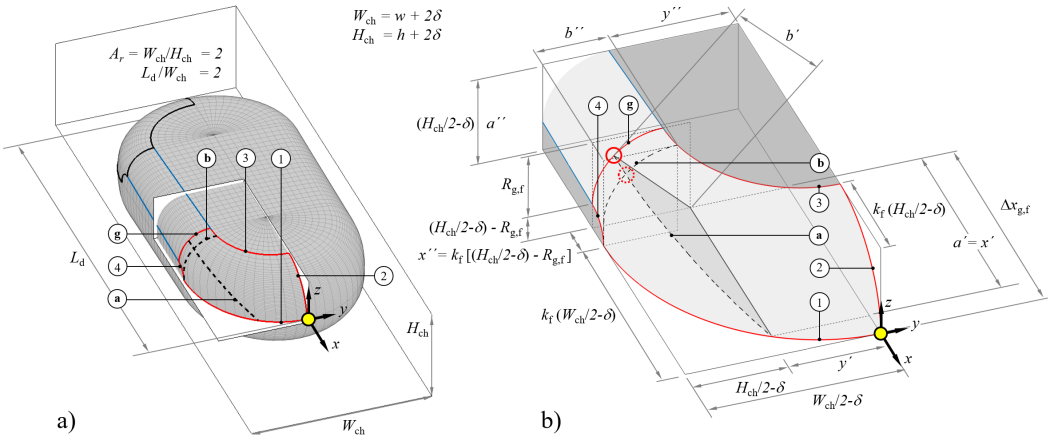

Fig. 4.1: Droplet sketch to locate and estimate the gutter radius at the droplet front $R_{g,f}$. A droplet with an aspect ratio ($A_r = \frac{W_{ch}}{H_{ch}} = 2$) and a length ratio $\frac{L_d}{W_{ch}}$ of 2 is depicted. In the droplet overview a) the boundaries of the frontal cap, the back cap and the gutter surface are delimited with red, black and blue lines respectively. Lines 1-4 and g define a quarter of the front cap and are supported by the lines a and b to derive the frontal gutter radius $R_{g,f}$ (line g). The yellow dot marks the origin of the coordinate system. The droplet motion is directed in positive x-direction. Exemplary, excerpt b) details the quartered frontal droplet section to support the derivation of the gutter radius. The circles indicate the nodes used approximately equate Laplace pressures.

of the continuous phase. The surface tension forces dominate viscous forces ($Ca_c \ll 1$) which in turn prevail the inertial forces ($Re < 1$). The Bond number $Bo = \frac{\Delta\rho g H_{ch}^2}{\sigma} \ll 1$ is small, since buoyancy effects are suppressed due to the channel dimensions.

In Fig. 4.1 a sketch of the droplet interface is given to detail the geometry. Three interface regions are defined for the derivation of the model. The blue region depicts the area, where the Laplace pressure Δp geometrically depends on the gutter radius only. The red region shows the front cap (index i = f) of the droplet, where the Laplace pressure depends on two principal radii. The black region is the back cap of the droplet (index i = b), where the geometrical conditions are similar to those of the front cap. Unless otherwise stated, the calculations for the front and back cap are treated analogously.

For derivation purposes, only the front of the droplet is entirely depicted and the blue (gutter) and red regions (front cap) are considered: The line g indicates the border between the gutter and the front cap (blue and red region). Line a and b are supporting lines, that are defined later. The Laplace

pressure $\Delta p_{\mathrm{g},i}^{j}$ at the intersection of line g and line a depends on the gutter radius alone. This location is the gutter entrance (solid circle, Fig. 4.1b). The index j relates either to the static or the dynamic droplet shape ($j = \mathrm{stat}$ or dyn).

The intersection of the supporting lines a and b defines a proximate position in the red region, where the Laplace pressure $\Delta p_{ab,i}^{j}$ depends on two principal radii of the front cap (dashed circles, Fig. 4.1b). Both Laplace pressures are considered to be equal due to their spatial vicinity.

$$\Delta p_{ab,i}^{j} \approx \Delta p_{g,i}^{j} \tag{4.1}$$

Later in the description of the model, the differences of the Laplace pressure between the static and the dynamic case (Eq. 4.2) allow to derive the dynamic gutter radii R_i^{dyn} as a function of the droplet length L_{d}, channel width W_{ch} and the below defined cap deformation ratio k_i.

$$\left(\Delta p_{ab,i}^{\mathrm{stat}} - \Delta p_{ab,i}^{\mathrm{dyn}}\right) \approx \left(\Delta p_{\mathrm{g},i}^{\mathrm{stat}} - \Delta p_{\mathrm{g},i}^{\mathrm{dyn}}\right) \tag{4.2}$$

Following Stone and Leal [108], the shape of the cap in the x-y plane at z=0, i.e., the symmetry plane in the z-direction, is approximated as an ellipse (line 1). Line 2 is the elliptical contour approximation in the symmetry plane in y-direction, respectively. In the static case, lines 1 and 2 reduce to circles with the radii $W_{\mathrm{ch}}/2$ and $H_{\mathrm{ch}}/2$. They limit the elliptical description for the static case.

The ellipse line 1 of the droplet cap is described by the semi-major axis $a_{1,i}$ and the semi-minor axis $b_{1,i}$. The ratio of the two axes specifies the cap deformation from the static circular shape. The flow field exerts forces onto the cap and evokes the deformation. In the following, this geometrical proportion is called cap deformation ratio k_i^j (Eq. 4.3). This deformation ratio has the same value for the z- and y-direction, i.e. for line 1 and 2. This assumption especially holds true for channels with aspect ratio $A_{\mathrm{r}} = 1$.

Furthermore, the deformation ratio are also applied for the lines 3 and 4, describing the shape of the onset of the top and side wall films.

$$k_i^j = \frac{a_{1,i}}{b_{1,i}} \approx \frac{a_{2,i}}{b_{2,i}} \approx \frac{a_{3,i}}{b_{3,i}} \approx \frac{a_{4,i}}{b_{4,i}} \tag{4.3}$$

Under static conditions (i.e. in the absence of a flow) the ellipses indicated by line 1-4 assume circular shapes and their corresponding deformation factors reduce to 1. As soon as the flow exerts forces on the droplet interface (dynamic conditions), the droplet back compresses and the droplet front elongates in flow direction:

$$\begin{aligned} \text{static} : k_i^j &\rightarrow k_\mathrm{f}^\mathrm{stat} = k_\mathrm{b}^\mathrm{stat} \rightarrow 1 \\ \text{dynamic} : k_i^j &\rightarrow k_\mathrm{f}^\mathrm{dyn} > 1 \\ k_i^j &\rightarrow k_\mathrm{b}^\mathrm{dyn} < 1 \end{aligned}$$

Implicitly, the following assumptions and simplifications are made to estimate the gutter radii at the front $R_{\mathrm{g,f}}^{\mathrm{dyn}}$ and the back $R_{\mathrm{g,b}}^{\mathrm{dyn}}$ of a moving droplet:

- The adjacent flow fields of the droplet interface are stationary.
- Momentum transport normal to the interface changes the droplet shape from its static shape at rest. The fluid flow is the source of deviation from the static shape.
- The general interface contour in the symmetry planes (xy & yz) can be approximated using an elliptical description.
- Channel height H_{ch}, channel aspect ratio A_{r}, disperse phase length L_{d} and the front and back cap deformation ratios k_{f} and k_{b} of in the $z = 0$ center plane are known - either by experiment (images), a correlation or other eligible sources.
- The elliptical deformation observed in the $z = 0$ center plane is transferable to the $y = 0$ symmetry plane and the border geometry of the wall films.

- The osculating circles of the ellipses vertices and co-vertices are sufficient to estimate the curvature of the neighboring surface elements (Fig. 4.1 a), intersection of the lines a-b and a-g) for a Laplace pressure balance.
- The Laplace pressure difference of those neighboring interfacial points is negligible.
- The interfacial tension σ is constant in the proximity of the gutter entrance.

The Laplace pressure difference across the interface of the static and dynamic flow condition at the gutter entrance in Eq. 4.2 is approximated with the following principle radii of the sectional ellipse of the lines a and b (Fig. 4.1a).

$$\Delta p_{ab,i}^{j} = \sigma \left(\frac{1}{R_{a,i}^{j}} + \frac{1}{R_{b,i}^{j}} \right) \tag{4.4}$$

At the beginning of the gutter (line g, Fig. 4.1a) the surface curvature is composed of the gutter radius $R_{\mathrm{g},i}$ alone.

$$\Delta p_{\mathrm{g},i}^{j} = \sigma \left(\frac{1}{R_{\mathrm{g},i}^{j}} \right) \tag{4.5}$$

Applying Eq. 4.4 and 4.5 to Eq. 4.2 and marking the respective static and dynamic terms produces ultimately an implicit description of the dynamic gutter radius.

$$\begin{aligned} 0 \;=\; & + \left(\frac{1}{R_{a,i}^{\mathrm{stat}}} - \frac{1}{R_{a,i}^{\mathrm{dyn}}} \right) \\ & + \left(\frac{1}{R_{b,i}^{\mathrm{stat}}} - \frac{1}{R_{b,i}^{\mathrm{dyn}}} \right) \\ & - \left(\frac{1}{R_{\mathrm{g},i}^{\mathrm{stat}}} - \frac{1}{R_{\mathrm{g},i}^{\mathrm{dyn}}} \right) \end{aligned} \tag{4.6}$$

Note, that the solution is independent of the interfacial tension σ. Thus, the solution for the gutter radii is considered to hold also for flows in the presence dilute surfactant load as long as the interfacial tension gradients are small at the gutter entrances. The application of a zero-finding algorithm results in the dynamic gutter radii, which are used in the later described construction of the 3D droplet interface.

Relating the gutter radius $R^j_{\mathrm{g},i}$ to the droplet height $(H_{\mathrm{ch}} - 2\delta)$, a non-dimensional gutter radius is defined.

$$k^j_{\mathrm{g},i} = \frac{R^j_{\mathrm{g},i}}{H_{\mathrm{ch}}\left(1 - \frac{2\delta}{H_{\mathrm{ch}}}\right)} \tag{4.7}$$

The wall film thickness δ and the diagonal film thickness of the gutter δ_{g} presented by Han and Shikazono [37] are used to derive a theoretical estimation of a mean non-dimensional gutter radius:

$$k^j_{\mathrm{g,theo}} = \frac{\left(\frac{\delta_{\mathrm{g}}}{H_{\mathrm{ch}}} - \frac{\delta}{H_{\mathrm{ch}}}\sqrt{2}\right)}{\left(\sqrt{2}-1\right)} \frac{1}{\left(1 - \frac{2\delta}{H_{\mathrm{ch}}}\right)} \tag{4.8}$$

For static conditions, an infinitesimal layer of continuous phase is assumed to remain in the wall films ($\delta \xrightarrow{Ca_{\mathrm{c}} \to 0} 0$). The received static theoretical dimensionless gutter radius is applied in the presented model in order to reference the static condition of the interface shape and can be expressed as

$$k^{\mathrm{stat}}_{\mathrm{g,theo}} = \frac{\left(\frac{\delta_{\mathrm{g}}}{H_{\mathrm{ch}}}\right)}{\left(\sqrt{2}-1\right)}. \tag{4.9}$$

Apart from the description of the sectional ellipse line a (Fig. 4.1b) the system of equations of the front is entirely symmetric to that of the droplet back. However, when a flow related pressure gradient compresses the back of the droplet ($k^{\mathrm{dyn}}_{\mathrm{b}} < 1$) and elongates the front ($k^{\mathrm{dyn}}_{\mathrm{f}} > 1$), the expression

for the osculating circles of the sectional ellipse line a needs to be based on different vertices: The co-vertex is used for the frontal cap

$$R_{a,\mathrm{f}}^{\mathrm{dyn}} = \frac{a'^2}{b'}, \tag{4.10}$$

while the main vertex is specifies the cap radius on the backside.

$$R_{a,b}^{\mathrm{dyn}} = \frac{b'^2}{a'} \tag{4.11}$$

Applying the definition of the gutter radius (Eq. 4.7) in the expression for the semi-minor axis of the sectional ellipse b' results from geometrical consideration:

$$\begin{aligned} b' &= \left(\frac{H_{\mathrm{ch}}}{2} - \delta\right)\sqrt{2} - R_{\mathrm{g},i}^{j}\left(\sqrt{2}-1\right) \\ &= \frac{H_{\mathrm{ch}}\sqrt{2}}{2}\left(1 - \frac{2\delta}{H_{\mathrm{ch}}}\right)\left(1 - 2k_{\mathrm{g},i}^{j}\left(1 - \frac{1}{\sqrt{2}}\right)\right). \end{aligned} \tag{4.12}$$

The corresponding semi-major axis a' is calculated using the elliptical description of line 1 (Fig. 4.1b) on the xy-symmetry plane and its semi-major a_1 and -minor b_1 axis. y' denotes the intercept in y-direction of line 1 leading to a' as the according x-axis intercept x':

$$a' = x' = \frac{a_1}{b_1}\sqrt{b_1^2 - y'^2} \tag{4.13}$$

$$a_1 = k_i^j b_1 \tag{4.14}$$

$$b_1 = \left(\frac{W_{\mathrm{ch}}}{2} - \delta\right) = \frac{H_{\mathrm{ch}}}{2}\left(A_{\mathrm{r}} - \frac{2\delta}{H_{\mathrm{ch}}}\right) \tag{4.15}$$

$$
\begin{aligned}
y' &= \left(\frac{W_{\mathrm{ch}}}{2} - \delta\right) - \left(\frac{H_{\mathrm{ch}}}{2} - \delta\right) \\
&= \frac{H_{\mathrm{ch}}}{2}\left(A_{\mathrm{r}} - 1\right)
\end{aligned} \tag{4.16}
$$

For the supporting line b in the proximity of the gutter entrance (Fig. 4.1b) the radius $R^j_{b,i}$ of the osculating circle is derived. The expression is derived for the intersection of line a and b.

$$
R^j_{b,i} = \frac{1}{a''^4 b''^4}\sqrt{\left(a''^4 y^2_{ab} + b''^4 z^2_{ab}\right)} \tag{4.17}
$$

The height z_{ab} on which the intersection is located is estimated from geometric considerations in Fig. 4.1b with

$$
\begin{aligned}
z_{ab} &\approx \left[a'' - R^j_{\mathrm{g},i}\right] + \frac{R^j_{\mathrm{g},i}}{\sqrt{2}} \\
&\approx \frac{H_{\mathrm{ch}}}{2}\left(1 - \frac{2\delta}{H_{\mathrm{ch}}}\right)\left(1 - 2k^j_{\mathrm{g},i}\left(1 - \frac{1}{\sqrt{2}}\right)\right).
\end{aligned} \tag{4.18}
$$

The corresponding intercept on the y-axis is formulated as

$$
y_{ab} = \frac{b''}{a''}\sqrt{a''^2 - z^2_{ab}}, \tag{4.19}
$$

where a'' denotes the semi-major axis of the ellipse at line b in z-direction and b'' represents the according semi-minor axis in y-direction:

$$
a'' = \left(\frac{H_{\mathrm{ch}}}{2} - \delta\right) = \frac{H_{\mathrm{ch}}}{2}\left(1 - \frac{2\delta}{H_{\mathrm{ch}}}\right) \tag{4.20}
$$

$$
b'' = \left(\frac{W_{\mathrm{ch}}}{2} - \delta\right) - y'' = \frac{H_{\mathrm{ch}}}{2}\left(A_{\mathrm{r}} - \frac{2\delta}{H_{\mathrm{ch}}}\right) - y''. \tag{4.21}
$$

The ellipse line 3 at the onset of the top wall film delivers the y-axis intercept y'' for the sectional ellipse line b (Fig. 4.1b) applying the corresponding semi-minor and-major axis a_3 and b_3:

$$y'' = \frac{b_3}{a_3}\sqrt{a_3^2 - x''^2} \tag{4.22}$$

$$a_3 = k_f^j b_3 \tag{4.23}$$

$$\begin{aligned} b_3 &= \left(\frac{W_{\mathrm{ch}}}{2} - \delta\right) - R_{\mathrm{g},i}^j \\ &= \left(\frac{A_{\mathrm{r}} H_{\mathrm{ch}}}{2} - \delta\right) - k_{\mathrm{g},i}^j \left(H_{\mathrm{ch}} - 2\delta\right) \\ &= \frac{H_{\mathrm{ch}}}{2}\left(\left(A_{\mathrm{r}} - \frac{2\delta}{H_{\mathrm{ch}}}\right) - 2k_{\mathrm{g},i}^j\left(1 - \frac{2\delta}{H_{\mathrm{ch}}}\right)\right). \end{aligned} \tag{4.24}$$

The x-position x'' at which the top film ellipse is evaluated is equal to the semi-major axis a_4 of the side film ellipse line 4 (Fig. 4.1b):

$$\begin{aligned} x'' &= a_4 = k_i^j\left(\left(\frac{H_{\mathrm{ch}}}{2} - \delta\right) - R_{\mathrm{g},i}^j\right) \\ &= k_i^j \frac{H_{\mathrm{ch}}}{2}\left(1 - \frac{2\delta}{H_{\mathrm{ch}}}\right)\left(1 - 2k_{\mathrm{g},i}^j\right). \end{aligned} \tag{4.25}$$

For the static case $Ca_{\mathrm{c}} \to 0$, the cap deformation ratio reaches unity $k_{\mathrm{f}}^{\mathrm{stat}} = k_{\mathrm{b}}^{\mathrm{stat}} \to 1$ and the wall film thickness is infinitesimal $\delta \to 0$. The flow related front and back deformation of the droplet caps $k_{\mathrm{f}}^{\mathrm{dyn}}$ and $k_{\mathrm{b}}^{\mathrm{dyn}}$ can be extracted e.g. from experimental images of the Taylor flow. Calculating the capillary number and Reynolds number delivers the wall film thickness δ/H_{ch}. Inserting the summarized conditions and equations (4.7 - 4.25) into (4.6) delivers the final description. As a final step, the dynamic front and back gutter radii $R_{\mathrm{g},i}^{\mathrm{dyn}}$ ($k_{\mathrm{g},i}^{\mathrm{dyn}}$) are calculated using a zero-finding algorithm.

The difference between the front and the back gutter radius results from the different deformation of the front and back caps. The relation of the proposed geometrical approximation summarizes as follows: With rising viscous forces (rising Ca-number) the pressure drop along the droplet increases. The rear cap is compressed while the front cap is elongated with respect to the main flow direction (bullet shape of the droplet). Accordingly, the front gutter radius is larger than the rear gutter radius. The above system of equation delivers the quantitative connection between the cap deformation and the gutter radii. Additionally, the location of the gutter entrances is determined with respect to the cap tips and an entire boundary framework for the droplet shape.

4.3 Geometric boundary framework

The geometric representation of the droplet interface is constructed in a quarter section of the channel volume, making use of the existing flow symmetry. The front and back cap deformation ratios k_i^j are assumed to generally deliver a measure describing the deformation of the entire associated cap region (Eq. 4.3). Thus, these deformation ratios are applied to the lines 1-4 (Fig. 4.1). The dynamic gutter radii $R_{\mathrm{g},i}^{\mathrm{dyn}}$ ($k_{\mathrm{g},i}^{\mathrm{dyn}}$) are positioned at a distance $x_{\mathrm{g},i}^j$ from the tip (coordinates $[0,0,0]$) and tail (coordinates $[-L_{\mathrm{d}},0,0]$) towards the center of the droplet. Geometric considerations and inclusion of Eq. 4.25 deliver:

$$\begin{aligned} \Delta x_{\mathrm{g},i}^j &= k_i^j \left(\frac{W_{\mathrm{ch}}}{2} - \delta \right) + a_4 \\ &= k_i^j \frac{H_{\mathrm{ch}}}{2} \left[\left(A_{\mathrm{r}} - \frac{2\delta}{H_{\mathrm{ch}}} \right) + \left(1 - \frac{2\delta}{H_{\mathrm{ch}}} \right) \left(1 - 2k_{\mathrm{g},i}^j \right) \right]. \end{aligned} \tag{4.26}$$

For droplets shorter than a critical dimensionless length of $\frac{L_{\mathrm{crit}}}{W_{\mathrm{ch}}} \leqslant (x_{\mathrm{g,f}}^j + x_{\mathrm{g,b}}^j)$ the actual location of the gutter radii with respect to the droplet front and back cap-tips would lack physical meaning. In those cases, shorter droplets need to develop bigger gutter radii to accommodate the dispersed phase. The minimal dispersed phase size ($\frac{L_{\mathrm{min}}}{W_{\mathrm{ch}}} \rightarrow 1$) has a gutter radius of approximately

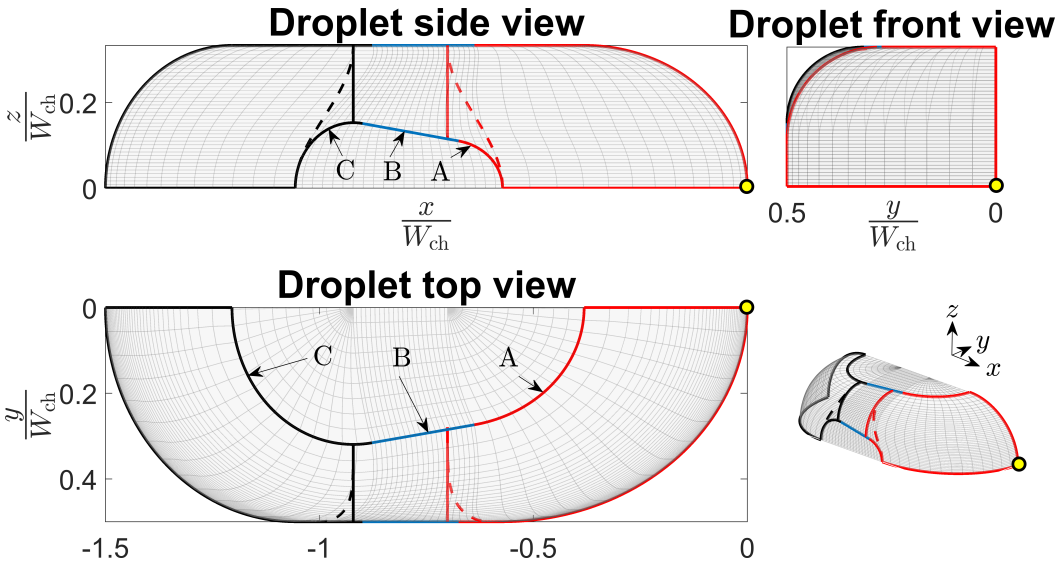

Fig. 4.2: Geometric boundary frame representation of the Taylor flow interface shape model ($A_\mathrm{r} = 1.5; L_\mathrm{d}/W_\mathrm{ch} = 1.5$). The yellow dot represents the interface front tip. The droplet length L_d and the front and back cap deformation ratios k_i are expected to be experimentally determined by e.g. imaging of the xy-symmetry center plane. The lines A-B-C show the outlines of the wall films.

half the channel height ($k_{\mathrm{g},i} \to 0.5$). To preserve the deformation information of the caps, a scale factor c enlarges both gutter radii obtained from the model:

$$c = A_\mathrm{r} \left(\frac{1}{k^j_{\mathrm{g,f}} + k^j_{\mathrm{g,b}}} \right) \left(\frac{k^j_{\mathrm{g,f}} + k^j_{\mathrm{g,b}}}{2} + A_\mathrm{r} - \frac{L}{W_\mathrm{ch}} \right) \tag{4.27}$$

Subtracting the gutter radii $R^j_{\mathrm{g},i}$ from the half of the droplet width $(W_\mathrm{ch}/2 - \delta)$ and height $(H_\mathrm{ch}/2 - \delta)$ yields the respective semi-minor axis b_3 and b_4 of the wall film onsets (pos. 3 & 4, Fig. 4.1).

In order to avoid sharp edges on neighboring interface sections at the side wall films, the x-coordinates of the side film onset (line 4) are joined with the x-coordinate of the gutter radii postulating a z-dependent cosine function (dashed lines, side view, Fig. 4.2).

4.4 Interface construction sequence

The interface construction routine is implemented in a Matlab script. The iterative progression of the calculation begins at the center points of the ellipses at the top wall film. Moving outwards towards the border of the top film (Fig. 4.2: Top view), the routine advances against the positive z-direction towards the xy-center plane of the droplet. At each iteration step, the supporting points of the particular front and back ellipses are computed applying the above explained geometric boundary framework. Subsequently, the front and back ellipses are tangentially connected to form a smooth outline (Fig. 4.2: Top view). Finally, the entire resulting surface quarter is copied, mirrored and rearranged to form a closed interface. The starting point of the construction sequence causes an optical artifact: The outline of the top wall film is visible in the grid structure, while the outline of the sidewall film is not visible (e.g. Fig. 4.3a). Nonetheless, both are present (see Fig. 4.2, lines A-B-C).

4.5 Visualization and application

In order to demonstrate the capability of the Taylor flow interface shape model, four different geometrical settings are chosen as shown in Fig. 4.3: two droplet lengths ($L_\mathrm{d}/W_\mathrm{ch} = 1$ and ≈ 1) for two aspect ratios ($A_\mathrm{r} = 1, 2$). These are representative for Taylor-droplet shapes reported in many applications.

A widely used 1st order estimate for the volume V_d of the Taylor droplet is a confining cuboid of the dimensions $H_\mathrm{ch}\, W_\mathrm{ch}\, L_\mathrm{d}$ [87]. However, a significant amount of continuous phase is accommodated outside the caps and in the gutters [107]. The deviation of this basic cuboid geometry from the here presented approach is depicted in Fig. 4.4 for a channel aspect ratio of $A_\mathrm{r} = 1$ and $Ca_\mathrm{c} = 0.002$.

The confining cuboid approach overestimates the volume of elongated droplets about 15%, while for shorter droplets $\frac{L_\mathrm{d}}{W_\mathrm{ch}} \approx 2$ it overestimates the volume up to 31%. The shortest droplet length is a sphere $\frac{L_\mathrm{d}}{W_\mathrm{ch}} \approx 1$ that is

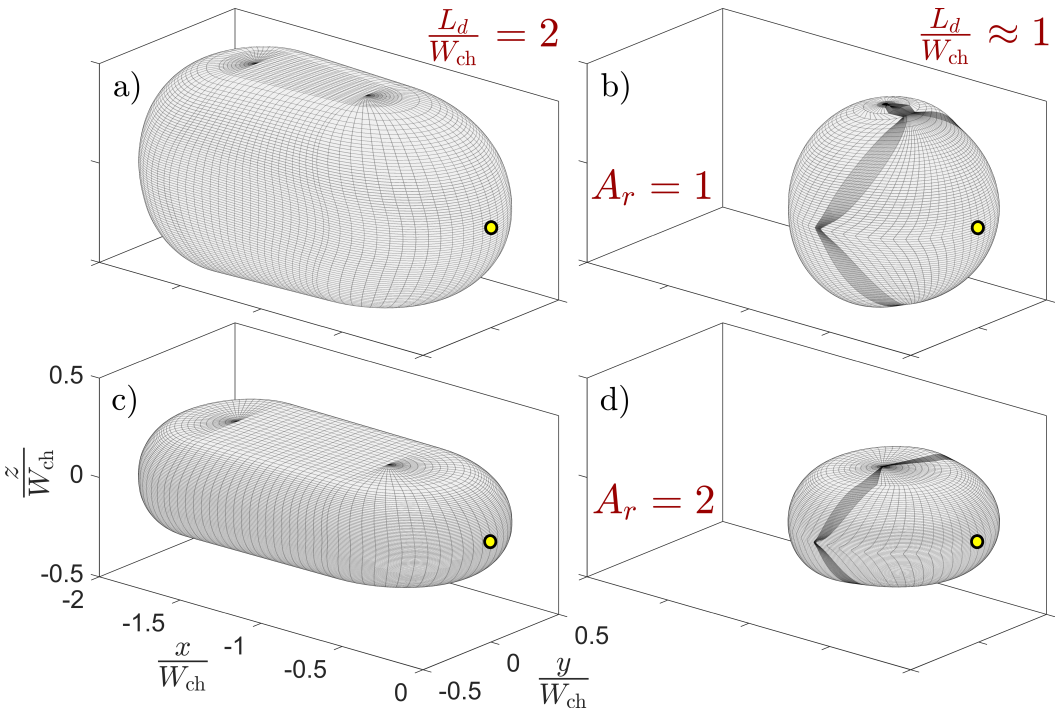

Fig. 4.3: Visualization of commonly used droplet sizes in two different channel geometries: Aspect ratio $A_{\mathrm{r}} = 1$, a) long ($2W_{\mathrm{ch}}$) and b) short ($1W_{\mathrm{ch}}$) droplet. Aspect ratio $A_{\mathrm{r}} = 2$, c) long ($2W_{\mathrm{ch}}$) and d) short ($1W_{\mathrm{ch}}$) droplet. The flow is directed along the positive x-axis and the tip of the interface is marked with a yellow dot. The starting point of the construction sequence causes an optical artifact: The outline of the top wall film is visible in the grid structure, while the outline of the sidewall film is not visible (e.g. Fig. 4.3a). Nonetheless, both are present (see Fig. 4.2, lines A-B-C).

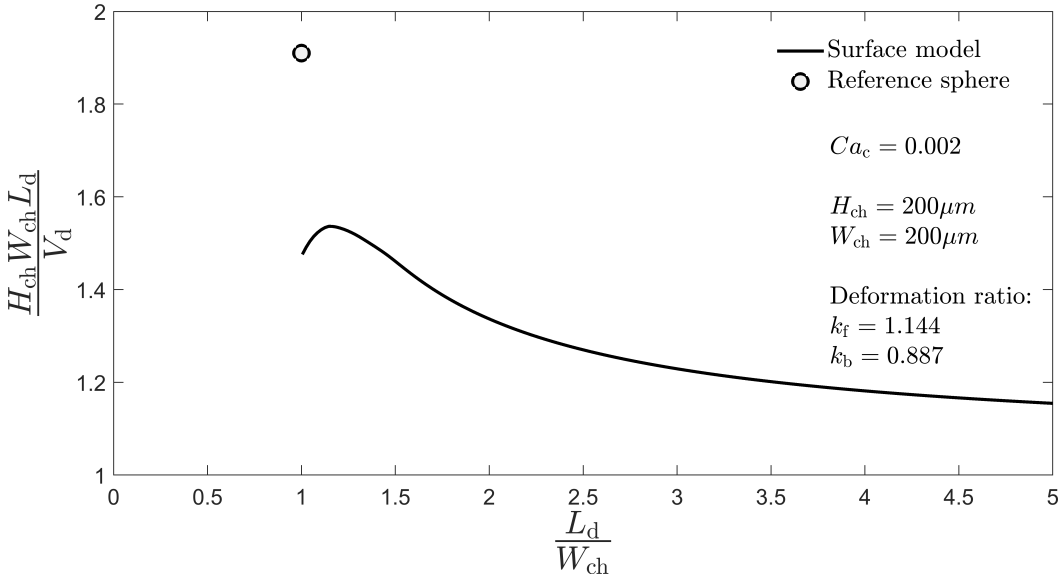

Fig. 4.4: Comparison of the droplet volume V_d with that of the bounding cuboid ($H_\mathrm{ch}W_\mathrm{ch}L_\mathrm{d}$) in dependence of the dimensionless droplet length $\frac{L_\mathrm{d}}{W_\mathrm{ch}}$ including the flow induced deformation at $Ca_\mathrm{c} = 0.002$ at $A_\mathrm{r} = 1$. The basic 1st order confining cuboid approach overestimates the volume of elongated droplets of about 15%. The cuboid model for shorter droplets $\frac{L_\mathrm{d}}{W_\mathrm{ch}} \approx 2$ exposes a volume overestimation of up to 31%. The shortest droplet length is a sphere $\frac{L_\mathrm{d}}{W_\mathrm{ch}} \approx 1$ that is confined in a cuboid of $H_\mathrm{ch}W_\mathrm{ch}^2$, which overestimates the reference sphere by a factor of 1.9. The viscous forces of the flow deform the spherical shape and result in additional disperse phase accommodated in the confining cuboid.

confined in a cuboid of $H_\mathrm{ch}W_\mathrm{ch}^2$, which overestimates the reference sphere by a factor of 1.9 (black dot, Fig. 4.4). The viscous forces of the flow deform the spherical shape and result in additional droplet volume V_d accommodated in the confining cuboid.

The interface shape model can be applied directly, when the cap deformation ratios k_i and the droplet length are experimentally available from images and the channel geometry is known. However, given a relation between the cap deformation ratio and the capillary number Ca_c, an entire scope of Taylor droplet shapes is at hand with a relatively small computational effort. Sauzade and Cubaud [101] propose a capillary number dependent quotient of the front and back deformation ratio $k_\mathrm{b}^\mathrm{dyn}/k_\mathrm{f}^\mathrm{dyn}$ to quantify the overall deformation of their droplets. However, to calculate the individual front and back gutter radii, a discrimination between the front cap and the back cap deformation is necessary, and therefore their relation can't be applied.

A manually fitted impression of the deformation ratio in dependence of the capillary number is depicted in in Fig. 4.5. The underlying data consists of measurements of Helmers et al. [42] and their interface deformation estimation derived from the simulation of Taha and Cui [109] in combination with the particle image data presented later in this study. The static cap shape of the interface is assumed to be circular (grey line). When exposed to a viscous flow ($Ca_c > 0$), the back cap geometry is compressed ($k_b < 1$, black points), while the front cap is elongated ($k_f > 1$, gray points). Based on this rough assessment, the corresponding dimensionless gutter radii of the deformed caps are calculated with the above presented model and referenced with the theoretical dimensionless gutter radius (blue line, Fig. 4.5) to enable a comparison to the theoretical gutter radius, which is implicitly delivered by the side wall- and diagonal gutter film thickness δ_g of Han and Shikazono [37] (Eq. 4.8).

For $Ca_c < 0.004$ the theoretical gutter radius is higher than the mean dynamic gutter radius received from this study. The maximum deviation is about 1%. Regarding flows with higher capillary numbers, the theoretical value decreases due to the significant thickening of the gutter film. The gutter radii of the model actually increase further. Based on this comparison the validity range of the model is estimated to span from static flow conditions ($Ca_c = 0$) to a maximum of $Ca_c = 0.01$. Obviously, this interrelation needs to be investigated more thoroughly with a considerably increased number of data points. Additionally, the inertia effect needs to be investigated, to systematically clarify the role of the Reynolds number on the deformation of the Taylor droplet shapes.

4.6 Results and discussion

In this section the position and shape of the interface between the model and the measurements is compared. The quality of the model is tested with respect to the following geometrical and material parameters: the channel aspect ratio, the dimensionless droplet length, and the material system. At first, the flow related dilation of the PDMS-channel geometry is addressed. Secondly, a deviation map gives an qualitative and quantitative

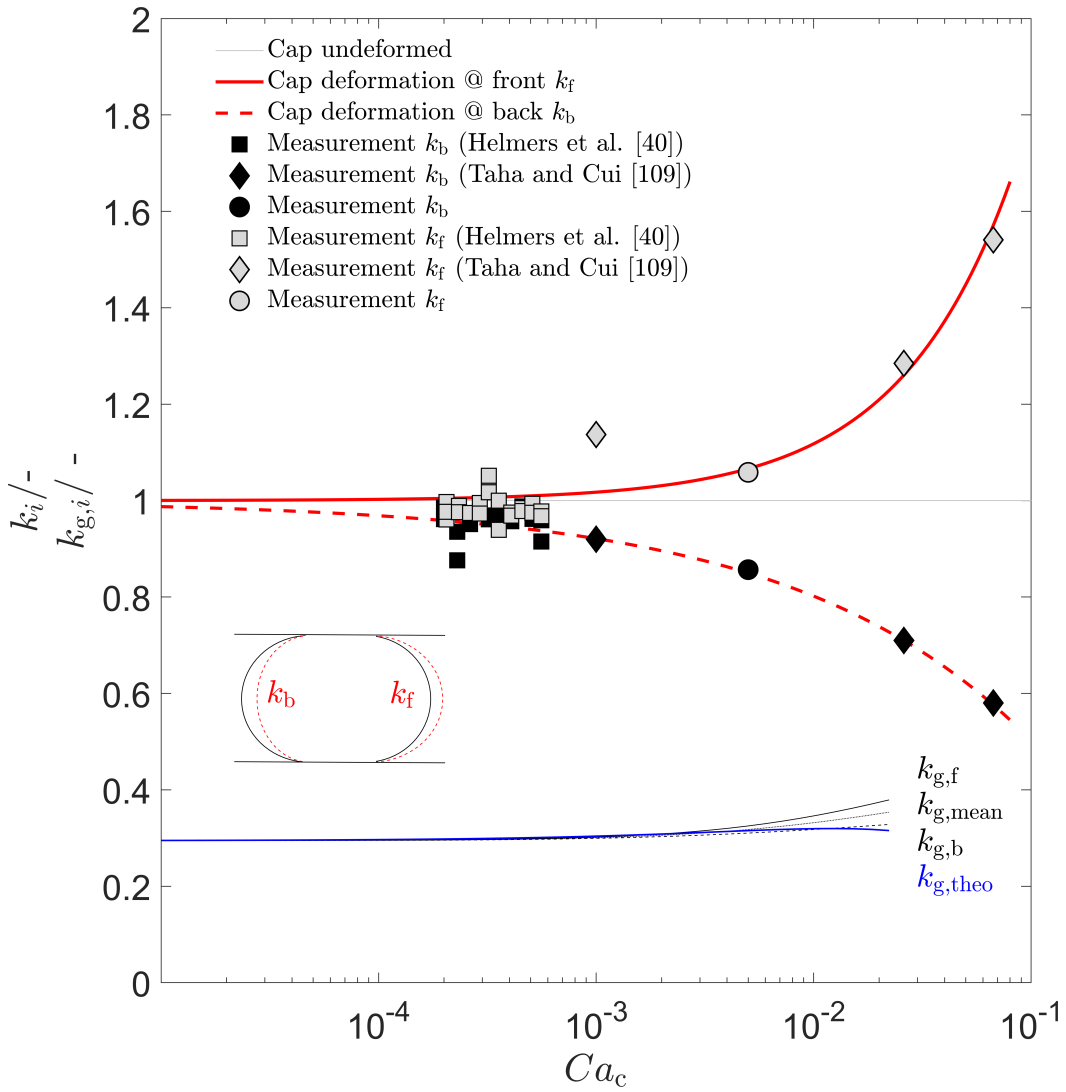

Fig. 4.5: Deformation ratios k_i of the droplet caps in dependence of the capillary number: Measurements and manual estimation of the data trend. Resulting gutter radii in comparison to a literature based theoretical approach. Given the manual estimation of the cap deformation ratios the gutter radii appear to be in good agreement.

impression based on the exemplary droplet already addressed in Fig. 3.5. Subsequently, a more detailed plane-wise shape comparison between the Taylor droplet shape model and the measurements is conducted. Finally, an overall shape assessment with the statistical droplet measurements is given and discussed.

4.6.1 Deformation of the PDMS-Channel

The initial positioning of the measurement plane in z-direction is referenced by focusing on the channel top and bottom wall and measuring the according objective position. After establishing a continuous Taylor droplet flow the pressure drop across the disperse phase and film deforms the ductile PDMS-channel up to 5% in z-direction. Hence, the referenced top and bottom walls of the channel slightly expand their distance.

A compensation of the channel deformation is performed by adjusting the relevant model channel height to the dimensions of the deformed experimental setup. The following presented data sets are all treated with this adaption procedure.

4.6.2 Shape deviation between model and measurement

The accuracy of the suggested Taylor flow interface shape model is at first visualized mapping the deviation $\frac{r}{W_{\mathrm{ch}}}$ from the experimental data onto the theoretical surface (Fig. 4.6a). The color coding uses dark red to indicate a positive discrepancy in case the measurement overshoots the model with more than $+5\%$. Dark blue displays negative differences of -5% and more. The range between $\pm 2.5\%$ is purposely marked gray to emphasize the model surface fraction that does not deviate significantly from the measurement. Thus, most of the model interface does achieve non-significant deviations. Due to the location asymmetry of the significant shape deviations with respect to the flow axes, the discrepancies are attributed to measurement artifacts rather than to the flow conditions. The top of the 3D-deviation map is not closed, since at this position no measurement data is available. Instead, the grid structure of the model is depicted.

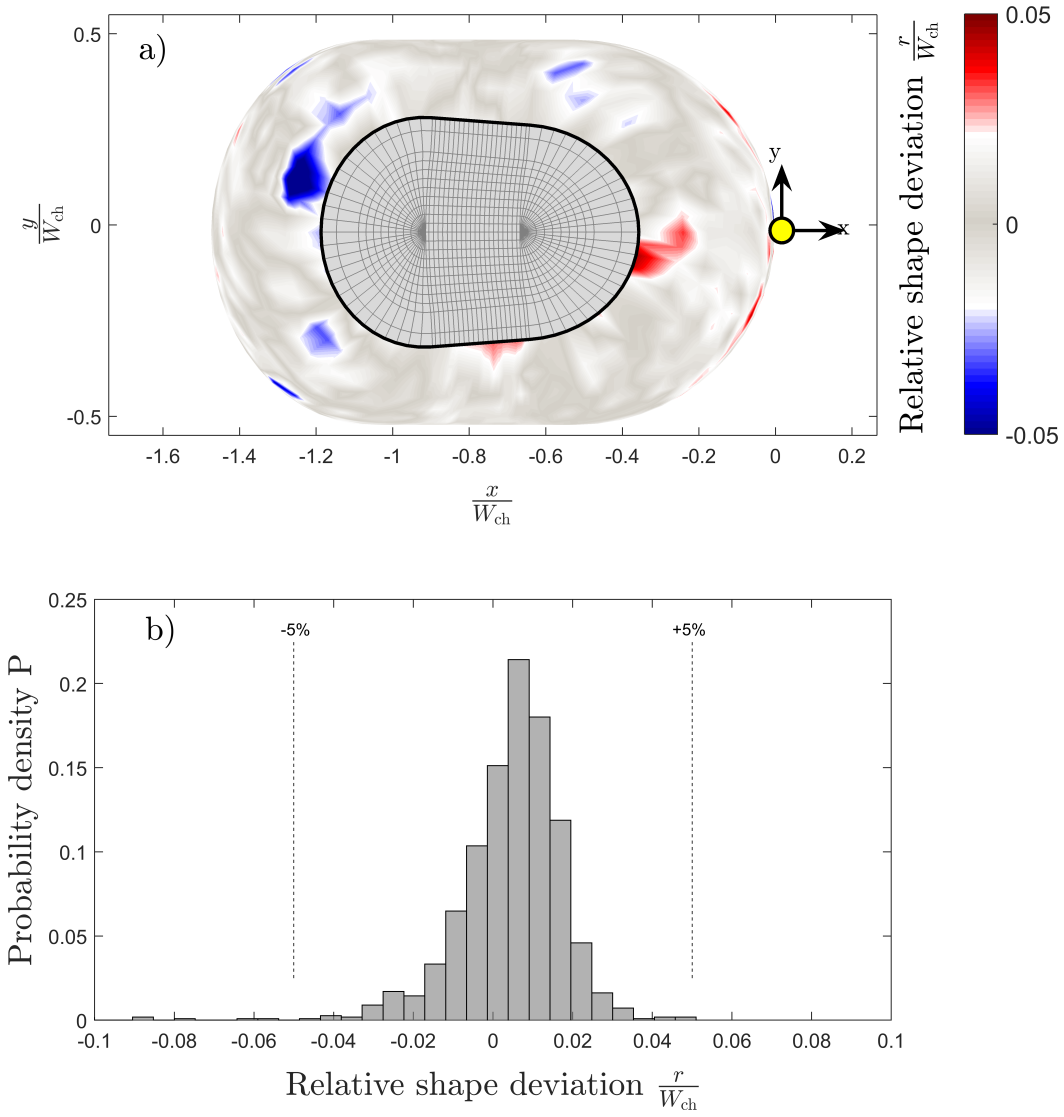

Fig. 4.6: a) Surface map (top view) of the relative deviation location. Dark red and blue colors indicate a deviation beyond $\pm 5\%$. Gray color specifies value between $\pm 2.5\%$. b) Probability density distribution of the relative shape deviation. A slight skew towards positive values is present with a minor positive shift.

The probability density distribution P of the relative shape deviation $\frac{r}{W_{\mathrm{ch}}}$ is computed and shown in Fig. 4.6b). Almost the entire distribution is located well between $\pm 5\%$. The location of the peak deviation in the graph indicates a minor skew towards a positive shape deviation (+7.5‰): The model underestimates the measured interface position, which corresponds to a mild underestimation of the approximated droplet volume. The modeled droplet is slightly too small.

A measurement plane wise itemization assesses the relative deviation independent of its direction, as a function of the droplet length, aspect ratio and material system (Fig. 4.7). At first, longer droplets $\frac{L_{\mathrm{d}}}{W_{\mathrm{ch}}} > 1$ are considered (Fig. 4.7a). The mean shape deviation of the droplets inside the investigated aspect ratio $A_{\mathrm{r}} = 1$ channel remains below an relative error $\frac{r}{W_{\mathrm{ch}}}$ of 2.5% for all measurement planes. Taking the standard deviation into account, the maximum relative error is 3.6% at a channel height of $42.8\,\mu\mathrm{m}$. A clear influence of the material parameter is not observable.

The droplet shape model of a Taylor flow inside a channel of aspect ratio $A_{\mathrm{r}} = 2$ exhibits a growing deviation with increasing channel height. The mean discrepancies between measurement and model stay below 5% but roughly double compared to the corresponding channel of aspect ratio $A_{\mathrm{r}} = 1$.

The mean relative shape deviation short Taylor droplets ($\frac{L_{\mathrm{d}}}{W_{\mathrm{ch}}} \approx 1$) stays below 2.5% (Fig. 4.7b). The deviation even decreases until the gutter height is reached at $H_{\mathrm{ch}} \approx 25\,\mu\mathrm{m}$.

Approaching the top wall film of the interface (Fig. 4.7a), the mean deviation rises up to 3.5% for water/DMSO. Taking the standard deviation into account at this height level, the maximum deviation of 5.2% is reached. No clear difference between the droplet materials was noticed.

Continuing from the section-wise model assessment, an overall accuracy of the modeled interface with respect to the measurement is given in Fig. 4.8. Measurement cases A to E reflect the droplet material system variation along with the geometrical variation of the aspect ratio and the droplet length. The mean relative deviation is provided as well as the respective standard deviation to indicate the accuracy of the proposed Taylor flow interface shape model.

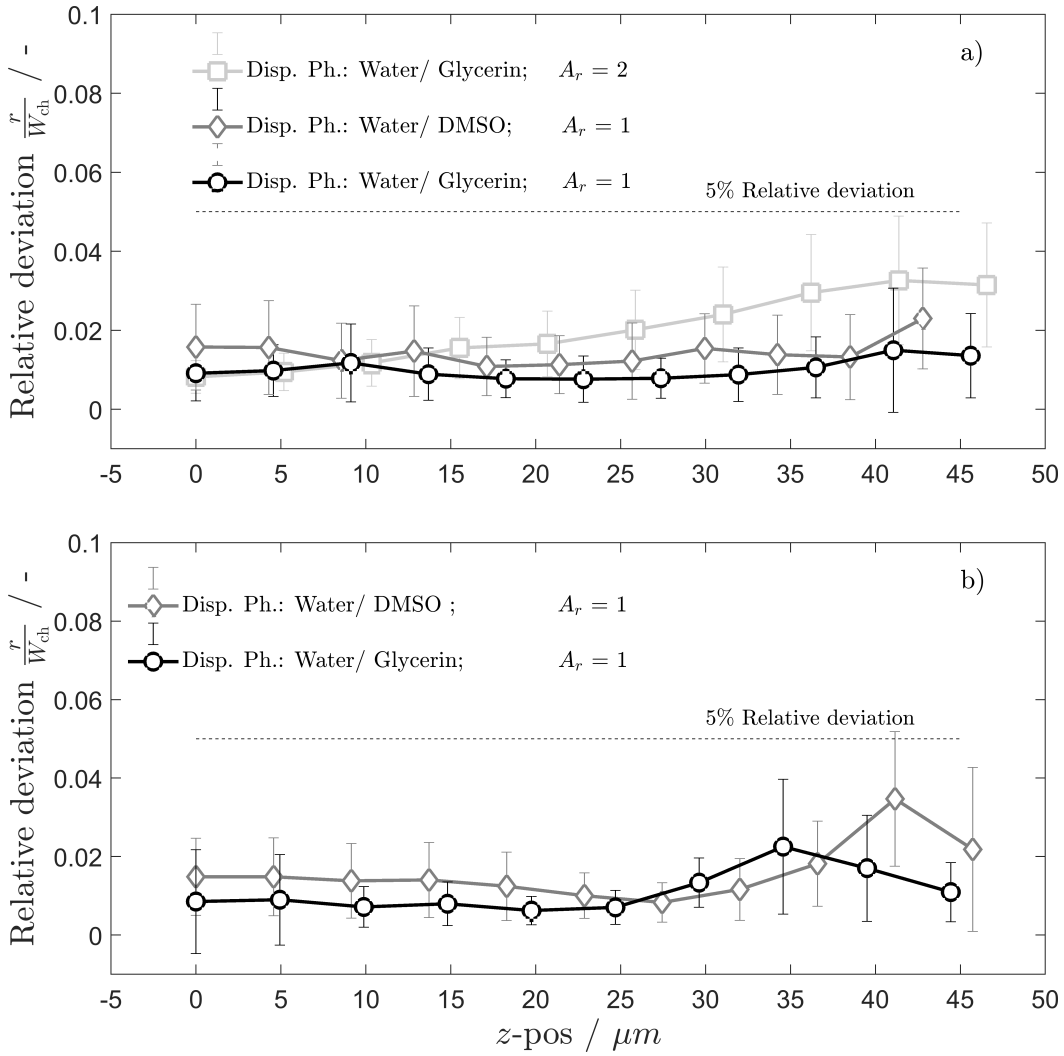

Fig. 4.7: Comparison of the relative in-plane shape deviation between model surface and average particle images of elongated a) ($\frac{L_d}{W_{ch}} = 1.31 \cdots 1.66$) and short droplets b) ($\frac{L_d}{W_{ch}} \approx 1$) for different height positions z as shown in Fig. 3.5). The relative deviation of the long droplets is well below 5% with maximum values in the z = 35 to 45 μm range corresponding to regions with larger deviations in Fig. 4.6). The example for $A_r = 2$ shows a deviation twice as big at the slanting top part of the droplet. The same trend holds for the short droplets. Despite the increased relative error in the proximity of the curved droplet top, the proposed interface shape model fits well for both investigated material systems.

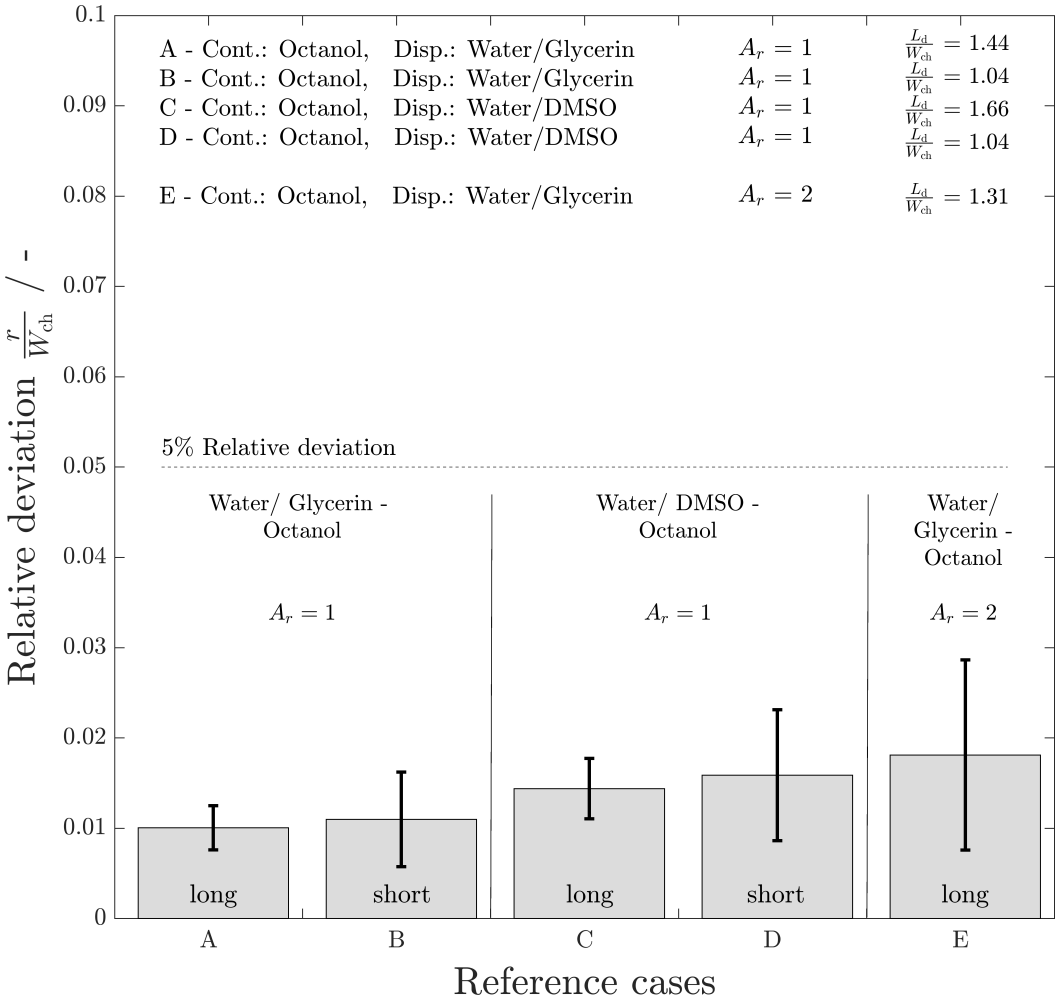

Fig. 4.8: Comparison of the overall shape deviation between model interface and the averaged particle images. The mean deviation for all shapes and materials stays well below the 5% mark.

All mean relative shape deviations are quantified to be below 5% (dashed reference line, Fig. 4.8). The model comparison exhibits the maximum relative shape deviation in case E: the long water/ glycerin droplet measured in a channel of aspect ratio $A_\mathrm{r} = 2$.

The material variation indicates a decreased accuracy for the water-DMSO/ octanol system. The interfacial tension ($\sigma = 2.26\,\mathrm{mN\,m}$) as well as the viscosity ratio $\frac{\eta_\mathrm{d}}{\eta_\mathrm{c}} = 0.43$ are smaller than that of the water-glycerin/ octanol system ($\sigma = 5.89\,\mathrm{mN\,m}$, $\frac{\eta_\mathrm{d}}{\eta_\mathrm{c}} = 2.62$). The capillary number of the continuous phase is held constant at $Ca_\mathrm{c} = 0.005$ to preserve a comparable force balance between the outer viscous forces and the interface tension forces. Thus, the viscosity ratio indicating the momentum transfer into the droplet is likely to be the reason for the increase of the material related relative shape deviation. As Balestra et al. [11] and Rao and Wong [97] show, the momentum coupling has an influence on the relative velocity and the droplet shape. In addition the model appears to represent elongated droplets better than the minimal sizes around the dimensionless droplet length of 1. This effect is anticipated, since the deformation leads to an increased accommodation of disperse phase compared to a non-deformed reference sphere (Fig. 4.4).

The mean overall deviation for all cases is found to be below 2%. When taking the standard deviation into account the relative deviation stays below 3%. Hence, the proposed interface shape model for Taylor flow at low capillary numbers does represent real flow conditions with good accuracy.

4.7 Conclusion

In order to enable a model based guidance for the 3D flow field reconstruction for multiplane μPIV-measurements of Taylor flows in rectangular micro channels, an analytic interface shape approximation for low capillary numbers is proposed. Based on the flow dependent droplet dimensions in the droplet symmetry plane an elliptical shape deformation is assumed. Given the flow dependent elliptical front and back cap deformation ratio, the droplet length and the channel aspect ratio, the front and back gutter radii can now be determined. The interface shape construction sequence uses a framework of geometric boundary conditions to calculate the 3D-distribution of interface

nodes. The proposed model can be applied for rectangular channels of varying aspect ratio $A_\mathrm{r} = [1...2]$ (and possibly beyond) and dimensionless Taylor droplet length $\frac{L_\mathrm{d}}{W_\mathrm{ch}} \gtrsim 1$.

The capillary numbers covered by the analytical approximation are set in a range that is suitable not only for applications but also for theoretical work on microscopic Taylor flow. In terms of Reynolds numbers, the approximation is restricted to flows dominated by viscous forces, since the modeled deformation at the back of the droplet begins to deviate beyond the onset of inertia forces [64]. To the best of my knowledge, this model is the first work, that delivers an approach to analytically asses the deformed shape of moving Taylor droplet and the size of the gutter radii.

Verifying the performance of the model, an experimental investigation of continuous Taylor flows is conducted. An optical scanning procedure combined with a microscope objective of small depth of focus records images of tracer particles, which are immersed in Taylor droplets. An image processing procedure is developed that creates average particle image slices of a representative mean Taylor droplet. Those scans provide accurate information about the mean interface position of the flow.

Varying the geometry in terms of aspect ratio as well as in terms of dimensionless droplet length and the material system of the droplet, results in a mean overall deviation of less than 2% with respect to the channel width. When comparing the interface shape model with the particle image data of a 3D-scan, the proposed analytic model is found to represent the low capillary number Taylor droplets accurately.

5

Flow field of a viscous Taylor droplet

Once there were some particles
They flew towards tough obstacles
Following tightly the stream,
with rollercoaster screams
Dreading to find their team,
shot at with laser beams
A particle's life 's no popsicle

This chapter presents a μPIV measurement of the 3D2C velocity distribution of Taylor droplets moving in a square horizontal microchannel at Ca_c = 0.005 and Re_c = 0.051. The third velocity component is reconstructed and an accuracy assessment of the reconstruction is presented based on a volume flow balance of the 3D3C velocity field. The velocity field allows to investigate the 3D flow features such as stagnation regions and the shear rate distribution. The maximum shear rate is located at the entrances and exits of the wall films and at the corner flow (gutter) bypassing the Taylor droplet. The regions of high strain correspond to the cap positions of the Taylor droplets. An experimental data set allows visualization of the streamlines of the velocity distribution on the interface of a Taylor droplet and to directly relate it to the main and secondary vortices of the droplet phase velocity field. The measurement data is provided as digital resource for the validation of numerical simulation or further assessment.

The μPIV-measurement of a 3D flow field relative to the interface of Taylor droplets in motion is evaluated. The 3D velocity field on selected symmetry planes is detailed to introduce comparability to other studies and to visualize the hydrodynamic features. For this purpose, the vector component matrices $u(x, y, z)$, $v(x, y, z)$ and $w(x, y, z)$ are referred to as U, V and W respectively. Secondly, the shear rate distribution of the flow is analyzed to indicate regions of maximum strain. Finally, the application of the λ_2-criterion allows the visualization of the position of the wall-driven main vortices as well as a much less prominent compensating secondary vortex structures inside and outside the Taylor droplets.

If not stated otherwise, the velocity information is presented in a moving frame of reference relative to the droplet velocity u_d. The corresponding streamline representations of the flow are given either in symmetry planes or at locations, where the 2D reference section is not expected to exhibit velocities normal to the section (i.e. the droplet interface).

All representations of Taylor droplet interfaces in the following apply the analytical interface approximation of Mießner et al. [82] (Chap. 4). In the following, when the outcome of this work is described and discussed, it is referred to the results of a single Taylor droplet - despite the large number of statistically incorporated Taylor droplets.

5.1 Overview

A good comprehension of the three dimensional (3D) velocity distribution and its derived quantities, e.g. the shear rate magnitude and distribution, is important for optimal process design. The interaction of advection and diffusion influences the efficiency of multiphase processes, while the resilience of educt or product against shear forces limits the applicable velocity gradients [72].

For low capillary numbers $Ca_\mathrm{c} = \frac{u_{0,\mathrm{tot}}\eta_\mathrm{c}}{\sigma}$, the flow inside and around Taylor droplets is dominated by surface tension forces. Avoiding high shear forces necessitates reduced velocity gradients in small channel dimensions. Thus,

the viscous forces dominate the inertia forces $Re_c = \frac{\rho_c u_{0,tot} H_{ch}}{\eta_c} \leqslant 1$. Buoyancy forces are negligible, since the Bond number $Bo = \frac{\Delta\rho g H_{ch}^2}{\sigma} \ll 1$.

A number of numerical studies are published to clarify the influence of the 3D velocity distribution of pressure driven Taylor flows in rectangular microchannels on the involved processes. Hazel and Heil [38] investigated the propagation of a semi-infinite bubble at $0.001 \leqslant Ca_c \leqslant 10$ and $Re_c \ll 1$. Taha and Cui [109] performed CFD modeling of the rising slug flow inside square capillaries ($0.001 \leqslant Ca_c \leqslant 3, Re_c \ll 1$). Raimondi et al. [96] simulated the mass transfer in square microchannels for liquid–liquid slug flow ($0.001 \leqslant Ca_c \leqslant 10$ and $Re_c \ll 1$) and Guido and Preziosi [34] studied the droplet deformation of Taylor flows ($0.001 \leqslant Ca_c \leqslant 1, Re_c \leqslant 50$). Falconi et al. [28] presented an experimental study for vertical pressure driven Taylor flow in rectangular minichanels ($Ca_c = 0.1, Re_c = 7$). Bordbar et al. [14] reviewed the slug flow in microchannels with respect to numerical simulation and applications. Kumari et al. [63] published a study on the flow field and heat transfer in slug flow in microchannels with respect to the influence of the bubble volume. Recently, an analytical solution of the Taylor flow in an elongated ellipsoid droplet in the frame of 2D Stokes equations is published by Makeev et al. [77]. Their solution delivers a benchmark to evaluate numerical algorithms that aim to calculate the flow in and around Taylor droplets. The work clearly links the driving velocity distribution on the droplet interface to the circulation of the flow inside: A single vortex develops in 'bypass'-mode, and a set of three vortices result from the 'slug flow'-mode.

On the other hand, detailed measurements of the velocity field in and around microscopic Taylor droplets in rectangular microchannels are reported by Kinoshita et al. [57]. They used a high-speed confocal scanning procedure that enables multiple measurement planes with 2D velocity information. An integration of the continuity equation results the out of plane component. The scanning process of the high-speed confocal scanner with Nipkow disk allows measurements at the following approximated dimensionless numbers: Ca_c = 0.0015, Re_c = 0.00025, A_r = 1.72, MD* = 0.032. Herein, A_r denotes the aspect ratio relating the channel width to its height, while MD* = $\frac{MD}{H_{ch}}$ refers to the measurement depth MD of a single optical slice of the experimental setup divided by the channel height H_{ch}. The same research group

extended their technique and report a simultaneous measurement of a Taylor droplet including its surrounding [91]. An approach to distinguish between tracer particles of different fluorescent color enabled them to discriminate between the phases. The measured Taylor flow features dimensionless numbers, which are comparable to those of this study (Ca_c = 0.003, Re_c = 0.001, A_r = 2.44, MD* = 0.084). Mohammadi and Sharp [85] summarized the experimental methods to access the velocity distribution of Taylor flows. Meyer et al. [80] investigate vertically rising Taylor bubbles in a rectangular mini channel. They measure the velocity field of the continuous phase in the slugs and in the film to support a numerical simulation that provides the entire flow. (Ca_c = 0.1, Re_c = 8, A_r = 1, MD* = 0.015). Khodaparast et al. [55] develop a measurement system (micro particle shadow velocimetry - μPSV) to investigate Taylor flow in circular microchannels in detail [56]. The dimensionless parameters are: Ca_c = 0.0003 - 0.09, Re_c = 0.1-10, MD* = 0.071. The measurements of Ma et al. [74] reveal a viscosity ratio dependent change of flow topology inside their droplets that move in rectangular microchannels. They base their findings on the flow field measurements of two focal plane positions (Ca_c = 0.001-0.1, Re_c = 0.1-10, A_r = 1.33, MD* = 0.099). Liu et al. [72] provide a μPIV investigation of the internal flow transitions inside droplets traveling in a rectangular microchannel. Their measurements sample the 3D velocity field solely in the symmetry plane (Bo = 0.0043, Ca_c = 0.005-0.26, Re_c = 0.1-10, A_r = 1.5, MD* = 0.090).

In this chapter, the inherent physics of a Taylor flow are experimentally captured at low Ca_c and Re_c to generate benchmark data to support parametric CFD-studies. The hydrodynamic features of Taylor droplets are investigated in a horizontal square microchannel (Ca_c = 0.005, Re_c = 0.051, $A_r \approx 1$, MD* = 0.056). Based on a multiplane μPIV measurement, the 3D2C velocity field is experimentally measured inside and outside of Taylor droplets. The full 3D3C velocity field is reconstructed (Sec. 3.5.1) using the continuity equation. The stagnation regions of the flow relative to the droplet motion are presented and the normalized shear rate distribution is deduced (Sec. 2.4.2) and shown. This delivers information on the location with maximal strain. The position is of interest for handling delicate products or sensitive educts. This novel approach yields an experimental data set that allows the visualization of the streamlines of the velocity distribution on the interface of a Taylor droplet and to directly relate it to the main and secondary vortices

of the velocity field. The measurement data is provided as digital resource for the validation of numerical simulation or further assessment.

5.2 2D2C Velocity field at the center plane

At first, the discussion of the normalized relative 2D2C field at the central symmetry plane of the Taylor droplet (Fig. 5.1) asses the quality of the ensemble correlated multiplane μPIV measurement. The droplets translate from left to right with a mean velocity of $u_\mathrm{d} = 4.2\,\mathrm{mm\,s^{-1}}$. The droplet interface is indicated with the analytical shape approximation.

Fig. 5.1 a) depicts the vector field of the relative flow at the x-y symmetry plane. Only every 4th vector in longitudinal direction is plotted to maintain the clarity of the graph. The wall-driven main vortices are already recognizable in the vector plot.

In Fig. 5.1 b) the corresponding streamline representation of the flow is given in combination with a color coding of the normalized stream-wise relative velocity. The main vortices are evident inside and outside of the droplet. The maximum stream-wise absolute velocity at the center of the droplet's main vortex is $1.72\,u_\mathrm{d}$. Also, the secondary vortex structures inside the front and the back cap of the droplet are captured clearly. The rear secondary vortex has roughly half the size of the secondary vortex in the front cap. The stagnation points at the cap tips are prominent.

The color coding in Fig. 5.1 c) shows the measured transverse velocity of the Taylor flow. The reference axis of the flow direction is changed to a radial representation $r = \sqrt{x^2 + y^2}$. The flow in radial direction away from the x-axis is positive (red), while flow towards the center of the micro channel is negative (blue). The maximum radial velocities are a factor of about 3.5 times smaller than the droplet velocity u_d. Inside the secondary vortices at the front and back of the droplet the magnitude of transverse velocities are a factor of 10 smaller than the droplet velocity u_d. A vector addition of the relative flow field inside the secondary vortices shows that the local velocity magnitude decreases below $0.005\,u_\mathrm{d}$. Despite the large dynamic range of

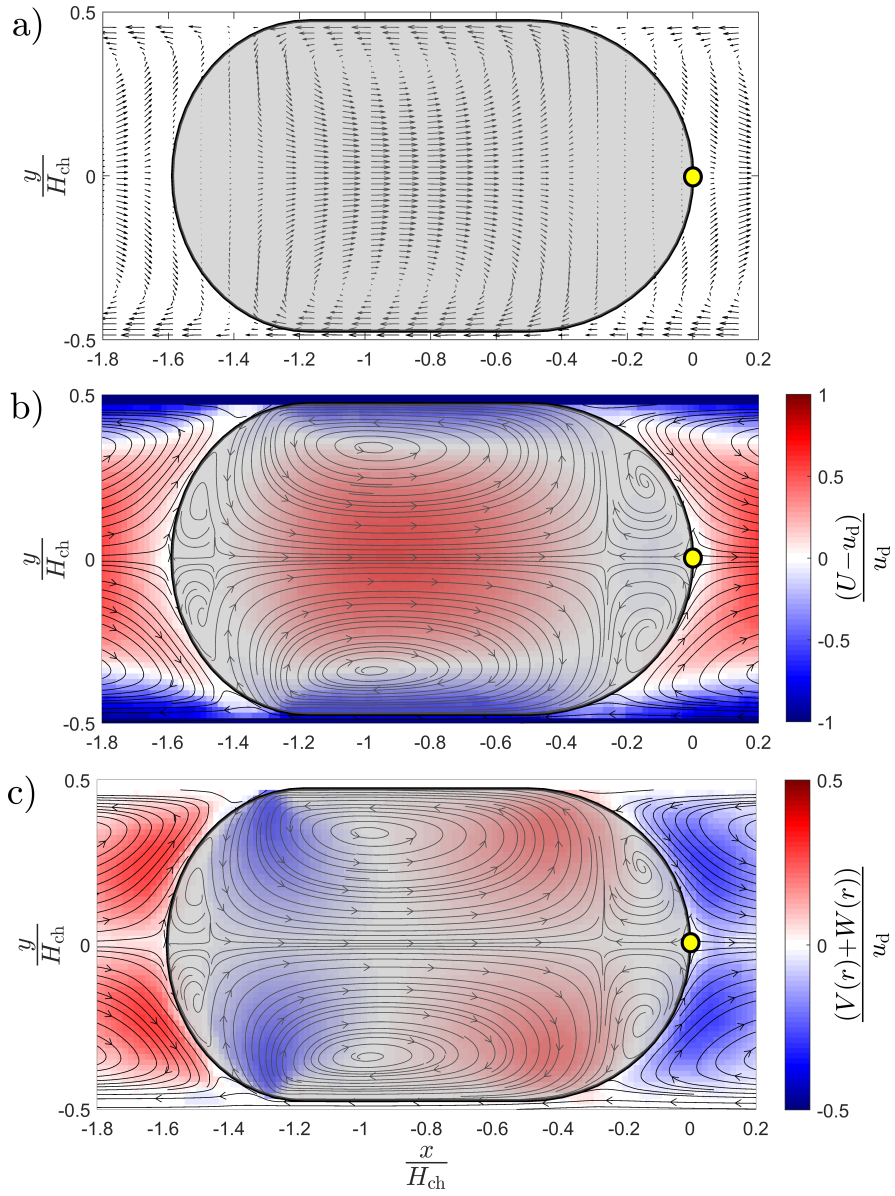

Fig. 5.1: Exemplary ensemble correlated μPIV measurement of the normalized relative velocities inside and outside of a Taylor droplet at the x-y center plane of a square microchannel. The droplet translates from left to right. The yellow dot shows the downstream pointing droplet tip at the origin coordinate system. The black contour line represents the interface position [82] (Chap. 4). The velocity information is depicted in a moving frame of reference. a) 2D2C vector plot of the measurement showing the flow field relative to the droplet movement ($u_d = 4.2\,\mathrm{mm\,s^{-1}}$). For clarity 3 out of 4 vectors in x-direction are omitted. b) Associated streamline plot of the relative flow field with the normalized stream-wise relative velocity being color coded. c) Associated streamline plot of the relative flow field with transverse velocities being color coded. The color coding uses the radius $r = \sqrt{x^2 + y^2}$ as reference. Red represents flow away from the centerline (x-axis) in positive radial direction, while blue color indicates flow against the radial direction towards the centerline. The entire 3D2C data set is given in the supplementary material of this article, along with a plane-wise representation of the measured data

the measurement, the delicate flow structures of the secondary vortices are clearly present in the streamline plot.

5.3 3D3C Velocity distribution

The streamlines on the Cartesian symmetry planes of the droplet allow to compare the quality of the measured velocity distribution ($x-y$ center plane: U, V) to the reconstructed flow distribution ($x-z$ center plane: U, W). The color coded velocities of the flow relative to the interface are depicted in Fig. 5.2. Negative values indicate velocities directed against the chosen reference axis while positive values point into the positive direction. In addition, a streamline representation is given for each data slice based on the respective in-plane components. The droplets translate from left to right.

The stream-wise velocity components are emphasized in Fig. 5.2 a), thus solely measured information is color coded. Despite the difference in spatial resolution between data in the x-y plane ($\Delta x = \Delta y = 1.8\,\mu\mathrm{m}$) and the resolution in z-direction ($\Delta z = 5.4\,\mu\mathrm{m}$) the symmetry of the measurement with respect to the x-axis is obvious. Approaching the droplet rear cap from the tailing slug, the fluid at the channel centerline decelerates in the proximity of the stagnation point. Through the entire rear secondary vortex, the liquid moves slowly with almost the x-velocity of the interface u_d. Further along the x-axis the fluid accelerates, when it enters the wall-driven main vortex and decelerates towards the frontal secondary structure. Beyond the frontal stagnation point the outer fluid accelerates again into the wall-driven main recirculation. In the proximity of the wall, proceeding from the droplet front to its back cap, the fluid decelerates at the on- and off-set of the wall film.

Based on the reconstructed third velocity component W in the z-direction (explained in Sec. 3.5.1) and the measured transverse velocity V, The normalized radial transverse velocity is shown $U_r(r, \theta, x)$ in Fig. 5.2 b). The color coding labels velocities blue when pointing towards and red when pointing away from the x-axis (channel center). The reconstruction of $W = U_r$ in the x-z plane with $y = 0$, where $V(y = 0) = 0$, is in good agreement with the measured transverse velocities $V = U_r$ in the x-y plane

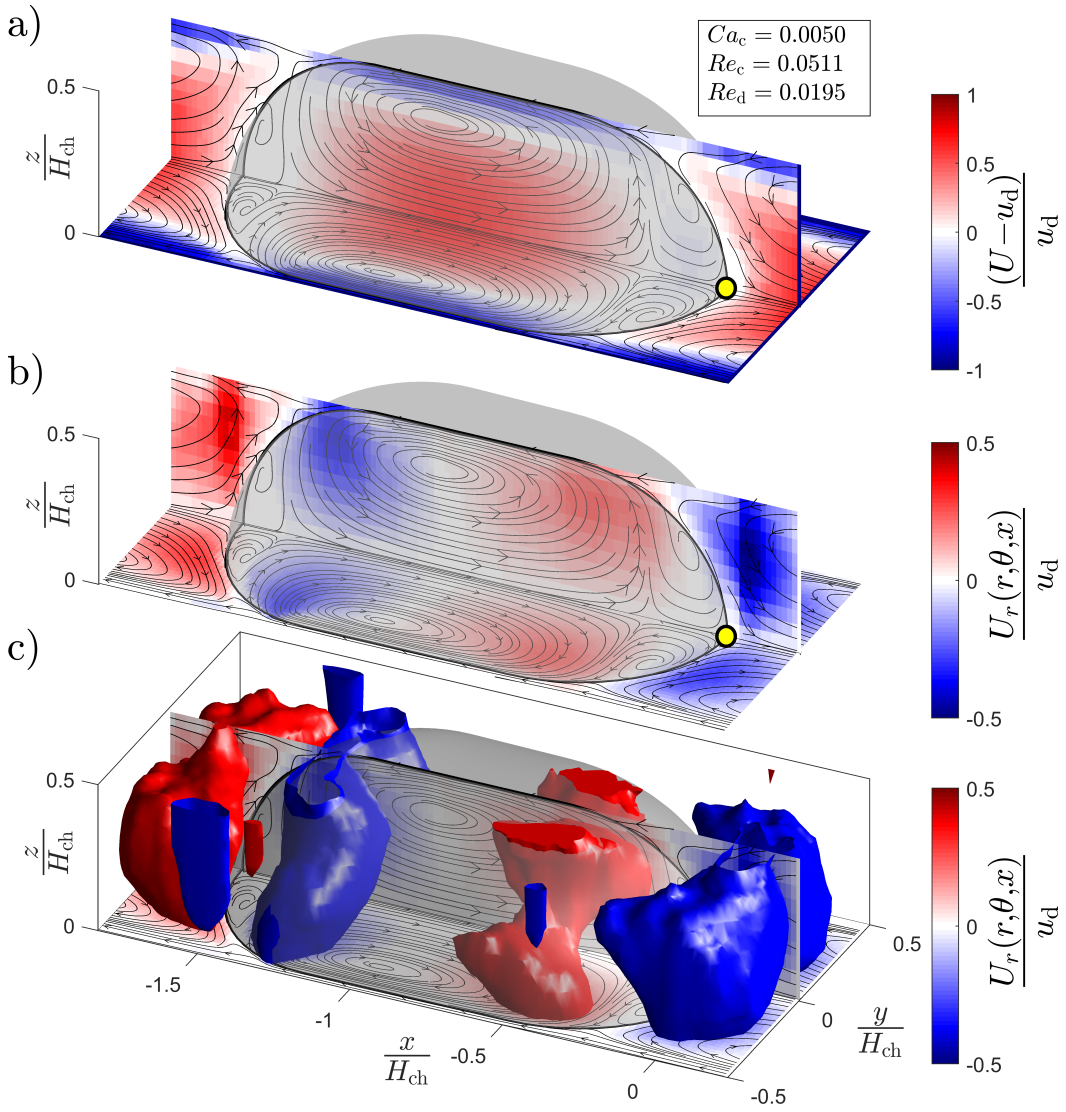

Fig. 5.2: Measured (U, V) and reconstructed W velocity data of the normalized relative flow field in and around Taylor droplets. A streamline representation is given for each data slice based on the respective in-plane components. The droplets translate from left to right. The yellow dot shows the downstream pointing droplet tip at the origin coordinate system. The velocity information is depicted in a moving frame of reference. a) The measured stream-wise relative velocity component is color coded. The streamline representation of the flow field reveals symmetric features of the measurement in the x-y plane in comparison to the reconstruction in the x-z plane. b) The radial transverse velocity component $U_r(r, \theta, x)$ is color coded: blue pointing towards and red away from the x-axis (channel center). c) Isosurfaces are added to b) ($\frac{U_r}{u_d} = 0.175$) to visualize the transverse velocities.

with $z = 0$, where $W(z = 0) = 0$. Also, the amplitude of both positive and negative transverse velocities inside the droplet are similar. However, the velocity development from the stagnation points towards the upper channel wall shows that the reconstruction overestimates the z-component.

In general, the flow features along the z-axis are less frail in comparison to the x-y symmetry plane due to the lower spatial resolution. Additionally, the streamline representation of the flow field reveals the highly symmetric features of the measurement in the x-y plane in comparison to the reconstruction in the x-z plane.

Isosurfaces of the transverse velocities are added ($\frac{U_\mathrm{r}}{u_\mathrm{d}} = 0.175$) to visualize the symmetry of the 3D spatial distribution of the transverse velocities (Fig. 5.2 c). The features of the isosurfaces are generally symmetric. However, their relative position at the channel top compared to the location with respect to the side walls reveal slight asymmetry. The amplitude of the reconstructed velocities in z-direction is too pronounced: While the isosurfaces of the disperse phase remain inside the droplet in the proximity of the side wall, they clearly breach the interface towards the top wall. This corresponds to the considerations on the volume flow of Sec. 3.5.2.

5.4 Relative velocity field on the interface of the Taylor droplet

The fluid motion that is directed perpendicular to a droplet interface causes the interface to deviate from its shape at rest [82] (Chap. 4). A clean interface can not resist shear forces, thus tangential velocity components cause the fluid at the interface to move: Momentum coupling across the interface transfers kinetic energy into the droplet phase. Thus, the flow of the continuous phase drives the velocity field inside the droplet.

Fig. 5.3 a) shows the vector field of the interpolated velocity distribution on the interface. The top wall film is covered with a white area to mark a lack of available data. The velocity magnitude on the front and back caps is smaller than the interface movement in the proximity of the wall films. The interface

movement in the gutter region is directed from the front to the back of the droplet. The velocities along the gutter interface range between the fast wall movement and the slow movements on the caps.

In Fig. 5.3 b), the direction of the interface motion is given as a streamline representation. The color coding indicates the normalized relative velocity component in stream-wise direction. Fluid moving in positive x-direction relative to the velocity of the droplet is shown in red, while blue indicates motion against the downstream direction. White color shows interface regions that do not move with respect to the overall translation of the droplet. As expected, two stagnation points are identified: One is located at the front tip and one at the back tip of the droplet. In addition, two annular stagnation regions can be seen, where the forward moving core of the droplet flow separates from the backwards directed motion of the wall-driven interface.

The radius dependent transverse velocities of the interface movement are given in Fig. 5.3 c) as color coding. Red shows the fluid motion outwards to the wall, while blue indicates the inwards movement towards the x-axis. In combination with the streamlines, the stagnation points at the droplet front and back tips can be seen clearly. At the front tip, fluid elements of the interface converge into the stagnation point. At the back tip, the diverging stagnation point shows that a new interface is generated.

The annular stagnation region at the on- and offset of the wall films (and the gutters) is clearly recognizable in the transverse component of the interface motion. At the droplet front, fluid elements below a certain distance from the channel center are pulled inwards to the stagnation point. Fluid elements beyond that distance are directed outwards and are either transported into the wall films or through the gutters. At the end of the gutter and of the wall films the interfacial fluid is transported inwards towards the rear annular stagnation region. Here it meets with the outwards directed interface motion, which is driven by the rear main vortex.

The annular stagnation regions can be observed best in a rear view (Fig. 5.3 d) and a front view (Fig. 5.3 e) of the Taylor droplet. The color coding shows the transverse velocity component on the interface. The diverging stagnation point of the rear cap tip (Fig. 5.3 d) is complemented with a converging annular stagnation region. A small vortex structure is found where the fluid

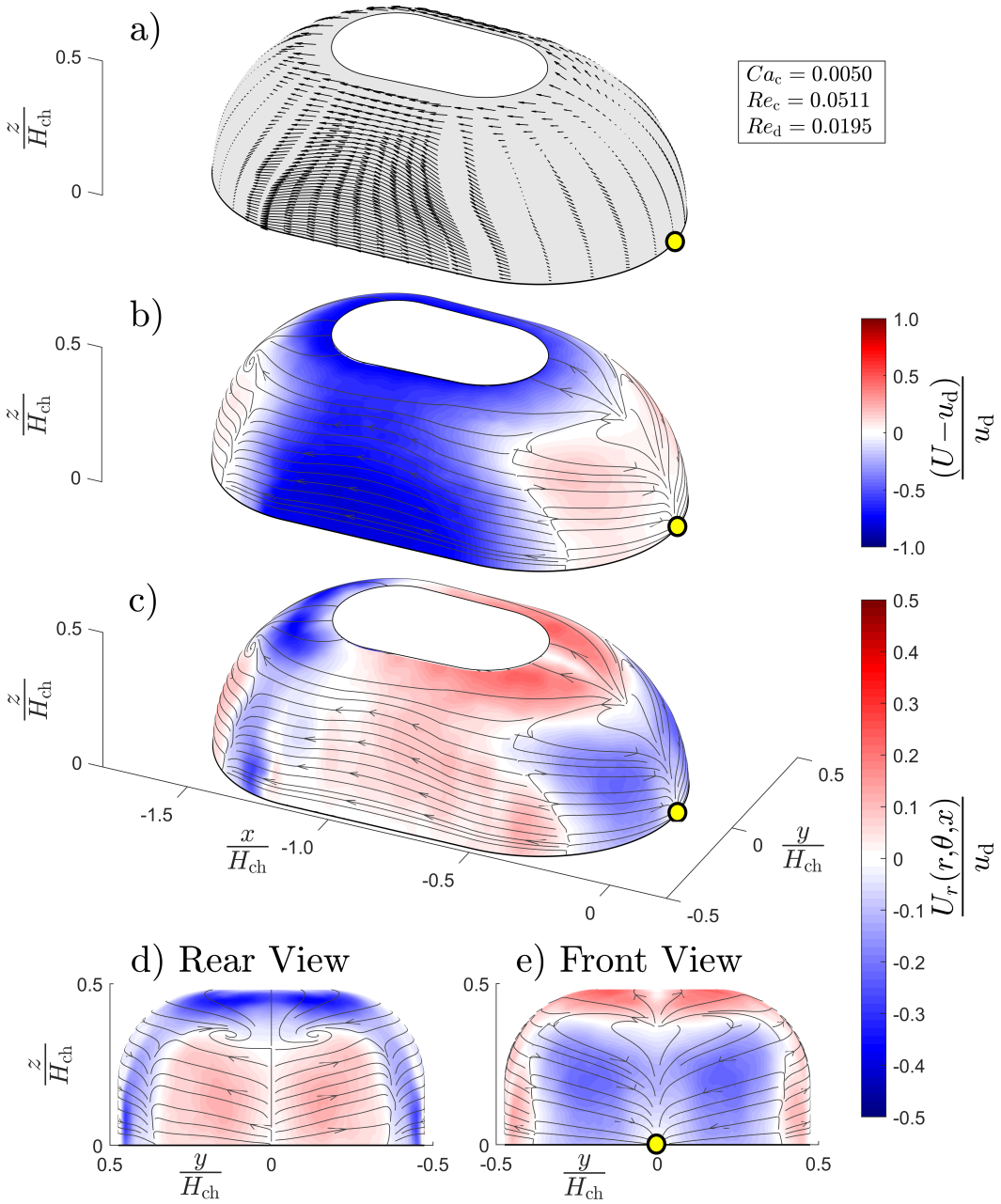

Fig. 5.3: Interpolation of the 3D-Velocity field on the interface of the Taylor droplet. The velocity information is depicted in a moving frame of reference. a) In-plane 2D vector representation of the velocity field on the mobile droplet interface. The sampling is reduced in x-y direction to improve the clarity of the graph. b) Streamline plot of the in-plane velocity distribution on the Taylor droplet interface. The color coding indicates the normalized stream-wise relative velocity of the flow. In the droplet frame of motion the walls move in negative x-direction. At the droplet top, no data is available. Thus, the section is covered with a corresponding white surface. c) In addition to the streamlines on the droplet interface, the color coding shows the radius dependent transverse velocity component (red - away from the x-axis; blue - towards the x-axis). d) Rear view d) and front view e) of the droplet indicating the same quantities as in c)

elements meet, that leave the wall film and the gutter. Symmetry suggests that a similar structure should be present at the corresponding location on the wall in y-direction. However, the spatial resolution in z-direction does not allow to detect any small filaments. In the front view (Fig. 5.3 e) of the droplet interface motion a divergent annular stagnation region produces a new interface, which converges into the frontal stagnation point.

A comparison of the relative radial location of the two annular stagnation regions shows, that both of them follow the shape of the channel cross section. However, the frontal stagnation region reaches in an outwards direction further into the gutter region and results in a pillow shape. In contrast, the rear stagnation region is shifted inwards towards the center axis of the microchannel and maintains a more oval shape.

5.5 Stagnation regions

The 3D distribution of stagnation regions inside and outside of the Taylor droplet (Fig. 5.4) is investigated using the relative flow field. Its absolute magnitude is computed, the scalar values are normalized with the droplet velocity ($\sqrt{(U-u_\mathrm{d})^2+V^2+W^2}/u_\mathrm{d}$) and the result is projected on the interface and the x-y and x-z symmetry planes. In addition, isosurfaces of the relative velocity magnitude at a dimensionless level of 0.075 indicate stagnation regions. The threshold corresponds roughly to a fraction of less than 1% of the present continuous phase kinetic energy. It is chosen such that all stagnation regions are clearly visible.

At the back (Fig. 5.4 a) and at the front (Fig. 5.4 b) of the droplet, the stagnation region breaches the interface and indicates its location with respect to the droplet shape. At the droplet back the region is connected, while at the front, the stagnation point at the droplet tip is separated from an annular stagnation region. The outer shape of both stagnation regions clearly follow the cross section shape of the microchannel.

To show the relative location of the stagnation regions with respect to each other Fig. 5.4 c) shows an elevated side perspective. At the location of the annular stagnation region, the outer vortices attach to (droplet front) or

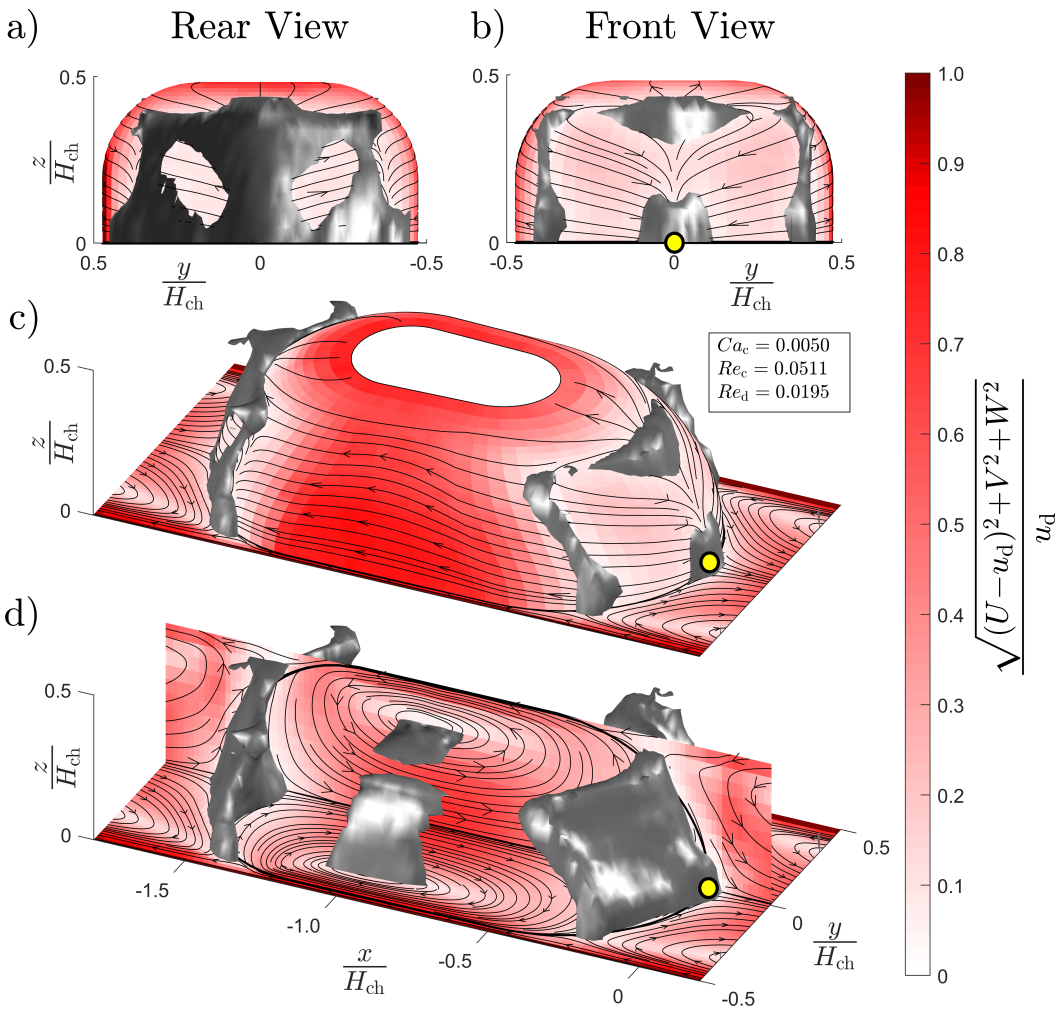

Fig. 5.4: Visualization of stagnation regions using isosurfaces (Threshhold: 0.075). The depicted scalar quantity is the absolute value of the relative velocity field. The velocity field information is depicted in a moving frame of reference. Rear view a), front view b) and elevated side view c) visualize the 3D location of the stagnation regions with respect to the droplet interface. In a), b) and c) the streamlines on the interface indicate the motion of the droplet surface. d) reveals according stagnation regions inside the droplet and the location of the core of the main disperse phase vortex. The interface shape at the droplet top film is covered in white, since no data is available that can be projected to this location

detach from (droplet back) the interface. Here, the hydrodynamic forces of the flow interact strongly with the interface to deform the droplet [40]. The corner of both outer stagnation regions mark the entrance of the gutter, where continuous liquid bypasses the droplet. The streamline pattern of the interface motion coincides with the visualization of the absolute magnitude of the relative velocity.

Without the interface, one can observe the entire extent of the stagnation regions (Fig. 5.4 d). The isosurfaces cover a major part of the secondary vortices inside the droplet caps. Additionally, the annular core structure of the wall-driven main vortex of the disperse is prominent, since it is a region of low relative velocity compared to the motion of the Taylor droplet. The position agreement of the main vortex center on the x-z symmetry plane and the location of 3D stagnation region at the vortex core demonstrates the symmetry of the 3D-flow field.

5.6 Shear rate distribution

The shear rate is related to the magnitude of the strain. Its normalized absolute amplitude is used to establish a scalar quantity to visualize the strain distribution in and around the Taylor droplet as well as to locate the strain maxima (Fig. 5.5).

The shear rate distribution on the symmetry planes in x-y and x-z direction shows the expected general increase from the microchannel center towards the walls (Fig. 5.5 a). The wall shear rate decreases in the proximity of the cap interface, since at these stagnation regions the velocities and their gradients are low. At the longitudinal center of the main vortices, the relative wall motion that drives the flow causes a clear shear rate increase. A comparison of the shear rate on the symmetry planes reveals a general similarity. However, the errors introduced by the reconstruction (above the cap stagnation points in z-direction) and the noise increase due to the derivatives have a recognizable impact. In addition, delicate structures on the x-y plane can not be observed in the perpendicular plane.

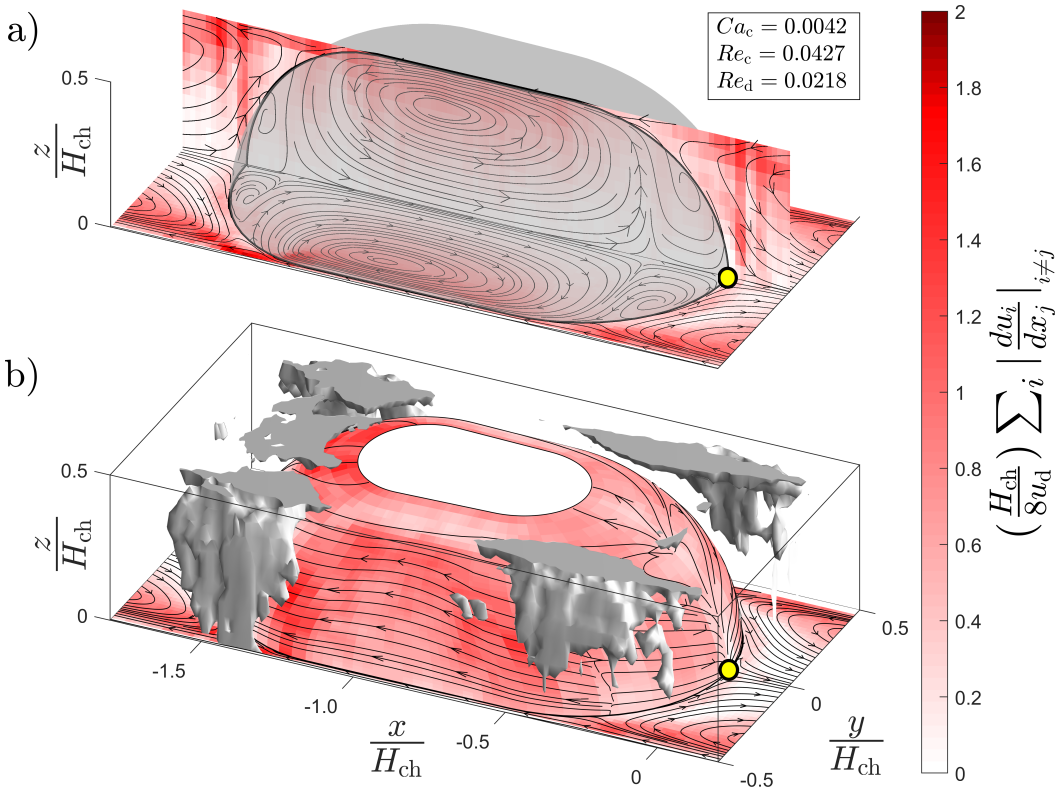

Fig. 5.5: Absolute values of the normalized shear rate inside and around Taylor droplet indicating strain. The velocity information is depicted in a moving frame of reference. a) Normalized shear rate distribution on the symmetry planes (x-y and x-z direction) of the flow. b) Isosurfaces (dimensionless threshold level: 1.5) to expose the location of maximum strain. The maximum strain is located at gutter and wall film entrances and respective exits. The interface model is artificially closed at the top film

The normalized shear rate information at the interface position and isosurfaces of an elevated shear rate (dimensionless threshold level: 1.5) enables analysis of the impact of the strain location on the Taylor droplet shape (Fig. 5.5 b). At the droplet front cap, the strain location coincides with the position of pressure build up. Fluid decelerates and the continuous phase either evades the interface and converges into the gutter and the wall films or the flow is forced to reverse with respect to the droplet translation. The position of the shear rate maximum overlaps with the corner of the annular stagnation region, which can be identified in Fig. 5.4 c). The pressure increase at the stagnation region squeezes and elongates the front cap in flow direction from its spherical shape at rest.

At the droplet back cap, the strain location coincides with the position of pressure release. The continuous phase accelerates and diverges from the wall films and the gutters until it merges with the reversing flow of the rear main vortex. The location of the shear rate maximum at the back coincides with the corner position the annular stagnation region (Fig. 5.4 c). The interface is being pulled towards the wall. In combination with the pressure build up at the rear stagnation point, a compressed deformation in the main flow direction is achieved with respect to the undeformed static droplet shape.

5.7 Vortex strength: λ_2-criterion

The λ_2-criterion corresponds to the pressure minimum on a planar section through the flow and is applied to represent vortex core geometry [48]. A vortex is defined as a connected region, where λ_2 is negative. Hence, only negative values are depicted in Fig. 5.6.

Two sections through the scalar field of the λ_2-criterion on the symmetry planes of the Taylor flow (x-y and x-z direction) (Fig. 5.6 a) enable to detect the main features and to judge the data quality. On the x-z plane, the main wall-driven vortices are as clearly recognizable as they are on the delicately featured x-y plane. However, the velocity derivatives in z-direction amplify the noise of the reconstructed velocity z-component.

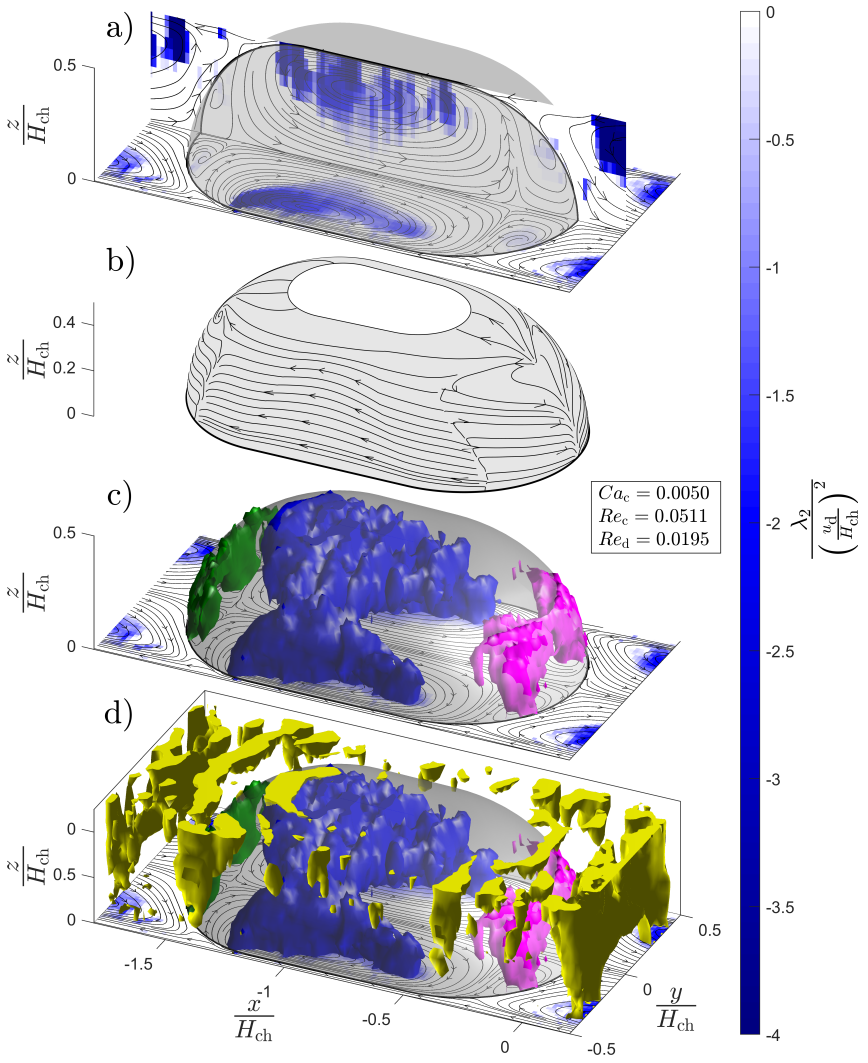

Fig. 5.6: Application of the λ_2-criterion to visualize the vortices inside and outside of the Taylor droplet. Solely negative values are depicted, since only connected negative regions represent the pressure minima of vortices. The presented velocity information is depicted in a moving frame of reference. a) Scalar representation of the λ_2-criterion on the symmetry planes of the Taylor flow (x-y and x-z plane through the origin): The derivatives of the veloctiy reconstruction introduce a significant amount of noise. b) The fluid motion on the interface causes the inner circulation of the Taylor droplet. The streamline pattern of the interface motion is depicted separately to improve the clarity of Fig. 5.6 c) and d). c) Isosurface visualization of the vortices inside the disperse phase only: The main vortex is about 4 times stronger compared to the front vortex, which in turn is about 3 times stronger than the rear secondary structure. Derivative-induced noise is clearly visible at the main vortex in the proximity of the top wall. The threshold of the main vortex (blue isosurface) is set to -1.28 to follow the outline of the vortex in the x-y symmetry plane. For the secondary vortices different threshold levels are chosen for the front (-0.24, magenta isosurface) and the back of the droplet (-0.08, green isosurface) to visualize their 3D extent inside their respective caps. d) λ_2 representation of the continuous phase flow is added: The recognition of coherent structures becomes increasingly difficult due to the noisy data at the wall

The fluid motion on the interface causes the inner circulation of the Taylor droplet. The streamline pattern of the interface motion is depicted separately from the vortex visualization to maintain clarity (Fig. 5.6 b). Isosurfaces are used inside the disperse phase only, to visualize both: the large main vortex and the smaller counter rotating secondary structures of the front and back of the droplet caps (Fig. 5.6 c). The main vortex (blue isosurface) is not strictly toroidal as one might expect from Taylor flows in circular tubes, but its structure reflects the square channel geometry. The extent of the main vortex in the plane of the cross section diagonal and along the main flow axis is decreased towards the droplet front. Nonetheless, the main recirculation maintains its symmetry with respect to the channel dimensions. The noise, attributed to the squared and summed derivatives of the reconstructed velocity components, is noticeable in the proximity of the top wall of the channel.

The location of the secondary vortices (green and magenta isosurface) that compensate the rotation direction of the main recirculation coincide with the stagnation region identified in Fig. 5.4. Despite their low values of λ_2 both structures are clearly detectable and carry a channel related symmetry. In addition, the shape and orientation of the secondary vortices match the location of the streamline pattern on the droplet interface (Fig. 5.6 b).

In the droplet frame of motion, the wall movement directly drives the main vortices in the slug between the droplets. It also moves the separating film between the wall and the droplet. The flow inside the droplet is generated by the momentum transfer across the interface and therefore the velocity on the interface drives both, the main and the secondary vortices inside the droplet. The magnitudes of the interface velocities determine the spatial extension of vortices. While the main vortex is powered by the strong streamwise flow of the wall film, the secondary vortices are driven by transverse velocities, which are an order of magnitude smaller.

Adding the λ_2 vortex detection of the continuous phase to the graph, the presence of the main vortex of the adjacent slug can only be anticipated (Fig. 5.6 d), yellow isosurface). Despite choosing the identical threshold as for the main vortex in the droplet (-1.28), the noise of the reconstructed data set prevents a clear detection of its structure.

5.8 Conclusion

A μPIV study on the 3D2C velocity distribution of Taylor droplets moving in a square horizontal microchannel is conducted. The third velocity component is reconstructed and the result is verified (Sec. 3.5.2) based on the volume flow in stream-wise and transverse flow directions. The Taylor droplets dilate the PDMS channel walls and cause the stream-wise volume flow to be underestimated up to -4.7%. The mean deviation of reconstructed velocity in z-direction is found to be $\pm 2.7\%$, while the maximum deviation amounts to -6% of Q_{tot}. In y-direction the deviation of the ensemble correlation μPIV is quantified to reside below $\pm 0.1\%$.

The completed 3D3C velocity field is used to investigate the stagnation regions of the 3D flow. In combination with the interface approximation of Mießner et al. [82] (Chap. 4), the location of the stagnation regions reveals expectable stagnation points at the cap tips of the Taylor droplet. In addition, an annular stagnation region is visualized closer to the walls, where the main outer vortices attach to or detach from the interface. It is at this location, that the hydrodynamic forces applied on the interface cause the droplet deformation.

The maximum shear rate is found at the entrances and exits of the wall films and the corner flow (gutter) bypassing the Taylor droplet. This straining location macroscopically corresponds to the cap position of the Taylor droplets.

For the first time, an experimental data set allows to visualize the streamlines of the velocity distribution on the interface of a Taylor droplet and to directly relate it to the main and secondary vortices of the velocity field. A small vortex structure is found in the stagnation region at the back of the droplet, where the fluid elements that leave the wall film and the gutter meet.

The evaluation methods which have been developed for this study allow to investigate laminar quasi-stationary and pulsating flows. Determining the shear rate distribution helps to effectively handle fragile educts and/or products in single phase as well as in multiphase microfluidic flows, e.g. organ-on-a-chip applications and cell handling applications using droplets [24].

6

Pressure field and energy dissipation

Once there were some particles
Their moves were clearly visible
Excited bright, exposed to pressure
Plain delight, agreed to measure
Results turned out - a major treasure

In this study, the 3D pressure field is reconstrcuted and the 3D contributions of the energy dissipation is derived from a 3D3C velocity field measurement of Taylor droplets moving in a horizontal microchannel ($Ca_c = 0.0050$, $Re_c = 0.0519$, $Bo = 0.0043$, $\lambda = \frac{\eta_d}{\eta_c} = 2.625$). The pressure field is devided in a wall-proximate part and a core-flow to describe the phenomenology. At the wall, the pressure decreases expectedly in downstream direction. In contrast, a reversed pressure gradient is found in the core of the flow that drives the bypass flow of continuous phase through the corners (gutters) and causes the Taylor droplet's relative velocity between the faster droplet flow and the slower mean flow.

Based on the pressure field the driving pressure gradient of the bypass flow is quantified and verified by a simple estimation method: the geometry of the gutter entrances deliver a Laplace pressure difference. As a direct measure for the viscous dissipation, the 3D distribution of work done on the flow elements is calculated, that is necessary to maintain the stationarity of the Taylor flow.

The spatial integration of this distribution provides the overall dissipated energy and allows to identify and quantify different contributions from the individual fluid phases, from the wall-proximate layer and from the flow redirection due to presence of the droplet interface.

For the first time, deep insight is gained into the 3D pressure field and the distribution of the energy dissipation in the Taylor flow based on experimentally acquired 3D3C velocity data. The 3D pressure field of and the 3D distribution of work is provided as supplementary material to enable a benchmark for CFD and numerical simulations.

A comparison between the pressure distribution and the curvature-derived Laplace-pressure on the interface of a Taylor droplet identifies the source of the motion-related droplet deformation. Next, the pressure gradient that drives the by-pass flow through the gutters is quantified, and an easy-to-access estimation method is verified. The analysis of the 3D pressure distribution inside and outside the Taylor droplet explains the mean pressure profile in stream-wise direction. Finally, the energy dissipation of the droplet is discussed based on the 3D distribution of the work done on the Taylor flow.

In the following sections, the Taylor droplets move in the positive x-direction. Their front tip is situated in the origin of the coordinate system, while their back cap tip is located at $x/H_{\mathrm{ch}} = -1.58$.

6.1 Overview

To control the flow stability of subsequent Taylor droplets one needs to understand and control the pressure drop inside and outside the disperse phase. The challenge becomes obvious when considering microchannel-parallelization as a commonly used strategy to increase the throughput. Uniform flow conditions are desirable to achieve continuous and stable processes in all branches of a parallelized microreactor [10]. Fluctuations of the two-phase flow change the product quality, since the process deviates from the optimal working point.

The stabilization of parallel flows requires to control the individual droplet formation at low capillary number and low Reynolds number. This formation process feedbacks sensitively to downstream pressure changes in a microchannel. The droplet shedding frequency as well as the droplet length are affected by pressure shifts [118]. At a constant volume flow rate and for a given surfactant-free material combination between two immiscible phases, only the droplet length determines its hydraulic resistance. The hydraulic resistance influences the actual droplet velocity, which finally determines the droplet residence time in a microchannel [41]. Thus, to control the flow stability of a Taylor droplet chain one needs to understand and control the pressure drop inside and outside the disperse phase.

Droplets in rectangular capillaries are less often addressed theoretically and fewer models exist than for Taylor flow in circular capillaries - pioneering work for the latter has been published by Bretherton [15]. An early correlation for rectangular capillaries that describes the pressure drop was published by Lockhart and Martinelli [73] in the form of friction factors. To date a variety of analytical models have been published: The relevant forces have been explained by Kreutzer et al. [61] and later expanded by Abiev [4]. The pressure profile is analyzed and the relevant flows for the pressure drop are recognized [3]. This author suggests to use the shape of the Taylor droplet interface to determine the local pressure distribution. Balestra et al. [11] and Vivekanand and Raju [114] add simulative work to the problem. Yue et al. [126] developed a correlation for liquid/liquid slug flow in rectangular microchannels and Ładosz and von Rohr [65] extended their models and focused on the influence of the wall-film as proposed by Jovanović et al. [51].

Experimentally, a variety of measurement approaches have been used to characterize the pressure fluctuations and frictional pressure drop caused by Taylor droplets in microchannels. Techniques such as optical tweezers [49], Laplace-pressure sensors [2, 99, 124] and also membrane cavities in DRIE-echted reactors have been used [86] in devices of small channel height $H_{\mathrm{ch}} < 500\mu$m. In larger microchannels, mostly adapted conventional pressure sensors were applied, which allow to measure the total pressure at the entrance and exit of the microchannel to calculate the pressure drop along the entire channel [75, 89, 116]. Despite relying on integral information

about entire droplet chains, Wang et al. [117] showed the importance of the wall contact angles for the magnitude of the pressure drop. The pressure drop caused by droplet trains in pressure-driven flows has been examined by Jakiela [45], who also worked on the influence of droplet length and presents a measurement device for networks.

All of these approaches measure either the pressure at a distinct position at the channel walls or integrally over a number of droplets. For modeling purposes and further understanding of the underlying effects, spatially resolved pressure measurements are necessary. However, a 3D pressure field of a Taylor droplet extracted from a measurement has not yet been published.

With the intention to close this gap, this study is based on the μPIV-measurement of Mießner et al. [83] (Chap. 5). Their study provides the 3D3C velocity field in and around quasi-stationary Taylor droplets moving in a horizontal square microchannel. In the underlying experiment the surface tension forces dominate the viscous forces. Thus, the capillary number is small $Ca_\mathrm{c} = \frac{\bar{U}\eta_\mathrm{c}}{\sigma} \ll 1$. Herein, σ is the interface tension, η_c denotes the dynamic viscosity of the continuous phase and $\bar{U} = \frac{Q_\mathrm{c}+Q_\mathrm{d}}{A_\mathrm{ch}}$ represents the total superficial velocity of the flow. This average velocity is derived from the total volume flow through the area of the channel cross-section A_ch, where Q_c and Q_d are the volume flows of the continuous and the disperse phase, respectively.

In this context, the droplet velocity u_d is not useful for the definition of dimensionless numbers, since it is a flow dependent variable [41]: Continuous phase bypasses the droplet through the gutters from the droplet front to its back and causes a relative velocity $u_\mathrm{rel} = u_\mathrm{d} - \bar{U}$ of the Taylor droplet. Therefore, the droplet travels faster than the average flow $\bar{U}$ depending among other variables on the magnitude of the average flow velocity. Please note, that the total volume flow calculated from the velocity field [83] (Chap. 5) is smaller (94.44% $\pm$ 1.2 %) than the superimposed volume flow Q_tot discussed above due to channel deformation. This circumstance impacts the direct calculation of the relative velocity from the setup data given in Tab. 3.2.

A low Reynolds number $Re_\mathrm{c} = \frac{\rho_\mathrm{c}\bar{U}H_\mathrm{ch}}{\eta_\mathrm{c}} \leqslant 1$ relates the weak inertia forces to the dominating viscous forces and indicates Stokes-flow conditions. Herein, ρ_c denotes the density of the continuous phase, and H_ch is the channel height.

A low Bond number $Bo = \frac{\Delta\rho g H_{\mathrm{ch}}^2}{\sigma} \ll 1$ indicates a negligible influence of the buoyancy forces on the droplet shape. Herein $\Delta\rho$ denotes the density difference between the two phases, and g is the gravitational acceleration. The governing forces for the investigated Taylor flow given in descending order are the interfacial tension forces, the viscous forces, the buoyancy forces and the inertia forces ($Ca_{\mathrm{c}} = 0.0050, Re_{\mathrm{c}} = 0.0519, Bo = 0.0043$).

In this study, the measured 3D3C velocity field of Taylor droplets [83] (Chap. 5) is used two-fold: to reconstruct and investigate the 3D pressure field as well as to derive and discuss the contributions of the energy dissipation in the Taylor flow.

- At first, the Navier-Stokes equation is applied to the velocity field of the Taylor flow and the subsequent spatial integration calculates the 3D field of the pressure in and around a Taylor droplet. In this context, the calculation of the momentum thickness helps to discriminate between wall-influenced flow and the remaining core of the flow. While the gradient of the pressure inside the wall-layer points downstream as expected, a pressure gradient inversion with respect to the flow direction is found, and experimental evidence of the postulation of Abiev [3] is provided. This reversed pressure gradient in the core of the flow drives the bypass flow of continuous phase through the corners (gutters) and gives rise to the Taylor droplet's relative velocity [41]. To quantify the driving pressure gradient along the gutter, the Taylor droplet interface approximation of Mießner et al. [82] (Chap. 4) is applied twice: to evaluate the experimental data of the pressure field directly at the interface position and subsequently to establish and verify an estimation method for the calculation of the gutter gradient.

- Secondly, the viscous forces of the flow field and the velocity distribution is used to calculate the 3D field of work done on the flow elements. This work maintains the stationarity of the Taylor flow. The spatial integration of this distribution allows to identify and quantify different contributions to the losses of the flow: e.g. the properties of the individual fluid phases, the wall-influence and the flow redirection by the interface (Fig. 6.1). The total work done on the flow represents the mechanical energy introduced to the Taylor flow to maintain stationarity, i.e. to compensate for the viscous dissipation.

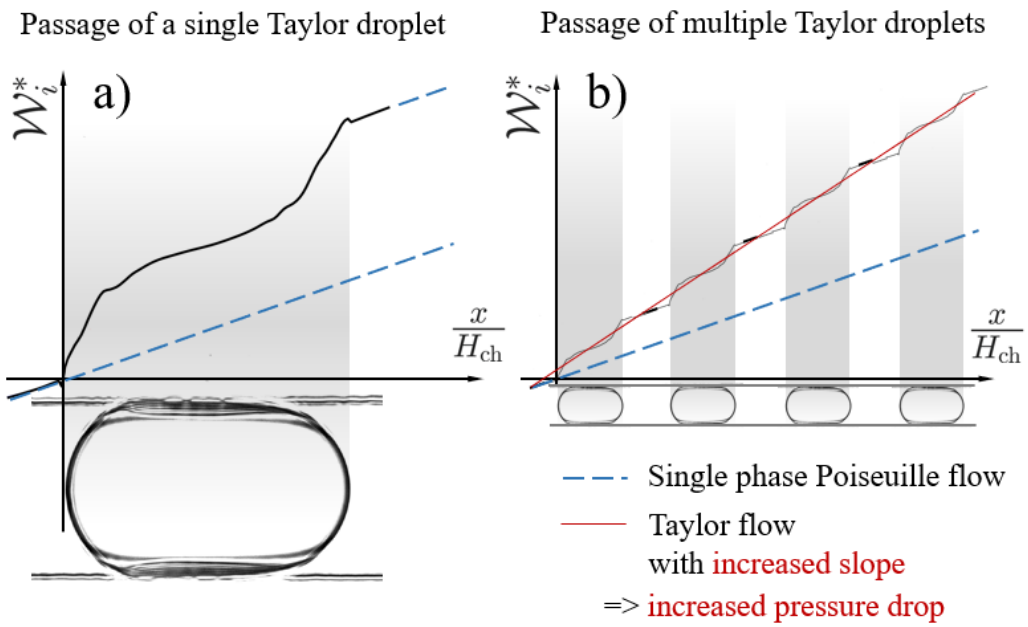

Fig. 6.1: Qualitative sketch comparing the viscous dissipation of a single-phase flow with that of a Taylor flow: In a stationary flow subjected to internal friction, energy is dissipated and work $\mathcal{W}_i^*$ needs to be done on the flow to compensate for the loss of mechanical energy. a) A stationary laminar viscous single-phase flow in a straight microchannel (blue dashed line) needs work done on the flow to solely overcome the wall-shear, thus the increase of work inflow direction is linear. The presence of a droplet interface redirects the flow field, adds energy loss to the shear contribution and increases the amount of work done on the flow at the droplet caps, where the directional change takes place (solid black line). b) In a stationary Taylor droplet chain, the contribution of each droplet sums up to an overall increased amount of work done on the flow (thin red line) in comparison to the single-phase flow

Three major benefits can be drawn from this work: i) the experimental validation of the analytical quantification method that estimates the magnitude of the reversed pressure gradient in the gutter of Taylor droplets, ii) the 3D pressure field and iii) the 3D distribution of mechanical work done on the flow. The pressure and the data of work done is offered as supplementary material to enable a benchmark for CFD and numerical simulations.

6.2 Pressure difference on the droplet interface

The flow field in and around a moving Taylor droplet deforms the interface from its shape at rest. Abiev [3] suggests to make use of the flow related interface deformation to estimate the pressure distribution. The geometry-based model data and a flow-based approach based on experimental data is used to quantify and compare the pressure difference on the droplet interface in Fig. 6.2. The pressure differences are normalized with the driving pressure for a single-phase Poiseuille-flow of continuous phase material ($Q_{\mathrm{HP}}, c = Q_{\mathrm{tot}}$) through an equivalent channel cross section of droplet length L_{d}. A positive pressure refers to forces that act on a area element $\mathrm{d}A$ against the outwards pointing surface normals (Fig. 2.6b): As a result the pressure pushes the interface inwards. The interface is moved outwards at regions of negative pressure. The green arcs mark the geometric entrances and exits of the gutters.

Fig. 6.2a shows the Laplace-pressure difference (Eq. 2.9) derived from the geometric interface approximation. The interface approximation produces artifacts when used as the source for second-order information (e.g. the interface curvature). The 2D Laplace-pressure profile on the interface exhibits discontinuities at the joints of different interface parts: i) at the entrances and exits of the gutter and the wall-film and ii) at the joints of the wall-films. In addition, the droplet interface at the wall-film does not show any sign of deformation which is in contradiction to the findings of [62]. Both, the artifacts and the absence of pressure in wall-films are the result of the simplification of the geometric boundary conditions and the assumptions that allowed to retrieve geometric first-order information, like the location of the Taylor droplet interface.

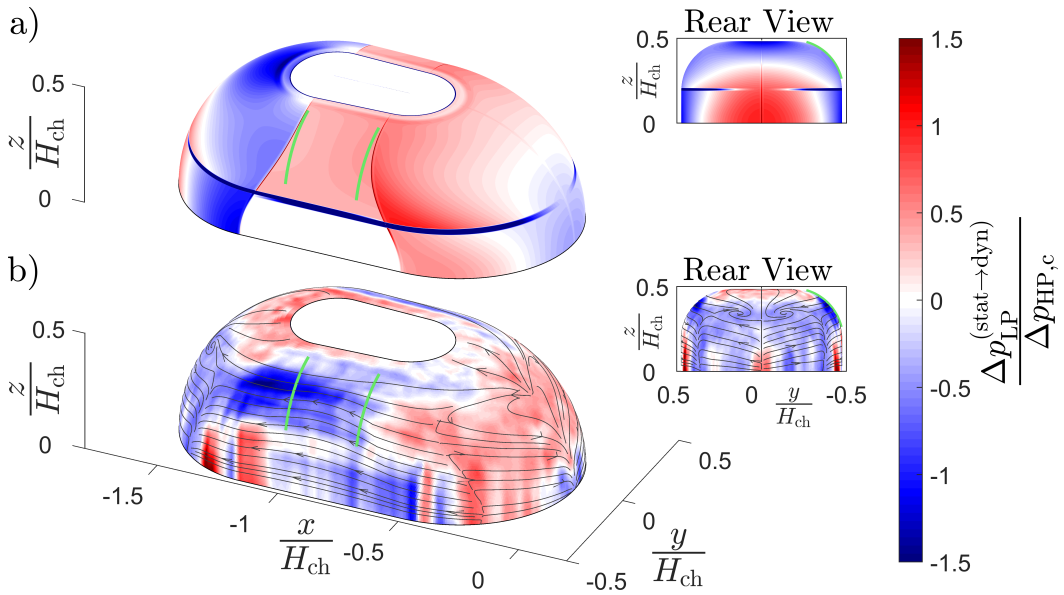

Fig. 6.2: Pressure distribution on the interface of a moving Taylor droplet. The approximate interface shape model of Mießner et al. [82] (Chap. 4) delivers the position of the dynamically deformed interface. Positive pressure (red) pushes the interface inwards (Fig. 2.6b). The interface is moved outwards at regions of negative pressure (blue). The green lines indicate the entrance and exit of the gutter that accommodates the bypass flow of the continuous phase. A rear view of the respective pressure distribution on the droplet interface enhances comparability. a) The difference between the curvature distribution of a Taylor droplet at rest and in steady motion allows to calculate the pressure distribution from the Laplace-pressure of both cases. The result relies entirely on the accuracy of the curvature of the interface approximation. b) The 3D velocity data of the μPIV measurement of [83] (Chap. 5) is used in the Navier-Stokes equations to calculate the pressure distribution on the interface of a moving droplet. Additionally, the fluid motion on the 2D interface is interpolated and represented with streamlines.

Despite these drawbacks, qualitative information on the droplet deformation from its static shape can be observed. The elongation of the front cap is caused by a suction region at the droplet's tip (blue) and followed by a region of positive pressure that moves the interface inwards. At the droplet's back cap the interface is initially pulled outwards behind the gutter exits and wall-film regions and subsequently compressed at the tip. Both qualitative results correspond to the cap deformation described by the experimentally derived correlation of Helmers et al. [40].

Fig. 6.2b depicts the pressure difference derived from the velocity field (Eq. 2.7 used in Eq. 2.4) at the interface of the Taylor droplet. In addition to the pressure information, the streamlines of the interface motion are shown [83] (Chap. 5).

The white area at the top wall-film artificially closes the droplet. The interface gap exists due to a lack of measurement data. However, the flow symmetry allows access to the pressure conditions in the films at the side wall-film instead.

The effect of the front cap elongation and the back cap compression is clearly present in the measurement-based pressure. The general magnitude range of the pressure distribution is comparable between the two approaches. The cap deformations arise from the relative motion of the main vortices in the slugs. The ring shape stagnation region at the droplet front indicates the location where the slug's wall-driven vortex attaches to the interface, while it detaches again at the droplet front tip. The pressure rises due to the viscous displacement that takes place between attachment and detachment. The influence of the detachment is smaller than predicted by the geometric representation (Fig. 6.2a). At the droplet back, inverted flow conditions with respect to the interface cause the back cap compression.

The pressure evolution from the wall-film entrance at the droplet front towards its rear exit shows a series of pressure changes. At the frontal stagnation region, the liquid of the continuous phase is either redirected to the droplet tip or in the direction of the wall-film. At the onset of the film the outer liquid is forced into the film and the pressure rises. After the transport of fluid through the film, the film-thinning increases the pressure. At the exit of the film, the liquid flows towards the ring-shaped stagnation region at

the back, where it slows down again. This series of pressure changes feed back to the interface and coincide with the location where the onset of the bullet-shape for increased Ca_c is situated [109].

The pressure distribution along the gutter appears to be different compared to the geometric approach. While the magnitudes of the pressure at the gutter entrances are similar, the distribution in gutters deviates. The geometric approach delivers positive Laplace-pressures, while the flow-based pressure carries a negative sign. However, in both cases the pressure decreases from the front to the back of the gutter. Thus, the pressure gradient points into the same direction - against the flow direction of the Taylor droplets. This confirms the postulated pressure gradient inversion with respect to the flow direction by Abiev [3].

6.3 Pressure gradient of the by-pass flow in the gutter

An estimation of the pressure gradient along the gutter allows the determination of the volume flow through the gutter and calculation of the relative velocity [41]. Based on the droplet interface geometry, two possibilities to analytically obtain the pressure along the gutter are feasible: an evaluation of i) the curvature difference distribution between the static and the dynamic Taylor droplet shape (Fig. 6.2a, Eq. 2.9) and ii) the Laplace-pressure difference between the mean gutter radius at the front and back of the gutter. The gutter radii are calculated as a by-product of the interface approximation [82] (Chap. 4).

The measurement-based pressure difference is used as a reference to asses the accuracy of the theoretical approaches (Fig. 6.3). For this purpose, the distribution in the gutter is averaged in transverse direction (blue triangles). The measurement resolution in the x-direction of the source velocity field serves as sampling grid distance in flow direction. The schematic inset of Fig. 6.3 visualizes the sampling method for the gutter gradient. The offset of pressure at the back end of the gutter is removed. The result is normalized with the driving pressure of a single-phase Poiseuille-flow of continuous phase

material ($Q_{\mathrm{HP}}, c = Q_{\mathrm{tot}}$) through an equivalent channel of gutter length L_{g} to quantify the influence of the droplets presence.

A linear fit to the averaged pressure difference (blue solid line) allows to estimate the overall gutter pressure gradient of the experiment. The confidence interval of the slope ($\pm 9.1\%$) is calculated to quantify the influence of the standard deviation of the measurement from the linear fit on the gradient (blue area).

The Laplace-pressure difference due to the geometric droplet deformation is averaged in the same manner ($\circ$) and a linear fit allows to estimate the pressure gradient in the gutter. Clearly, the slope of the model surface fit is half as steep as the pressure gradient of the measurement is (-55.4%). We attribute the deviation between the Laplace pressure difference of the gutter entrances (black dashed line) and the model's mean curvature distribution (black dotted line) to the simplifications introduced to calculate the grid points of the interface shape. Thus, the curvature difference of the approximate interface can not be used to estimate the gutter gradient.

In contrast, the calculation of the gutter gradient with the Laplace-pressure difference between the mean gutter radius at the front and back of the gutter leads to a suitable estimation (Fig. 6.3, dashed line). The result lies well inside the variance of the measured slope ($+2.7\%$). The gray area indicates the sensitivity to a $\pm 25\%$ slope change of the gutter radius approach. Thus, the approach of Helmers et al. [41] to estimate the driving pressure gradient of the gutter from the gutter radii is confirmed by the results presented here.

6.4 3D pressure field

In disregard of a reference pressure and of the Laplace-pressure at rest, the presented 3D field solely shows the pressure that drives the flow inside and outside of the Taylor droplet. The flow is directed from left to right. Streamlines in a frame of reference relative to the droplet motion are given on half of the central symmetry plane (Fig. 6.4a). Bernoully's principle does

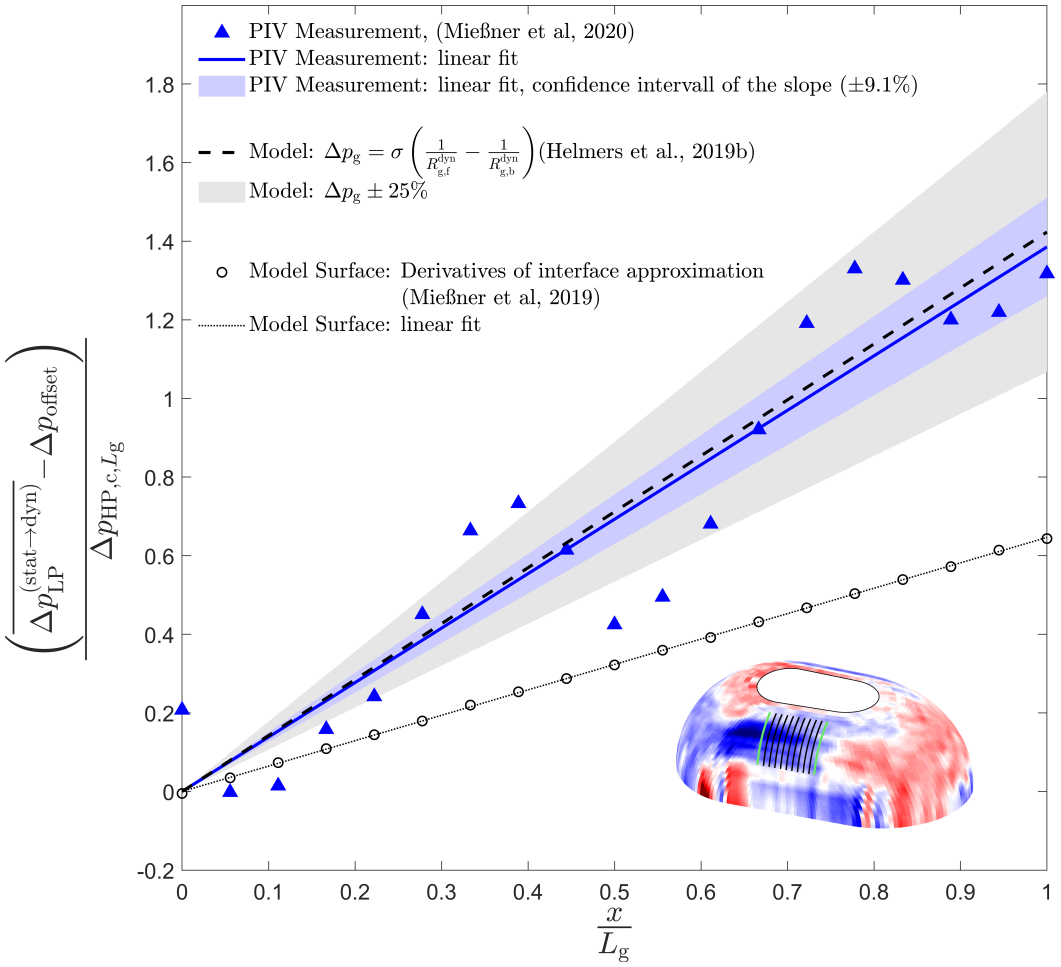

Fig. 6.3: Mean pressure gradient that drives the bypass flow through the gutter as a function of gutter lengths. Offsets are removed to directly compare between measurement data (blue) and two model-based estimations of the pressure gradient in the gutter. The linear fit of the measurement data (solid blue line) is used as reference. The blue area visualizes the uncertainty of the slope ($\pm 9.1\%$), based on the deviation of the linear fit (blue line) from the measurement (blue triangles). The gutter radii at the entrance and exit of the gutter (green lines on the interface) are used to directly estimate the pressure gradient. The slope (black dashed line) agrees with the measured pressure gradient along the gutter. The gray area visualizes the sensitivity of the pressure gradient on the gutter radius estimation ($\pm 25\%$)

not apply, since the viscous forces are 20 times stronger than the inertia forces ($Re_c = 0.05$, Stokes-flow conditions).

The pressure field of the Taylor droplet generally shows two different regions for its evolution: The pressure field in a layer close to the wall δ_2 and in the remaining core of the field. Inside the wall-proximate layer the pressure decreases as expected in stream-wise direction. However, the direction of the pressure gradient reverses in the core of the flow.

In the core flow, the pressure builds up at the droplet front due to viscous displacement. The outer main vortex in the slug is forced to change direction due to the interface at the droplet front. This elevated pressure in front of the droplet is the actual pressure source that drives the by-pass flow through the gutters [3] and gives rise to the relative velocity.

The wall-driven main vortex B inside the droplet strongly changes the flow direction to evade the secondary vortices (A, C) that connect the inner to the outer field. Two regions of the droplet's main vortex inner region B stand out: the converging rear develops a positive pressure, while the diverging front shows a negative sign.

The fundamental change of pressure conditions between the outer layer δ_2 and the core of the flow is attributed to the presence of shear at the wall (Fig. 6.4a). In case of the experimental conditions applied here, the thickness of the wall-sproximate layer amounts to δ_2. Perpendicular to the center plane (Fig. 6.4a), four sections are chosen to investigate the pressure evolution from the wall (Fig. 6.4b) towards the core of the flow (Fig. 6.4e). The black line indicates the position of the Taylor droplet interface. The pressure distribution at the wall (Fig. 6.4b) correlates with the droplet motion: increased pressure on the left causes the droplet motion downstream towards the right, while showing a decreasing pressure level.

To emphasize the change of the pressure gradient from the wall towards the core of the flow (Fig. 6.4b-e), the pressure is averaged in the z-direction to receive a pressure profile in downstream direction (Fig. 6.4f-i). A linear fit illustrates the change of pressure gradient (red lines). An inversed pressure gradient with respect to the flow direction is present at a wall distance of $\tilde{y} = \frac{\delta_2}{H_{ch}} = 1/15$. It seems that the core flow is moved through the microchannel and causes the shear-related pressure loss in the wall-layer.

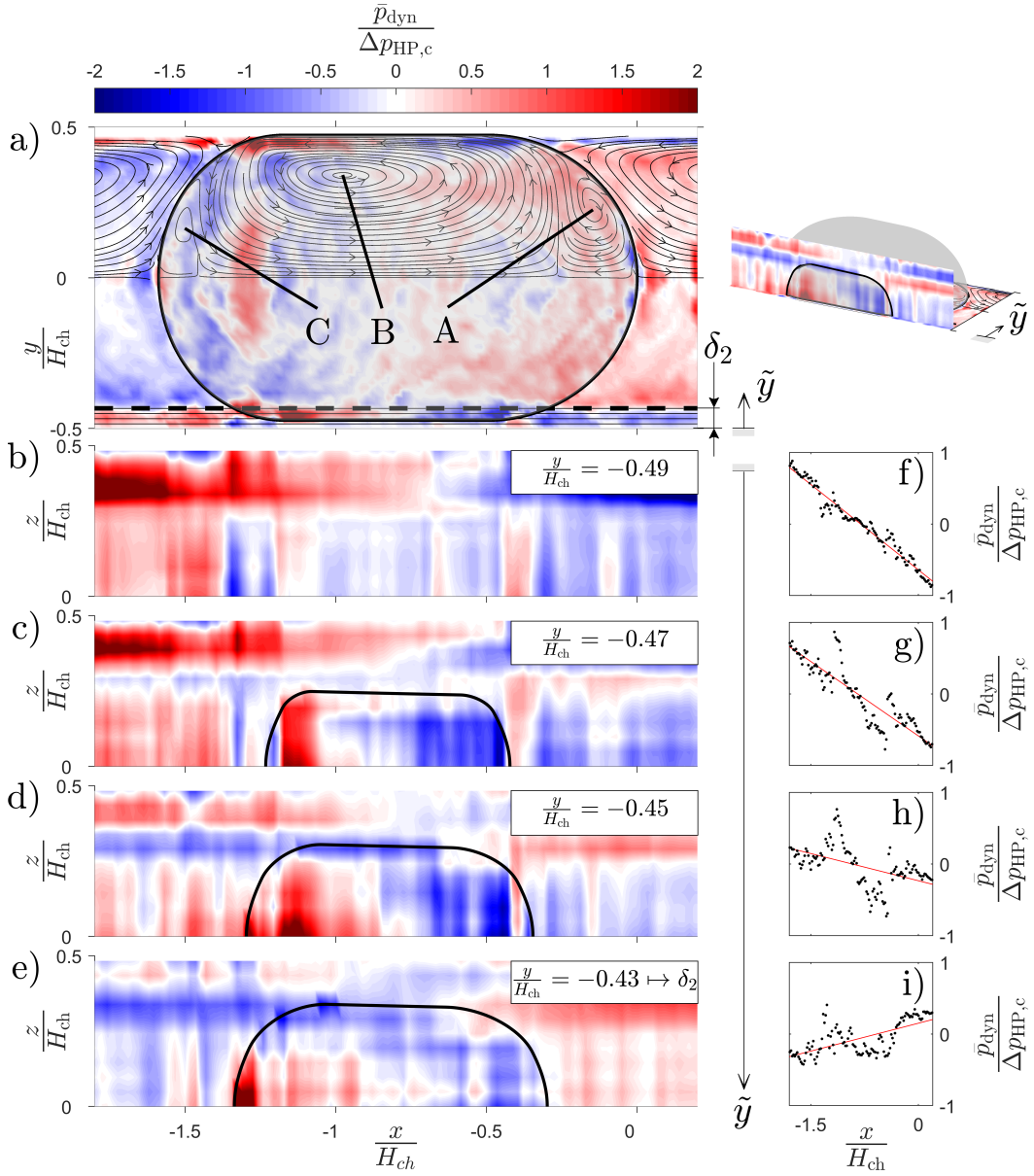

Fig. 6.4: Pressure in- and outside a moving Taylor droplet. The distribution on the x/y-symmetry plane a) shows an increased pressure in front of the droplet due to viscous displacement in comparison to the droplet rear. This pressure difference drives the flow through the gutter. The curved thick black line shows the position of the interface. The ring-vortices are labeled A, B and C from the droplet front to the back, with B denoting the main wall-driven vortrx and A and C indicating the secondary vortices in the respective droplet caps. The thick dashed line delimits the wall-proximate momentum-layer at δ_2. The thin black lines indicate the location of perpendicular pressure field sections (b-e) inside the wall-layer. The diagrams on the right (f-i) show the mean pressure along the x-axis of the according pressure field section. The linear fits (solid red lines) show a change of pressure gradient (slope) towards an inverted pressure gradient in the core flow as a function of the wall distance. The inversion of the gradient is reached at a wall distance of about $\tilde{y} = \frac{\delta_2}{H_{\mathrm{ch}}}$.

Inside the core flow, the viscous displacement of the recirculating main ring-vortices give rise to an elevated pressure.

In Fig. 6.5, the consideration of mean pressure profiles along the downstream direction provides an overview for the discussion of the pressure. For this purpose, a wall-proximate layer of thickness δ_2 is discriminated from the core of the flow as well as the droplet from the bulk. The color-coding indicates the disperse phase with red and the continuous phase with blue, while the core of the flow is represented with a thick line and the wall-layer with a thin line. The constant contribution of the Laplace-pressure is added to the droplet's pressure profiles to visualize the pressure jump at the interface.

Inside the wall-layer of both phases (Fig. 6.5, thin lines) the mean pressure decreases as expected in downstream direction. The elevated droplet viscosity $\lambda = \eta_\mathrm{d}/\eta_\mathrm{c} = 2.625$ causes a higher pressure drop in the momentum layer of the droplet in comparison to the layer of the continuous phase.

In the core flow of the droplet, a clear reversed pressure gradient is present in either phase (Fig. 6.5, thick lines). An expected maximum of the pressure is found at the rear stagnation point of the droplet (red thick line). The pressure fluctuation induced by the rear secondary vortex is followed by an almost linear pressure increase. The pressure fluctuations of the frontal secondary ring-vortex end in a local minimum at the frontal singularity of the droplet.

The evolution of the mean pressure in the core flow of the continuous phase (Fig. 6.5 thick blue line) along the droplet also shows the reversed pressure gradient. Most of the profile is almost constant from the back to the front of the droplet. The reversed pressure increase that drives gutter flow is located between the frontal gutter entrance and the frontal onset of the wall-film. Further downstream, the pressure is almost constant again. This again confirms the postulated pressure gradient inversion with respect to the flow direction by Abiev [3].

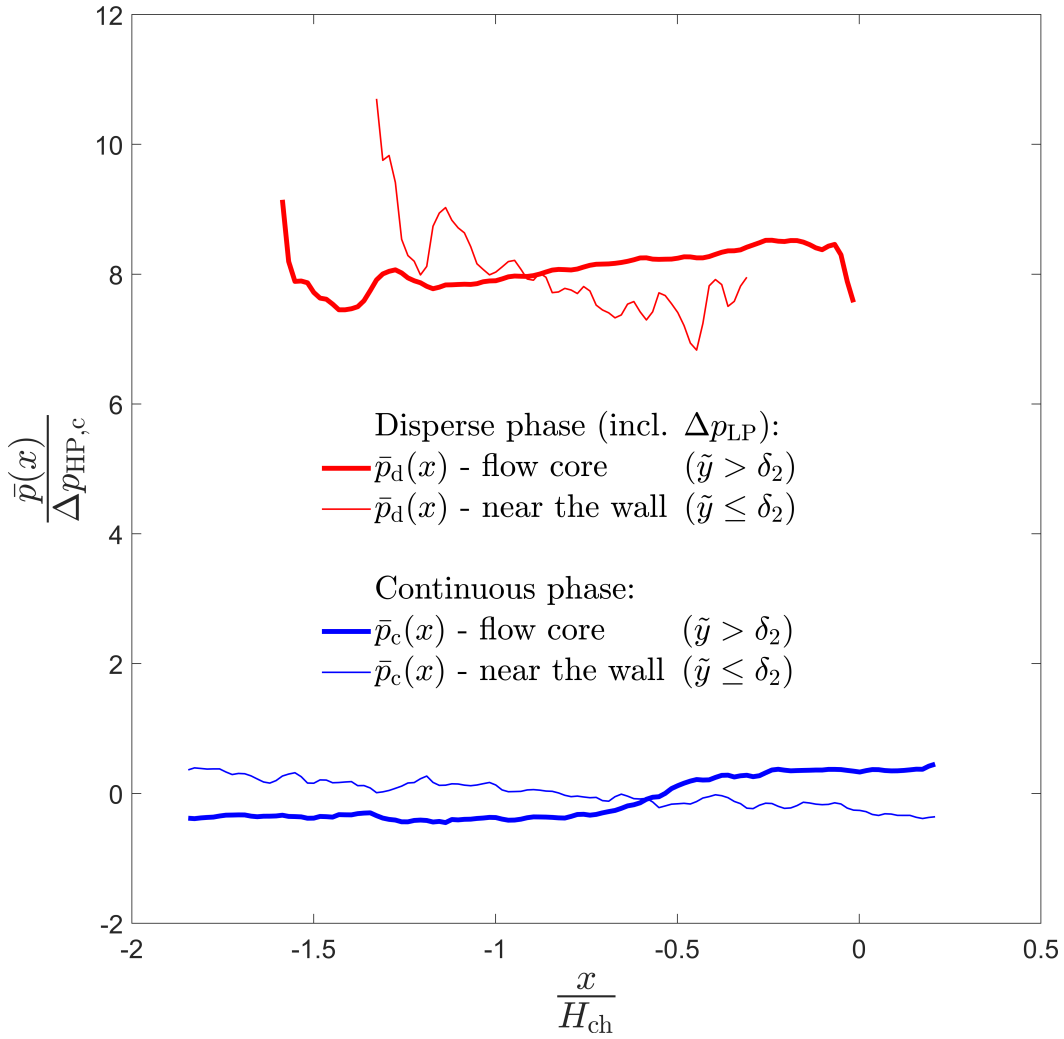

Fig. 6.5: Mean pressure profile evolution along x-axis of a moving Taylor droplet including the Laplace-pressure jump. The pressure inside (red lines) and outside (blue lines) of the droplet is divided into wall-proximate region (thin lines) and the core of the two-phase flow (thick lines). The flow is oriented in the positive x-direction. Inside a wall distance of $\tilde{y} \leqslant \delta_2$, an expected pressure gradient can be observed: the pressure decreases from the droplet back to its front (thin lines). However, viscous displacement in the core of the flow (thick lines) causes an inversion of the pressure gradient from front to back [3]. The inversion drives the bypass flow of the continuous phase from the droplet front to the back and is the cause of the relative velocity of the Taylor droplet [41].

6.5 3D distribution of work done on the flow

The distribution of the work done on the flow allows to locate the major contributions to the energy loss of the flow. For visualization reasons, the distribution of the work done $\mathcal{W}^*$ is scaled with the number of sampling points $\Pi_i N_i$ of the velocity field (Fig. 6.6). The droplet moves in the positive x-direction.

The work distribution in the central symmetry plane is shown in Fig. 6.6a. The interface shape is indicated with a thick black line. The streamlines relate the flow field to the distribution of work done on the flow.

Deceleration work (blue) is mainly performed due to the directional change of downstream velocity component of the flow field. Consequentially, the peak deceleration is located at the annular stagnation regions, where the fluid of the main vortices is forced to reverse direction.

Acceleration work is performed (red) in the caps of the Taylor droplet and inside the wall-influenced layer δ_2. The counter rotating secondary vortices (A, C) in the caps are driven by and receive their energy from the adjoining wall-induced main vortices. Except for the strong directional change of the main vortices, the fluid close to the wall is accelerated due to the no-slip condition at the wall. The layer-thickness of apparent acceleration amounts roughly to δ_2 and coincides with the momentum layer thickness where also the wall-related pressure gradient is situated (Fig. 6.4a).

Inside this layer, wall-proximate sections through the field of work are presented in Fig. 6.6b-e. It is noteworthy that in transverse direction the acceleration regions are spread mainly over the width of the wall-film of the Taylor droplet. With increasing wall distance $\tilde{y}$ the deceleration of the flow grows where the droplet interface redirects the flow.

The respective z-averaged profiles of work done on the flow $\mathcal{W}^*$ along the flow direction are given in Fig. 6.6f-i. Moving step-wise inwards from the wall, the acceleration intensity increases between f-g, and decreases when reaching δ_2 (Fig. 6.6i). In the case of this experiment, the momentum layer thickness δ_2 is a valid measure to distinguish the wall-proximate flow from the core of the Taylor flow.

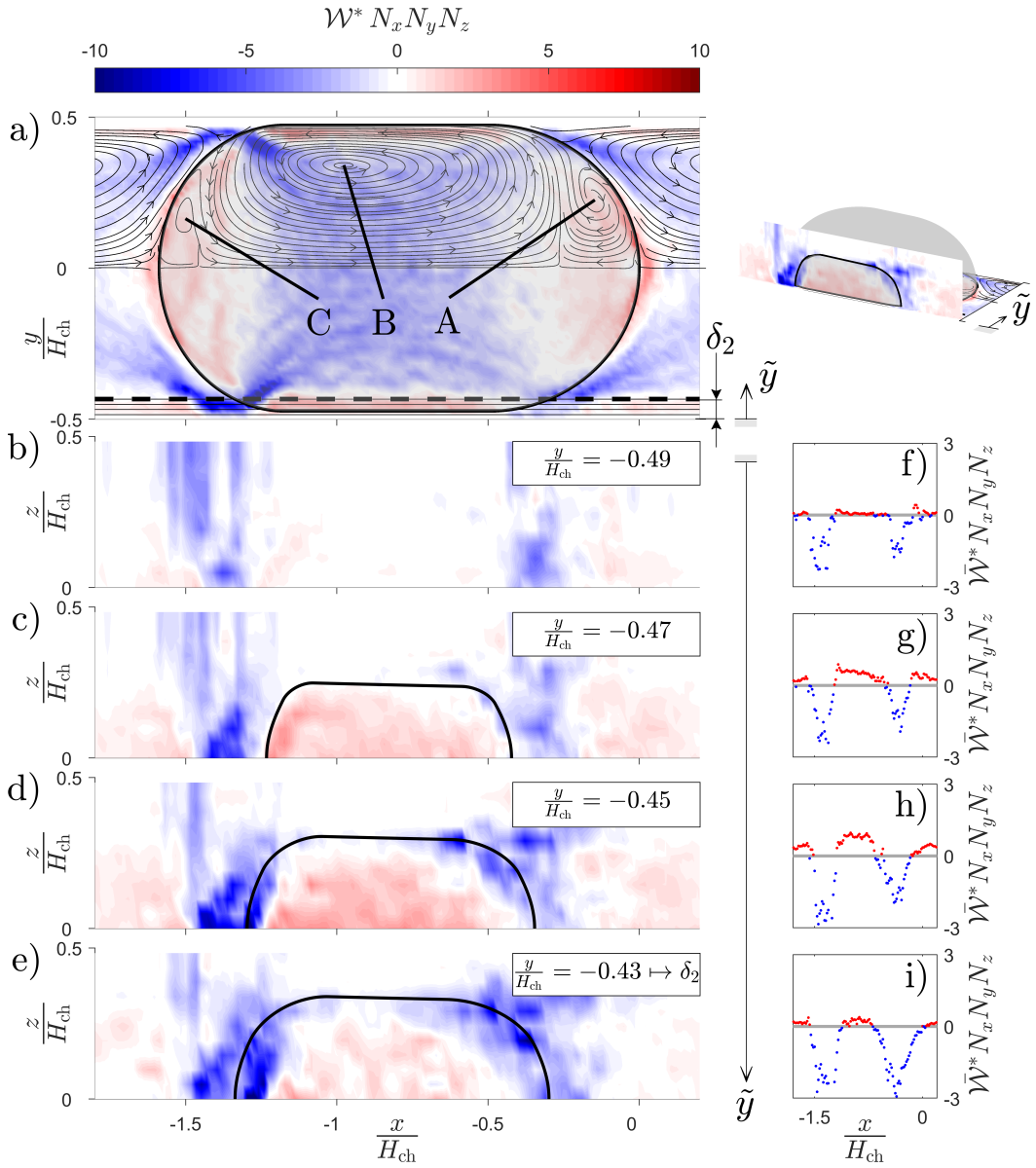

Fig. 6.6: Work done on the flow in- and outside a moving Taylor droplet. The color-coding uses red to show work done for acceleration and blue for the deceleration of fluid. The curved thick black line represents the droplet interface. The distribution of work in the flow field of a moving Taylor droplet on the x/y-symmetry plane a) shows that the secondary vortices (A, C) inside the caps are mainly accelerated by the flow, while the center of the main vortex B is constantly decelerated. The fluid close to the wall is mainly accelerated since the wall-shear impact on the steadily moving Taylor droplet needs to be compensated for. The thick dashed line delimits the wall-proximate momentum layer δ_2. The wall-shear-related acceleration is situated inside the wall layer δ_2 at the wall (b-e). The thin black lines show the location of perpendicular work distribution sections near the wall ($\tilde{y} \leqslant \frac{\delta_2}{H_{ch}}$). The diagrams on the right (f-i) show the mean work distribution along the x-axis of the according sections of the field. The mean work done to accelerate the fluid increases at first with growing wall distance and decreases again towards a wall distance of δ_2

6.6 Energy dissipation of a Taylor droplet

The cumulated energy dissipation of a Taylor droplet is shown and discussed, which is in its dimensionless form equivalent to the overall pressure drop of the Taylor droplet (Eq. 2.16). Thus, the cumulated work done on the flow is quantified, because the energy loss of a Taylor flow due to viscous dissipation equals the work done on the flow to maintain the flow stationary.

Since indirect and derived data on the loss of energy is provided, the results of three different methods are applied and compared. These calculations are based on i) the resistance forces at the interface of the droplet and the microchannel wall $\mathcal{W}_F^*$, ii) the actual work done on the flow field $\mathcal{W}_u^*$ and iii) the pressure loss at the channel wall $\mathcal{W}_{\Delta p,\mathrm{wall}}^*$. As reference quantity, the work done on a comparable single-phase flow is used $\mathcal{W}_{\mathrm{ref}}$ (Eq. 2.14). The discussion of the results always begins at the tip of the rear cap ($x/H_{\mathrm{ch}} = -L_d/H_{\mathrm{ch}} = -1.58$) and proceeds in flow direction (positive x-direction).

i) The cumulated work that is necessary to overcome the resistance forces at the interfaces is given in Fig. 6.7. The thin gray and black lines represent the work done on the gutter and the wall-film of the Taylor droplet interface Γ (Fig. 2.2) respectively. A summation of the latter results the red line, which shows the force-related total work done on the droplet interface displacement. Only those parts of the interface that are parallel to the flow direction contribute to the force-related flow resistance. The actual gutter and wall-film do not contribute. The forces at the front and back caps provide the main resistance, which agrees with the observations and findings of Bretherton [15], who related the interface forces to the pressure drop. The blue line shows the contribution of the cumulated shear forces at the wall that needs to be overcome by the flow. The shear-related work done $\mathcal{W}_{F,\tau}^*$ shows an almost linear contribution to the resistance along the entire droplet. The influence of the entrances and exits of the wall-films slightly raise the otherwise steady increase. The force contributions of the channel wall and the droplet interface show an almost equal magnitude at the front tip of the droplet. A combination of the influence of all force-related work results in the thick black line. At the tip of the front cap,

the resistance forces require $\mathcal{W}_F^*(x/H_{\mathrm{ch}} = 0) = 1.114$ times the work done on the reference single-phase flow.

ii) Fig. 6.8 shows the cumulated work done on the considered flow field (Eq. 2.19). The total work is given by the thick black line. The almost linear increase of the cumulated work along the Taylor droplet results in a magnitude of $\mathcal{W}_u^*(x/H_{\mathrm{ch}} = 0) = 1.458$ at the droplet tip. The contributions are presented differentiating between disperse phase and continuous phase (red and blue) as well as between the wall-layer δ_2 and the core of the flow (thin and thick lines). The work done on the wall proximate layer of the disperse and continuous phase accounts for 2.7% and 5.9% of the total flow related work $\mathcal{W}_u^*$, respectively. Thus, the major contributor for the energy loss is the core of the flow with 91.4%. At $\frac{x}{H_{ch}} = 0$, the dissipation contribution from the core of the disperse phase (thick blue line) amounts to 67.3% of the total work done on the flow (black line). The according contribution from the core of the disperse phase amounts to 24.3% of the total work done on the flow. The ratio of 2.77 between the work done contributed from the core flows corresponds remarkably well to the viscosity ratio $\lambda = 2.625$. The finding that the droplet contributes less with the cap recirculation, while the continuous phase adds the major amount of work at the caps, is mainly attributed to the changed cross-section area ratio in the droplet.

iii) A comparison between three approaches to calculate the total energy loss (Eq. 2.17-2.19) along the flow direction is presented in Fig. 6.9. The work received from the 3D flow field is given by the thick black line. The thick gray line indicates the shear and drag forces-based work at the channel walls and the droplet interface. Gray dots show a wall pressure-based approach to calculate the energy loss (Sec. 2.4.7b). As a first order simplification a linear fit (dashed line) allows to determine the total energy loss. The light gray area indicates $\pm 10\%$ deviation from the linear fit.

Judged from the total energy loss at the front tip of the Taylor droplet ($x/H_{\mathrm{ch}} = 0$), the drag and shear forces alone deliver the lowest estimate of the energy loss $\mathcal{W}_F^* = 1.11 = 0.76\mathcal{W}_u^*$. The linearized wall-pressure based approach estimates $\mathcal{W}_{\Delta p,\mathrm{wall}}^* = 1.25 = 0.86\mathcal{W}_u^*$ performs better.

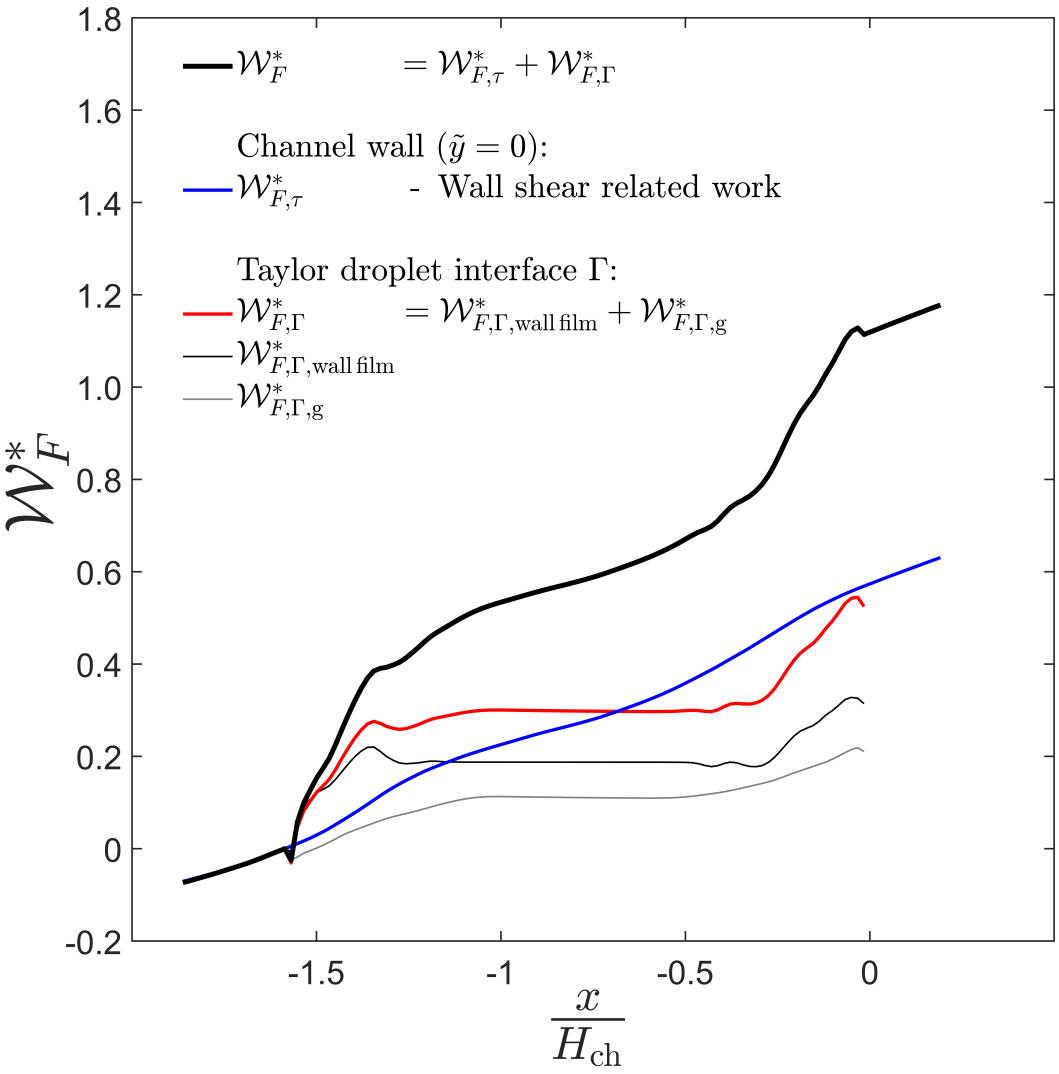

Fig. 6.7: Accumulated work due to drag forces from the onset of the rear cap (x/H_{ch} = -1.58) towards the droplet front (x/H_{ch} = 0). The accumulated forces along the gutter regions (thin light gray line) contribute less drag than the film regions (gray line). The addition of the interface forces of the gutters to those of the films results the drag force evolution along the moving Taylor droplet (red line). The shear forces at the channel walls (blue line) also contribute to the energy loss of the Taylor flow. The addition of the interfacial forces and the wall-shear forces gives the overall drag force profile in flow direction (thick black line). In total, wall-shear forces and interface forces contribute almost evenly. While the shear forces exhibit a steady increase along the droplet, the contribution of the interface is mainly attributed to the cap regions

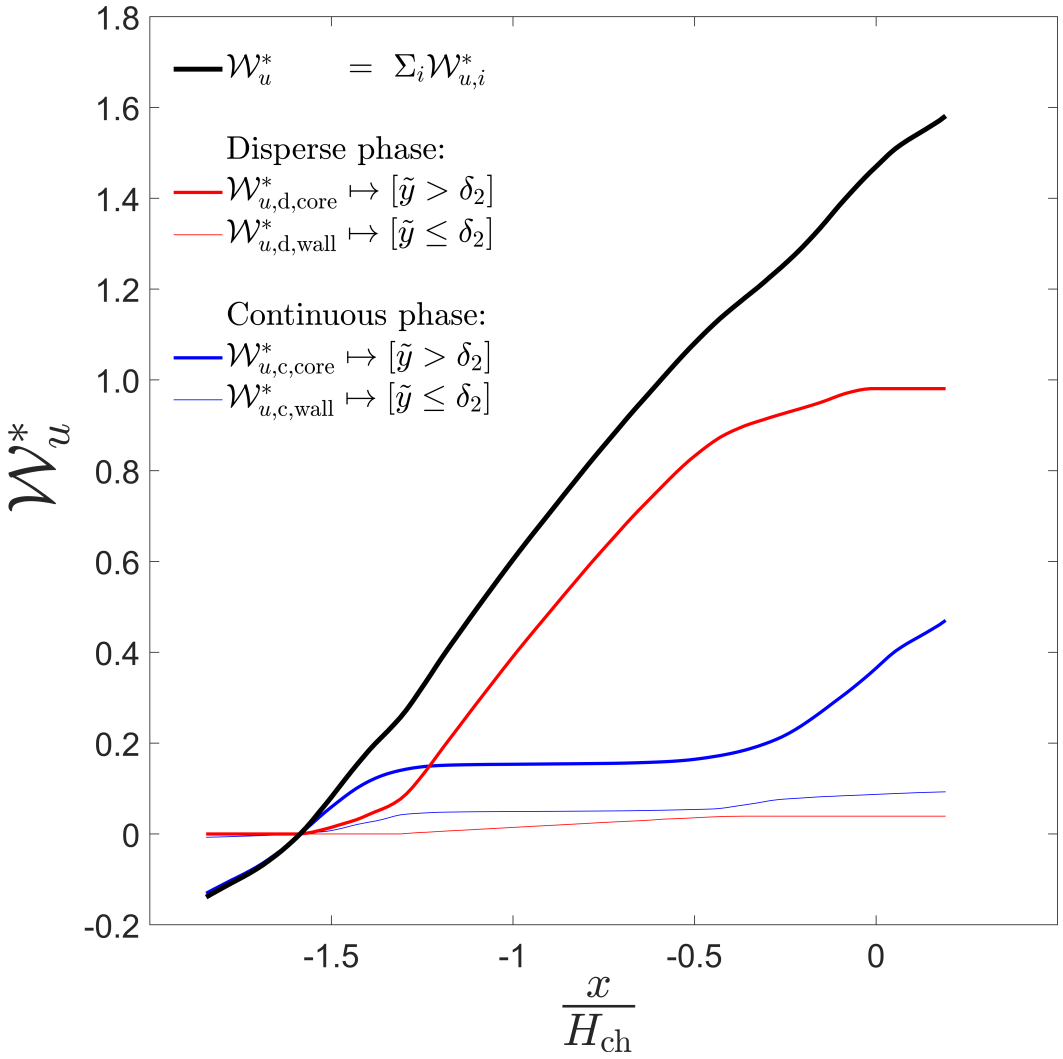

Fig. 6.8: Accumulated absolute work from the onset of the rear cap (x/H_{ch} = -1,58) towards the droplet front (x/H_{ch} = 0). The flow is oriented in the positive x-direction. The absolute work done inside (red lines) and outside (blue lines) the droplet is divided into wall-proximate region (thin lines) and the core of the two-phase flow (thick lines). The sum of all contributions results the total work done (thick black line) that is necessary to sustain the stationary two-phase flow

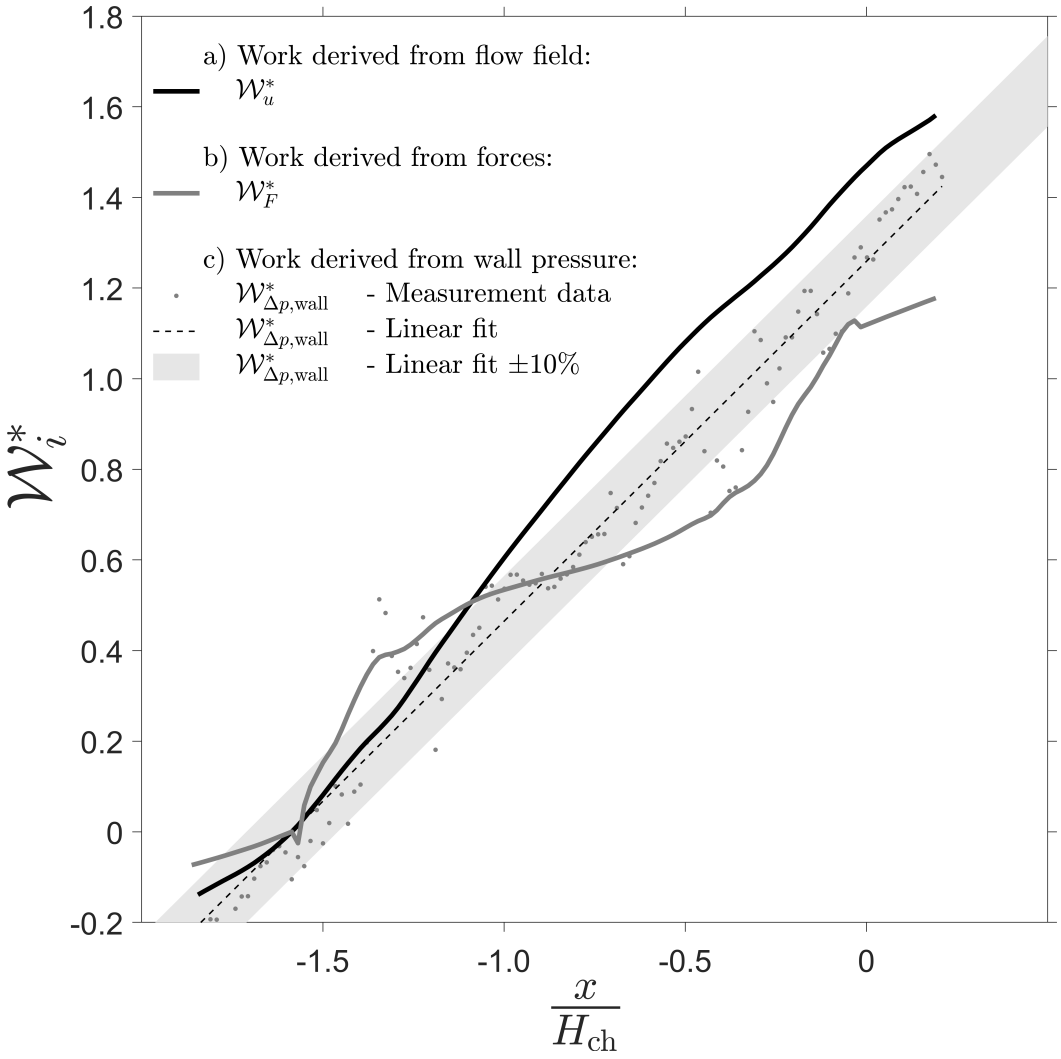

Fig. 6.9: Comparison between different dimensionless indicators of the work: The cumulated work derived from flow field a) is compared to the shear and drag forces at the channel walls and the droplet interface b) and the work estimated from the pressure profile at the wall c). All quantities are referenced with the work of a Hagen-Poiseuille flow in a square pipe of equal cross section A_{ch} and channel length $L_{\mathrm{ch}} = L_{\mathrm{d}}$. The reference channel is filled with the continuous phase of the Taylor flow and experiences the volume flow of $Q_{\mathrm{ref}} = Q_{\mathrm{tot}} = (Q_{\mathrm{d}} + Q_{\mathrm{c}})$ of the Taylor flow

The cumulated work done on the flow $\mathcal{W}_u^*$ amounts to 1.471 times the work done on the reference case of the single-phase flow in a square channel.

All presented approaches to quantify the energy dissipation of the two-phase flow are derivations of high order. They indirectly depend on the reconstructed 3D flow field to a variable degree: While pressure-based work $\mathcal{W}_{\Delta p,\mathrm{wall}}^*$ involves double differentiation and an integration, the interface force-related work $\mathcal{W}_F^*$ is subject to additional conversion and integration steps. Since the work done on the flow $\mathcal{W}_u^*$ includes only double derivatives, the result is considered to be more reliable. From this perspective, the tendency towards lower magnitudes of total work done on the Taylor flow correlates with a decreasing accuracy due to the indirectness of the quantification approaches. In addition, the force-based approach $\mathcal{W}_F^*$ does solely include forces in flow direction and omits contributions of the transverse flow.

6.7 Conclusion

For the first time the pressure field of a moving Taylor droplet has been extracted based upon experimental work. Despite the approximate character of the interface representation [82] (Chap. 4) and the mentionable noise level of the processed experimental data [83] (Chap. 5), a coherent overall picture of the 3D pressure field in and around a moving Taylor droplet is established.

The distinction between a wall-proximate momentum layer of thickness δ_2 and a core flow reveals a reversal of the pressure gradient from the wall towards the center of the flow. In the wall-proximate momentum layer, the pressure decreases in flow direction as one would expect from a pressure-driven laminar single-phase flow. However, the pressure gradient reverses when reaching the core of the flow. Here, the flow is governed by viscous displacement and builds up a pressure gradient from the droplet front to its back. Thus, the expectation of a reversed pressure gradient as stated by Abiev [3] is confirmed.

A straightforward estimation method is experimentally verified to quantify the reversed pressure gradient that drives the bypass flow of the continuous phase through the gutters and causes the relative velocity of Taylor droplets [41]. The approach overestimates the measured driving pressure gradient by 2.7%.

The curvature-based Laplace-pressure distribution on the droplet interface is deduced from the interface approximation [82] (Chap. 4). It resembles the measurement-based pressure distribution on the droplet interface only qualitatively. Thus, the interface approximation does not allow a precise calculation of second order information like the curvature distribution. However, it delivers accurate first order information, e.g. the location, the volume and the surface area of dynamically deformed Taylor droplet interface.

The 3D distribution of work done on the flow is divided into acceleration and deceleration. The fluid inside the wall-proximate momentum layer at the wall-films and inside the droplet caps is mainly accelerated, while the remaining flow undergoes deceleration. The constant change for the circulating liquid between acceleration and deceleration causes additional energy loss in comparison to the laminar flow in a straight pipe.

As a measure for the overall energy loss of the moving droplet the drag forces at the droplet and channel interface are compared to the cumulative work done on the flow field to overcome internal friction. The comparison shows that a consideration of the drag forces alone does not deliver all information on the losses of the flow. The governing viscous forces that act inside and outside the Taylor droplet also contribute to the overall energy loss. The energy loss calculated from the work done on the flow is 31.6% higher than the result received from the approach based on the drag-forces.

The 3D pressure field and the distribution of work done on the investigated Taylor flow enables benchmarking for numerical simulations and is published as supplementary material.

7

Main conclusions and outlook

Once there were some particles
Whose turns seemed random - farcical
Dark long nights were measured through
Next Evaluation - than review
Now their moves fill articles

This chapter summarizes the main findings of the Chapters 4-6 and provides an overview on the achievements of the work described in this thesis. The order of the presented content is preserved with respect to its presentation in the respective chapters. Secondly, an outlook is given on the possibilities that open future research.

Conclusions

In order to provide a model-based guidance for multiplane μPIV-measurements of the 3D flow field of Taylor flows in rectangular micro channels, **an analytic interface shape approximation** for low capillary numbers is proposed (Chap. 4). Based on the flow-dependent droplet dimensions in the droplet symmetry plane an elliptical shape deformation is assumed. Given the dynamic front and back cap deformation ratios (Eq. 4.3), the droplet length and the channel aspect ratio, the mean front and back gutter radii (Eq. 4.7) can now be determined.

Geometric boundary conditions are defined to calculate a 3D-distribution of interface nodes (Sec. 4.3). The proposed model can be applied for rectangular channels of varying aspect ratio $A_\mathrm{r} = \frac{W_\mathrm{ch}}{H_\mathrm{ch}} = [1...2]$ (and possibly beyond) and dimensionless Taylor droplet length $\frac{L_\mathrm{d}}{W_\mathrm{ch}} \gtrsim 1$. The capillary numbers covered by the analytical approximation are set in a range that is suitable not only for applications but also for theoretical work on microscopic Taylor flow. In terms of Reynolds numbers, the approximation is restricted to flows dominated by viscous forces, since the modeled deformation at the back of the droplet begins to deviate beyond the onset of inertia forces [64].

This approximation is the first work that delivers an approach to analytically asses the dynamically deformed shape of a moving Taylor droplet and the dimensions of the curved interface radii at the gutter (Sec. 6.3). The Laplace pressure difference between the gutter entrances over the distance of the gutter length allows to estimate the pressure gradient of the bypass flow through the gutters. The latter evokes the excess velocity between the droplet velocity and the mean velocity of the entire flow. The gradient estimation for the bypass flow through the gutters is valid for the range of $Ca_\mathrm{c} \lesssim 0.02$ and $Re_\mathrm{c} \lesssim 10$. Beyond those force ratios the flow ripples the interface shape at the onset of droplet back cap and the description wall film thickness looses validity. Additionally, the interface approximation can be used to visualize and investigate flow quantities (e.g. velocity, pressure) directly at the interface.

The **evaluation methods**, which have been developed for this work, generally allow to investigate laminar quasi-stationary and pulsating flows (Sec. 3.3). The methodology to asynchronously record, extract (raw image preprocessing) and compile (image shift for the in- and out-of-plane alignment) raw images of a two-phase flow that is subjected to stability fluctuations is essential to the successful quantitative analysis of the reconstructed 3D3C velocity field of inside and outside of moving Taylor droplets. An important part is the statistical analysis of the apparent droplet length distribution (Fig. 3.4) on all measurement planes to maximize the amount of flow information and to minimize the overall influence of the droplet length fluctuation. This procedure is the key-method that enables the successful accurate extraction of 3D3C velocity field from conventional multiplane 2D2C μPIV experiments investigating fluctuating Taylor flows.

The **μPIV study on the 3D2C velocity distribution of Taylor droplets** allows to reconstruct third velocity component (Sec. 3.5). It establishes a qualitatively and quantitatively verified 3D3C velocity field of a mean Taylor droplet and investigates the 3D flow features (Chap. 5). For the first time, an experimental data set allows to visualize the streamlines of the velocity distribution on the interface of a Taylor droplet (Fig. 5.3) and to directly relate it to the main and secondary vortices of the velocity field (Fig. 5.6).

Determining the shear rate distribution helps to effectively handle fragile educts or products in single phase as well as in multiphase microfluidic flows, e.g. organ-on-a-chip applications and cell handling applications using droplets [24]. The maximum shear rate is located in the continuous phase at the entrances and exits of the wall films and the corner flow (gutter) bypassing the Taylor droplet (Fig. 5.6). Thus, shear sensitive educts or products need to be placed inside the droplet if possible.

For the first time **the pressure field of a moving Taylor droplet** has been extracted based on experimental work. Despite the approximate character of the interface representation and the mentionable noise level of the processed experimental data, a coherent overall picture of the 3D pressure field in and around a moving Taylor droplet is established (Chap. 6).

The distinction between the momentum layer of thickness δ_2 and a core flow that is governed by viscous displacement (Sec. 2.4.1) reveals a pressure gradient reversal from the wall towards the center (Fig. 6.4). At the wall the pressure decreases as expected in the flow direction, while in the core of the flow it is directed against the flow direction. Thus, the analytical prediction of a reversed pressure gradient in the gutter as stated by Abiev [3] is confirmed.

A straightforward estimation method is verified (Fig. 6.3) to quantify the pressure gradient that drives the bypass flow of continuous phase through the gutters and gives rise to the excess velocity of Taylor droplets [40]: The Laplace pressure difference received from the mean gutter radius difference between the droplet front and its back. The approach slightly overestimates the measured driving pressure gradient by 2.7%.

The 3D scalar field of work done on the flow is divided into acceleration and deceleration work (Fig. 6.6). The fluid inside the momentum layer

at the wall films and inside the droplet caps is mainly accelerated, while the remaining flow undergoes deceleration. The constant change for the circulating liquid between acceleration and deceleration causes additional energy loss in comparison to the laminar flow in a straight pipe.

As a measure for the overall energy loss of the moving droplet, a comparison of the cumulative forces at the droplet and channel interface with the cumulative work done in the flow field (Sec. 6.6) shows that a consideration of forces does not result in the complete information on the flow losses. The governing viscous forces that act inside and outside the Taylor droplet contribute significantly to the overall energy loss.

Despite mainly referencing a single flow situation ($Ca = 0.005, Re = 0.051$), this thesis provides an extensive and detailed insight into the physics of the viscous Taylor flow. Especially, since it is being based on experimental work, it provides a unique spatially well-resolved reference case to benchmark numerical parameter studies on digital microfluidics.

Outlook

The application of Taylor droplets e.g. in chemical processes to achieve process intensification necessitates stable process conditions at an optimal working point. Fluctuations of any kind are therefore depreciated in this context. The fluctuations of a Taylor droplet chain in a long microchannel express themselves as a velocity distribution, a droplet length distribution, and a droplet shedding frequency distribution.

The reason for the droplet velocity distribution in Taylor flows differs from that of freely moving consecutive droplets: Disregarding possible buoyancy differences between the freely rising droplets due to a size distribution, a preceding droplet wake increases the velocity of a following droplet. In contrast, the bounding walls of the microchannel enforce similar hydrodynamic conditions for the individual droplets of the Taylor flow.

The droplet parameters velocity, length and time (frequency) are interdependent. They ultimately result from a feedback mechanism between i) the pressure conditions at the flow-focusing-junction (the driving pressure of

the two phases and the Laplace pressure across their interface) and ii) the overall pressure loss in the channel on the generation of new droplets.

In order to gain control of the velocity distribution of a Taylor flow that exhibits a droplet length distribution, the excess velocity of individual Taylor droplets needs to be controlled. The flow could be manipulated such, that all droplets translate with the same droplet velocity (i.e. with the total superficial velocity of the flow). It is not possible to prevent the Taylor flow from inducing the viscous displacement at the droplet front cap that builds up the driving pressure gradient of the bypass flow towards the droplet back. However, the flow conditions in the gutter are available to minimize the volume flow through the bypass. The hydraulic transmittance of the gutter can be influenced by the surface mobility of the droplet interface, the cross-sectional area of the gutter, the length of the gutter (related to the droplet length) and the viscosity of the continuous phase. A parameter study could be performed to clearly isolate the influences of

- the microchannel aspect ratio,
- the droplet length,
- the viscosity ratio between the involved phases, and
- a possible influence of a rising momentum transfer from the bulk phase into the droplets at elevated Re_c.

The prevention of a droplet length distribution would be more desirable, since it is the length fluctuation itself that causes the velocity distribution over the Taylor droplet chain. In order to gain insight into the formation of a Taylor droplet at flow-focusing-junctions a phase averaged high-speed 3D3C μPIV study of the Taylor droplet formation would allow to investigate the physics in detail.

From a process point of view it is important to investigate how the convection conditions change with respect to the application of physiological fluids (e.g. blood, blood plasma, protein samples). The assumption of a Newtonian fluid behavior often fails with the latter. Shear thinning behavior could have a significant effect on the relative flow through the gutters and with that on the excess velocity between the droplet and the mean velocity of the

flow. In order to maintain optimal process conditions it is favorable to gain knowledge and control on these effects.

Bibliography

[1]T. Abadie, J. Aubin, D. Legendre, and C. Xuereb. “Hydrodynamics of gas–liquid Taylor flow in rectangular microchannels”. In: *Microfluidics and Nanofluidics* 12.1 (Jan. 2012), pp. 355–369 (cit. on pp. 14, 56).

[2]A. R. Abate, P. Mary, V. van Steijn, and D. A. Weitz. “Experimental validation of plugging during drop formation in a T-junction”. In: *Lab Chip* 12 (8 2012), pp. 1516–1521 (cit. on pp. 52, 103).

[3]R. Sh. Abiev. “Analysis of local pressure gradient inversion and form of bubbles in Taylor flow in microchannels”. In: *Chemical Engineering Science* 174 (2017), pp. 403–412 (cit. on pp. 7, 8, 103, 105, 107, 110, 113, 115, 116, 124, 129).

[4]R. Sh. Abiev. “Modeling of pressure losses for the slug flow of a gas-liquid mixture in mini- and microchannels”. In: *Theoretical Foundations of Chemical Engineering* 45.2 (2011), pp. 156–163 (cit. on p. 103).

[5]R.Sh. Abiev. “Bubbles velocity, Taylor circulation rate and mass transfer model for slug flow in milli- and microchannels”. In: *Chemical Engineering Journal* 227 (2013). IMRET 12: Proceedings of the Twelfth International Conference on Microreaction Technology, pp. 66–79 (cit. on p. 56).

[6]R. J. Adrian and J. Westerweel. *Particle Image Velocimetry*. Cambridge; New York: Cambridge University Press, 2011 (cit. on pp. 44, 45, 47).

[7]N. Anantasarn, D. K. Babi, U. Suriyapraphadilok, and R. Gani. “Phenomena Based Process Intensification of Toluene Methylation for Sustainable Para-xylene Production”. In: *26th European Symposium on Computer Aided Process Engineering*. Ed. by Z. Kravanja and M. Bogataj. Vol. 38. Computer Aided Chemical Engineering. Elsevier, 2016, pp. 1093–1098 (cit. on p. 4).

[8]P. Angeli and A. Gavriilidis. “Hydrodynamics of Taylor flow in small channels: A Review”. In: *Proceedings of the Institution of Mechanical Engineers, Part C: Journal of Mechanical Engineering Science* 222.5 (2008), pp. 737–751 (cit. on p. 14).

[9]S. L. Anna. “Droplets and Bubbles in Microfluidic Devices”. In: *Annual Review of Fluid Mechanics* 48.1 (2016), pp. 285–309 (cit. on p. 56).

[10]N. Antweiler, S. Gatberg, G. Jestel, J. Franzke, and D. W. Agar. “Noninvasive Sensor for the Detection of Process Parameters for Multiphase Slug Flows in Microchannels”. In: *ACS Sensors* 1.9 (2016), pp. 1117–1123 (cit. on p. 102).

[11]G. Balestra, L. Zhu, and F. Gallaire. “Viscous Taylor droplets in axisymmetric and planar tubes: from Bretherton’s theory to empirical models”. In: *Microfluidics and Nanofluidics* 22.6 (June 2018), p. 67 (cit. on pp. 78, 103).

[12]T. Bandara, N.-T. Nguyen, and G. Rosengarten. “Slug flow heat transfer without phase change in microchannels: A review”. In: *Chemical Engineering Science* 126 (2015), pp. 283–295 (cit. on p. 5).

[13]T. Baur. “PIV with high temporal resolution for the determination of local pressure reductions from coherent turbulence phenomena”. In: *Proc. 3rd Int. Workshop on PIV - Santa Barbara*. 1999, pp. 101–106 (cit. on p. 23).

[14]A. Bordbar, A. Taassob, A. Zarnaghsh, and R. Kamali. “Slug flow in microchannels: Numerical simulation and applications”. In: *Journal of Industrial and Engineering Chemistry* 62 (2018), pp. 26–39 (cit. on p. 83).

[15]F. P. Bretherton. “The motion of long bubbles in tubes”. In: *Journal of Fluid Mechanics* 10.2 (1961), pp. 166–188 (cit. on pp. 2, 14, 103, 119).

[16]Ch. Brücker. “3D scanning PIV applied to an air flow in a motored engine using digital high-speed video”. In: *Measurement Science and Technology* 8.12 (Dec. 1997), pp. 1480–1492 (cit. on pp. 9, 47).

[17]Ch. Brücker. “Digital-Particle-Image-Velocimetry (DPIV) in a scanning light-sheet: 3D starting flow around a short cylinder”. In: *Experiments in Fluids* 19.4 (Aug. 1995), pp. 255–263 (cit. on pp. 9, 47).

[18]H. Bruus. *Theoretical Microfluidics*. New York: Oxford University Press, 2008 (cit. on p. 2).

[19]R. Budwig. “Refractive index matching methods for liquid flow investigations”. In: *Experiments in Fluids* 17.5 (Sept. 1994), pp. 350–355 (cit. on p. 35).

[20]Z. Cai, Y. Liu, T. Chen, and T. Liu. “Variational method for determining pressure from velocity in two dimensions”. In: *Experiments in Fluids* 61.5 (Apr. 2020), p. 118 (cit. on p. 23).

[21]J. J. Charonko, C. V. King, B. L. Smith, and P. P. Vlachos. “Assessment of pressure field calculations from particle image velocimetry measurements”. In: *Measurement Science and Technology* 21.10 (Aug. 2010), p. 105401 (cit. on pp. 23, 24).

[22]W. Chou, P. Lee, C. Yang, W. Huang, and Y. Lin. “Recent Advances in Applications of Droplet Microfluidics”. In: *Micromachines* 6.9 (2015), pp. 1249–1271 (cit. on pp. 5, 56).

[24]P. Cui and S. Wang. “Application of microfluidic chip technology in pharmaceutical analysis: A review”. In: *Journal of Pharmaceutical Analysis* 9.4 (2019). Special Issue: Advances in Pharmaceutical Analysis 2018, pp. 238–247 (cit. on pp. 99, 129).

[25]A. A. Darhuber and S. M. Troian. “Principles of microfluidic actuation by modulation of surface stresses”. In: *Annual Review of Fluid Mechanics* 37.1 (2005), pp. 425–455 (cit. on p. 56).

[26]E. Delnoij, J. Westerweel, N.G. Deen, J.A.M. Kuipers, and W.P.M. van Swaaij. “Ensemble correlation PIV applied to bubble plumes rising in a bubble column”. In: *Chemical Engineering Science* 54.21 (1999), pp. 5159–5171 (cit. on p. 44).

[27]F. Fairbrother and A. E. Stubbs. “119. Studies in electro-endosmosis. Part VI. The ’bubble-tube’ method of measurement”. In: *Journal of the Chemical Society* (), pp. 527–529 (cit. on p. 2).

[28]C. J. Falconi, C. Lehrenfeld, H. Marschall, et al. “Numerical and experimental analysis of local flow phenomena in laminar Taylor flow in a square minichannel”. In: *Physics of Fluids* 28.1 (2016), p. 012109 (cit. on p. 83).

[29]R. Feynman. *There is plenty of room at the bottom*. Annual meeting of the American Physical Society. Dec. 1959 (cit. on p. 2).

[30]P. Garstecki, M. J. Fuerstman, M. A. Fischbach, S. K. Sia, and G. M. Whitesides. “Mixing with bubbles: a practical technology for use with portable microfluidic devices”. In: *Lab Chip* 6 (2 2006), pp. 207–212 (cit. on p. 5).

[31]T. Gervais, J. El-Ali, A. Günther, and K. F. Jensen. “Flow-induced deformation of shallow microfluidic channels”. In: *Lab Chip* 6 (4 2006), pp. 500–507 (cit. on p. 52).

[32]T. Glawdel and C. L. Ren. “Global network design for robust operation of microfluidic droplet generators with pressure-driven flow”. In: *Microfluidics and Nanofluidics* 13.3 (Sept. 2012), pp. 469–480 (cit. on p. 3).

[33]I. E. Grossmann and A. W. Westerberg. “Research challenges in process systems engineering”. In: *AIChE Journal* 46.9 (2000), pp. 1700–1703 (cit. on p. 4).

[34]S. Guido and V. Preziosi. “Droplet deformation under confined Poiseuille flow”. In: *Advances in Colloid and Interface Science* 161.1 (2010). Physico-chemical and flow behaviour of droplet based systems, pp. 89–101 (cit. on p. 83).

[35]A. Gunther, S. A. Khan, M. Thalmann, F. Trachsel, and K. F. Jensen. “Transport and reaction in microscale segmented gas-liquid flow”. In: *Lab Chip* 4 (4 2004), pp. 278–286 (cit. on pp. 5, 56).

[36]R. Gurka, A. Liberzon, D. Hefetz, D. Rubinstein, and U Shavit. “Computation of Pressure Distribution Using PIV Velocity Data”. In: *Proc. 3rd Int. Workshop on PIV - Santa Barbara*. Jan. 1999 (cit. on p. 22).

[37]Y. Han and N. Shikazono. “Measurement of liquid film thickness in micro square channel”. In: *International Journal of Multiphase Flow* 35.10 (2009), pp. 896–903 (cit. on pp. 57, 62, 71).

[38]A. L. Hazel and M. Heil. “The steady propagation of a semi-infinite bubble into a tube of elliptical or rectangular cross-section”. In: *Journal of Fluid Mechanics* 470 (2002), pp. 91–114 (cit. on p. 83).

[39]T. Helmers, P. Kemper, U. Mießner, and J. Thöming. “Refractive index matching (RIM) using double-binary liquid-liquid mixtures”. In: *Experiments in Fluids* 61.2 (Feb. 2020), p. 64 (cit. on p. 8).

[40]T. Helmers, P. Kemper, J. Thöming, and U. Mießner. “Determining the flow-related cap deformation of Taylor droplets at low Ca numbers using ensemble-averaged high-speed images”. In: *Experiments in Fluids* 60.7 (June 2019), p. 113 (cit. on pp. 8, 15, 94, 109, 129).

[41]T. Helmers, P. Kemper, J. Thöming, and U. Mießner. “Modeling the excess velocity of low-viscous Taylor droplets in square microchannels”. In: *Fluids* 4.3 (2019) (cit. on pp. 3, 7, 14, 103–105, 110, 111, 116, 125).

[42]T. Helmers, J. Thöming, and U. Mießner. “Retrieving accurate temporal and spatial information about Taylor slug flows from non-invasive NIR photometry measurements”. In: *Experiments in Fluids* 58.11 (Oct. 2017), p. 160 (cit. on p. 71).

[43]J. A. Howard and P. A. Walsh. “Review and extensions to film thickness and relative bubble drift velocity prediction methods in laminar Taylor or slug flows”. In: *International Journal of Multiphase Flow* 55 (2013), pp. 32–42 (cit. on pp. 14, 56).

[44]IPCC Core Writing Team, R. K. Pachauri, and L. A. Meyer (eds.) *Climate Change 2014: Synthesis Report. Contribution of Working Groups I, II and III to the Fifth Assessment Report of the Intergovernmental Panel on Climate Change*. IPCC, Geneva, Switzerland. 2014 (cit. on p. 4).

[45]S. Jakiela. "Measurement of the hydrodynamic resistance of microdroplets". In: *Lab on a chip* 16.19 (2016), pp. 3695–3699 (cit. on p. 104).

[46]S. Jakiela, P. M. Korczyk, S. Makulska, O. Cybulski, and P. Garstecki. "Discontinuous Transition in a Laminar Fluid Flow: A Change of Flow Topology inside a Droplet Moving in a Micron-Size Channel". In: *Phys. Rev. Lett.* 108 (13 Mar. 2012), p. 134501 (cit. on pp. 3, 14).

[47]S. Y. Jaw, J.-H. Chen, and P.-C. Wu. "Measurement of Pressure Distribution from PIV Experiments". In: *Journal of Visualization* 12 (Mar. 2009), pp. 27–35 (cit. on p. 23).

[48]J. Jeong and F. Hussain. "On the identification of a vortex". In: *Journal of Fluid Mechanics* 285 (1995), pp. 69–94 (cit. on pp. 22, 96).

[49]Y. Jin, A. Orth, E. Schonbrun, and K. B. Crozier. "Measuring the pressures across microfluidic droplets with an optical tweezer". In: *Optics express* 20.22 (2012), pp. 24450–24464 (cit. on p. 103).

[50]B. M. Jose and T. Cubaud. "Formation and dynamics of partially wetting droplets in square microchannels". In: *RSC Adv.* 4 (29 2014), pp. 14962–14970 (cit. on p. 7).

[51]J. Jovanović, W. Zhou, E. V. Rebrov, et al. "Liquid–liquid slug flow: Hydrodynamics and pressure drop". In: *Chemical Engineering Science* 66.1 (2011), pp. 42–54 (cit. on p. 103).

[52]S. G. Kandlikar. "Fundamental issues related to flow boiling in minichannels and microchannels". In: *Experimental Thermal and Fluid Science* 26.2 (2002), pp. 389–407 (cit. on pp. 5, 56).

[53]D.-K. Kang, M. M. Ali, K .Zhang, et al. "Rapid detection of single bacteria in unprocessed blood using Integrated Comprehensive Droplet Digital Detection". In: *Nature Communications* 5 (2014), p. 5427 (cit. on p. 5).

[54]R. de Kat and B. W. van Oudheusden. "Instantaneous planar pressure determination from PIV in turbulent flow". In: *Experiments in Fluids* 52.5 (May 2012), pp. 1089–1106 (cit. on pp. 22, 23).

[55]S. Khodaparast, N. Borhani, G. Tagliabue, and J. R. Thome. "A micro particle shadow velocimetry (μPSV) technique to measure flows in microchannels". In: *Experiments in Fluids* 54.2 (Feb. 2013), p. 1474 (cit. on p. 84).

[56]S. Khodaparast, N. Borhani, and J.R. Thome. “Application of micro particle shadow velocimetry μPSV to two-phase flows in microchannels”. In: *International Journal of Multiphase Flow* 62 (2014), pp. 123–133 (cit. on p. 84).

[57]H. Kinoshita, S. Kaneda, T. Fujii, and M. Oshima. “Three-dimensional measurement and visualization of internal flow of a moving droplet using confocal micro-PIV”. In: *Lab Chip* 7 (3 2007), pp. 338–346 (cit. on pp. 8, 83).

[58]N. Kockmann. “Chemical Reactions and Reactive Precipitation”. In: *Transport Phenomena in Micro Process Engineering*. Berlin, Heidelberg: Springer Berlin Heidelberg, 2008, pp. 225–292 (cit. on p. 5).

[59]V. Koschatzky, P. D. Moore, J. Westerweel, F. Scarano, and B. J. Boersma. “High speed PIV applied to aerodynamic noise investigation”. In: *Experiments in Fluids* 50.4 (Apr. 2011), pp. 863–876 (cit. on p. 22).

[60]M. T. Kreutzer, F. Kapteijn, J. A. Moulijn, and J. J. Heiszwolf. “Multiphase monolith reactors: Chemical reaction engineering of segmented flow in microchannels”. In: *Chemical Engineering Science* 60.22 (2005). 7th International Conference on Gas-Liquid and Gas-Liquid-Solid Reactor Engineering, pp. 5895–5916 (cit. on pp. 5–7, 56, 57).

[61]M. T. Kreutzer, F. Kapteijn, J. A. Moulijn, C. R. Kleijn, and J. J. Heiszwolf. “Inertial and interfacial effects on pressure drop of Taylor flow in capillaries”. In: *AIChE Journal* 51.9 (2005), pp. 2428–2440 (cit. on p. 103).

[62]M. T. Kreutzer, M. S. Shah, P. Parthiban, and S. A. Khan. “Evolution of nonconformal Landau-Levich-Bretherton films of partially wetting liquids”. In: *Phys. Rev. Fluids* 3 (1 Jan. 2018), p. 014203 (cit. on pp. 7, 57, 107).

[63]S. Kumari, N. Kumar, and R. Gupta. “Flow and heat transfer in slug flow in microchannels: Effect of bubble volume”. In: *International Journal of Heat and Mass Transfer* 129 (2019), pp. 812–826 (cit. on p. 83).

[64]R. Kurimoto, K. Hayashi, H. Minagawa, and A. Tomiyama. “Numerical investigation of bubble shape and flow field of gas–liquid slug flow in circular microchannels”. In: *International Journal of Heat and Fluid Flow* 74 (2018), pp. 28–35 (cit. on pp. 79, 128).

[65]A. Ładosz and R. P. von Rohr. “Pressure drop of two-phase liquid-liquid slug flow in square microchannels”. In: *Chemical Engineering Science* 191 (2018), pp. 398–409 (cit. on p. 103).

[66]P. Lang, M. Hill, I. Krossing, and P. Woias. “Multiphase minireactor system for direct fluorination of ethylene carbonate”. In: *Chemical Engineering Journal* 179 (2012), pp. 330–337 (cit. on p. 5).

[67]S. S. Y. Leung, Y. Liu, D. F. Fletcher, and B. S. Haynes. “Heat transfer in well-characterised Taylor flow”. In: *Chemical Engineering Science* 65.24 (2010), pp. 6379–6388 (cit. on pp. 5, 56).

[68]R. Lindken, M. Rossi, S. Große, and J. Westerweel. “Micro-Particle Image Velocimetry (μPIV): Recent developments, applications, and guidelines”. In: *Lab Chip* 9 (17 2009), pp. 2551–2567 (cit. on p. 45).

[69]D. Liu, G. Liang, X. Lei, et al. “Highly efficient capillary polymerase chain reaction using an oscillation droplet microreactor”. In: *Analytica Chimica Acta* 718 (2012), pp. 58–63 (cit. on pp. 5, 56).

[70]H. Liu, C. O. Vandu, and R. Krishna. “Hydrodynamics of Taylor Flow in Vertical Capillaries: Flow Regimes, Bubble Rise Velocity, Liquid Slug Length, and Pressure Drop”. In: *Industrial & Engineering Chemistry Research* 44.14 (2005), pp. 4884–4897 (cit. on pp. 14, 56).

[71]X. Liu and J. Katz. “Instantaneous pressure and material acceleration measurements using a four-exposure PIV system”. In: *Experiments in Fluids* 41.2 (May 2006), p. 227 (cit. on p. 23).

[72]Z. Liu, L. Zhang, Y. Pang, X. Wang, and M. Li. “Micro-PIV investigation of the internal flow transitions inside droplets traveling in a rectangular microchannel”. In: *Microfluidics and Nanofluidics* 21.12 (Nov. 2017), p. 180 (cit. on pp. 82, 84).

[73]R. W. Lockhart and R. C. Martinelli. “proposed correlation of data for isothermal 2-phase, 2-component flow in pipes”. In: *Chemical Engineering Progress* 45.1 (1949), pp. 39–48 (cit. on p. 103).

[74]S. Ma, J. M. Sherwood, W. T. S. Huck, and S. Balabani. “On the flow topology inside droplets moving in rectangular microchannels”. In: *Lab Chip* 14 (18 2014), pp. 3611–3620 (cit. on p. 84).

[75]M. Mac Giolla Eain, V. Egan, J. Howard, et al. “Review and extension of pressure drop models applied to Taylor flow regimes”. In: *International Journal of Multiphase Flow* 68 (2015), pp. 1–9 (cit. on p. 103).

[76]M. Magnini, B. Pulvirenti, and J.R. Thome. “Numerical investigation of the influence of leading and sequential bubbles on slug flow boiling within a microchannel”. In: *International Journal of Thermal Sciences* 71 (2013), pp. 36–52 (cit. on pp. 5, 56).

[77]I. V. Makeev, I. Yu. Popov, and R. Sh. Abiev. “Analytical solution of Taylor circulation in a prolate ellipsoid droplet in the frame of 2D Stokes equations”. In: *Chemical Engineering Science* 207 (2019), pp. 145–152 (cit. on p. 83).

[78]D. Malsch, M. Kielpinski, N. Gleichmann, G. Mayer, and T. Henkel. “Reconstructing the 3D shapes of droplets in glass microchannels with application to Bretherton’s problem”. In: *Experiments in Fluids* 55.12 (Nov. 2014), p. 1841 (cit. on pp. 56, 57).

[79]L. Mazutis, J. Gilbert, W. L. Ung, A. D. Griffiths, and J. A. Heyman. “Single-cell analysis and sorting using droplet-based microfluidics”. In: *Nature Protocols* 8 (2013), pp. 870–891 (cit. on p. 5).

[80]C. Meyer, M. Hoffmann, and M. Schlüter. “Micro-PIV analysis of gas–liquid Taylor flow in a vertical oriented square shaped fluidic channel”. In: *International Journal of Multiphase Flow* 67 (2014), pp. 140–148 (cit. on p. 84).

[81]S. Mi, N. T. Weldetsadik, Z. Hayat, et al. “Effects of the Gas Feed on Bubble Formation in a Microfluidic T-Junction: Constant-Pressure versus Constant-Flow-Rate Injection”. In: *Industrial & Engineering Chemistry Research* 58.23 (2019), pp. 10092–10105 (cit. on p. 3).

[82]U. Mießner, T. Helmers, R. Lindken, and J. Westerweel. “An analytical interface shape approximation of microscopic Taylor flows”. In: *Experiments in Fluids* 60.4 (Mar. 2019), p. 75 (cit. on pp. 15, 24, 25, 31, 34, 39, 52, 82, 86, 89, 99, 105, 108, 110, 124, 125).

[83]U. Mießner, T. Helmers, R. Lindken, and J. Westerweel. “μPIV Measurement of the 3D velocity distribution of Taylor droplets moving in a square horizontal channel”. In: *Experiments in Fluids* 61.5 (May 2020), p. 125 (cit. on pp. 16, 35, 104, 105, 108, 109, 124).

[84]P. Miller, K. Danielson, G. Moody, et al. “Matching index of refraction using a diethyl phthalate/ethanol solution for in vitro cardiovascular models”. In: *Experiments in Fluids* 41.3 (Sept. 2006), pp. 375–381 (cit. on p. 35).

[85]M. Mohammadi and K. V. Sharp. “Experimental Techniques for Bubble Dynamics Analysis in Microchannels: A Review”. In: *Journal of Fluids Engineering* 135(2) (2013), pp. 021202 - 021202–10 (cit. on p. 84).

[86]S. Molla, D. Eskin, and F. Mostowfi. “Pressure drop of slug flow in microchannels with increasing void fraction: experiment and modeling”. In: *Lab on a Chip* 11.11 (2011), p. 1968 (cit. on p. 103).

[87]M. Musterd, V. van Steijn, C. R. Kleijn, and M. T. Kreutzer. “Calculating the volume of elongated bubbles and droplets in microchannels from a top view image”. In: *RSC Adv.* 5 (21 2015), pp. 16042–16049 (cit. on pp. 56, 57, 68).

[88]T. L. Narrow, M. Yoda, and S. I. Abdel-Khalik. “A simple model for the refractive index of sodium iodide aqueous solutions”. In: *Experiments in Fluids* 28.3 (Mar. 2000), pp. 282–283 (cit. on p. 35).

[89]R. Nayak, O. J. Lobo, D. Chatterjee, and S. K. Das. “Effect of geometrical parameters on slug behaviour and two phase pressure drop in microchannel T-junctions”. In: *Chemical Engineering and Processing - Process Intensification* 130 (2018), pp. 76–87 (cit. on p. 103).

[90]T. T. Nguyen, Y. Biadillah, R. Mongrain, et al. “A Method for Matching the Refractive Index and Kinematic Viscosity of a Blood Analog for Flow Visualization in Hydraulic Cardiovascular Models”. In: *Journal of Biomechanical Engineering* 126.4 (Sept. 2004), pp. 529–535 (cit. on p. 35).

[91]M. Oishi, H. Kinoshita, T. Fujii, and M. Oshima. “Simultaneous measurement of internal and surrounding flows of a moving droplet using multicolour confocal micro-particle image velocimetry micro-PIV”. In: *Measurement Science and Technology* 22.10 (Aug. 2011), p. 105401 (cit. on p. 84).

[92]M. G. Olsen. “Depth of correlation reduction due to out-of-plane shear in microscopic particle image velocimetry”. In: *Measurement Science and Technology* 21.10 (Sept. 2010), p. 105406 (cit. on p. 45).

[93]M. G. Olsen. “Directional dependence of depth of correlation due to in-plane fluid shear in microscopic particle image velocimetry”. In: *Measurement Science and Technology* 20.1 (Dec. 2008), p. 015402 (cit. on pp. 45, 46, 51).

[94]M. G. Olsen and R. J. Adrian. “Out-of-focus effects on particle image visibility and correlation in microscopic particle image velocimetry”. In: *Experiments in Fluids* 29.1 (Dec. 2000), S166–S174 (cit. on p. 45).

[95]M. Raffel, C. E. Willert, F. Scarano, et al. “Image Evaluation Methods for PIV”. In: *Particle Image Velocimetry: A Practical Guide*. Cham: Springer International Publishing, 2018, pp. 145–202 (cit. on p. 45).

[96]N. Di Miceli Raimondi, L. Prat, C. Gourdon, and P. Cognet. “Direct numerical simulations of mass transfer in square microchannels for liquid–liquid slug flow”. In: *Chemical Engineering Science* 63.22 (2008), pp. 5522–5530 (cit. on p. 83).

[97]S. S. Rao and H. Wong. “The motion of long drops in rectangular microchannels at low capillary numbers”. In: *Journal of Fluid Mechanics* 852 (2018), pp. 60–104 (cit. on p. 78).

[98]O. Robinson and D. Rockwell. “Construction of three-dimensional images of flow structure via particle tracking techniques”. In: *Experiments in Fluids* 14 (Feb. 1993), pp. 257–270 (cit. on pp. 9, 47).

[99]P. A. Romero and A. R. Abate. “Flow focusing geometry generates droplets through a plug and squeeze mechanism”. In: *Lab on a chip* 12.24 (2012), pp. 5130–5132 (cit. on p. 103).

[100]M. Rossi, R. Lindken, and J. Westerweel. “Optimization of multiplane μPIV for wall shear stress and wall topography characterization”. In: *Experiments in Fluids* 48.2 (Feb. 2010), pp. 211–223 (cit. on p. 45).

[101]M. Sauzade and T. Cubaud. “Initial microfluidic dissolution regime of CO_2 bubbles in viscous oils”. In: *Phys. Rev. E* 88 (5 Nov. 2013), p. 051001 (cit. on pp. 8, 70).

[102]H. Schlichting and Kl. Gersten. *Boundary-Layer Theory* -. 10th ed. Berlin, Heidelberg: Springer, 2016 (cit. on p. 18).

[103]R. Seemann, M. Brinkmann, T. Pfohl, and S. Herminghaus. “Droplet based microfluidics”. In: *Reports on Progress in Physics* 75.1 (Dec. 2011), p. 016601 (cit. on p. 5).

[104]L. Shang, Y. Cheng, and Y. Zhao. “Emerging Droplet Microfluidics”. In: *Chemical Reviews* 117.12 (2017), pp. 7964–8040 (cit. on p. 3).

[105]P. Sobieszuk, J. Aubin, and R. Pohorecki. “Hydrodynamics and Mass Transfer in Gas-Liquid Flows in Microreactors”. In: *Chemical Engineering & Technology* 35.8 (2012), pp. 1346–1358 (cit. on p. 57).

[106]T. M. Squires and S. R. Quake. “Microfluidics: Fluid physics at the nanoliter scale”. In: *Rev. Mod. Phys.* 77 (3 Oct. 2005), pp. 977–1026 (cit. on p. 2).

[107]V. van Steijn, C. R. Kleijn, and M. T. Kreutzer. “Flows around Confined Bubbles and Their Importance in Triggering Pinch-Off”. In: *Phys. Rev. Lett.* 103 (21 Nov. 2009), p. 214501 (cit. on pp. 7, 57, 68).

[108]H. A. Stone and L. G. Leal. “Breakup of concentric double emulsion droplets in linear flows”. In: *Journal of Fluid Mechanics* 211 (1990), pp. 123–156 (cit. on p. 59).

[109]T. Taha and Z.F. Cui. “CFD modelling of slug flow inside square capillaries”. In: *Chemical Engineering Science* 61.2 (2006), pp. 665–675 (cit. on pp. 15, 71, 83, 110).

[110]A. Tanimu, S. Jaenicke, and K. Alhooshani. “Heterogeneous catalysis in continuous flow microreactors: A review of methods and applications”. In: *Chemical Engineering Journal* 327 (2017), pp. 792–821 (cit. on pp. 5, 56).

[111]G. I. Taylor. “Deposition of a viscous fluid on the wall of a tube”. In: *Journal of Fluid Mechanics* 10.2 (1961), pp. 161–165 (cit. on p. 2).

[112]T. Tronchin, L. David, and A. Farcy. “Loads and pressure evaluation of the flow around a flapping wing from instantaneous 3D velocity measurements”. In: *Experiments in Fluids* 56.1 (Jan. 2015), p. 7 (cit. on p. 23).

[113]P. Vennemann, K. T. Kiger, R. Lindken, et al. “In vivo micro particle image velocimetry measurements of blood-plasma in the embryonic avian heart”. In: *Journal of Biomechanics* 39.7 (2006), pp. 1191–1200 (cit. on p. 45).

[114]S. V. B. Vivekanand and V. R. K. Raju. “Effect of wall contact angle and carrier phase velocity on the flow physics of gas–liquid Taylor flows inside microchannels”. In: *Chemical Papers* 73.5 (2019), pp. 1173–1188 (cit. on p. 103).

[115]P. M. Vlahovska. “Electrohydrodynamics of Drops and Vesicles”. In: *Annual Review of Fluid Mechanics* 51.1 (2019), pp. 305–330.

[116]X. Wang, A. Riaud, K. Wang, and G. Luo. “Pressure drop-based determination of dynamic interfacial tension of droplet generation process in T-junction microchannel”. In: *Microfluidics and Nanofluidics* 18.3 (2015), pp. 503–512 (cit. on p. 103).

[117]X. Wang, Y. Yong, C. Yang, Z.-S. Mao, and D. Li. “Investigation on pressure drop characteristic and mass transfer performance of gas–liquid flow in micro-channels”. In: *Microfluidics and Nanofluidics* 16.1-2 (2014), pp. 413–423 (cit. on p. 104).

[118]T. Ward, M. Faivre, M. Abkarian, and H. A. Stone. “Microfluidic flow focusing: Drop size and scaling in pressure versus flow-rate-driven pumping”. In: *Electrphoresis* 26.19 (2005), pp. 3716–3724. eprint: `https://onlinelibrary.wiley.com/doi/pdf/10.1002/elps.200500173` (cit. on pp. 5, 103).

[119]J. Westerweel. “Digital particle image velocimetry”. 1993 (cit. on p. 47).

[120]J. Westerweel. “Efficient detection of spurious vectors in particle image velocimetry data”. In: *Experiments in Fluids* 16.3 (Feb. 1994), pp. 236–247 (cit. on p. 47).

[121]J. Westerweel and Fulvio Scarano. “Universal outlier detection for PIV data”. In: *Experiments in Fluids* 39.6 (Dec. 2005), pp. 1096–1100 (cit. on p. 47).

[122]G. M. Whitesides. “The origins and the future of microfluidics”. In: *Nature* 442 (2006), pp. 368–373 (cit. on pp. 2, 5).

[123]A. Wolf, T. Hartmann, M. Bertolini, et al. “Toward high-throughput chip calorimetry by use of segmented-flow technology”. In: *Thermochimica Acta* 603 (2015). Chip Calorimetry, pp. 172–183 (cit. on pp. 5, 56).

[124]K. Xu, C. P. Tostado, J.-H. Xu, Y.-C. Lu, and G.-S. Luo. “Direct measurement of the differential pressure during drop formation in a co-flow microfluidic device”. In: *Lab on a chip* 14.7 (2014), pp. 1357–1366 (cit. on p. 103).

[125]C. Yao, J. Zheng, Y. Zhao, Q. Zhang, and G. Chen. “Characteristics of gas-liquid Taylor flow with different liquid viscosities in a rectangular microchannel”. In: *Chemical Engineering Journal* 373 (2019), pp. 437–445 (cit. on p. 3).

[126]J. Yue, E. V. Rebrov, and J. C. Schouten. “Gas-liquid-liquid three-phase flow pattern and pressure drop in a microfluidic chip: similarities with gas-liquid/liquid-liquid flows”. In: *Lab on a chip* 14.9 (2014), pp. 1632–1649 (cit. on p. 103).

Webpages

[@23]D. Claxton. *Surface Curvature*. 2006. URL: `https://www.mathworks.com/matlabcentral/fileexchange/11168-surface-curvature` (visited on Jan. 23, 2020) (cit. on p. 25).

Acknowledgements

Once there were some particles
their work was hard - plain merciless
I'm grateful, they did their share
Without them most pages 'd be bare
I still would be looking at surfaces

The experimental part of this thesis is the result of more than 4 years of research in the Laboratory for Aero- and Hydrodynamics (AHD) at the Delft Technical University, Netherlands. The modeling work evolved later during my employment at the Department of Environmental Process Engineering (UVT) at the University of Bremen, Germany. Despite authoring this thesis, I cannot regard it to be my work alone. Many people contributed in various ways - directly and indirectly. I would like to thank all of the bright helpful and unique people I was allowed to meet along this admittedly long journey.

First and foremost, I would like to express my deep gratitude to my advisors, Prof. dr. ir. Jerry Westerweel and Prof. Dr.-Ing. Ralph Lindken. Thank you for giving me the opportunity to challenge myself. Without your guidance, sustained advice, untiring support, indispensable knowledge and seemingly endless patience this work would certainly not have been possible. The positive working environment you created in AHD lab, the opportunities to learn and grow, and the provision of an ultimate scientific playground made my work enjoyable and also finally successful.

I am greatful to Prof. Dr.-Ing. Jorg Thöming and Prof. Dr.-Ing. Sven Kerzenmacher, who provided the possibility to continue after the sudden death of

Prof. Dr.-Ing. Räbiger. Without your support, encouragement, advice and especially the provided freedom, I certainly would still be on that journey. Thank you.

I especially am thankful for the invaluable company of Dr.-Ing. Thorben Helmers along the second part my way. From BSc- and MSc- to PhD-Thesis, he quickly grew to be a valuable versatile fellow scientist, whom I shared the joy of discussion and verbal sparring with. His curiosity and questioning have been of great value. The combined proof-reading effort of him and Dr. Stuart Pengelly allowed me to always concentrate on the next step, while still being able to improve the quality of my work substantially.

Since some time has past between commencing my PhD and its finalization, I have the privilege to thank not only one but two working groups. To the people of AHD Lab, who made living worth while at the time: I am grateful for going to BBQ's in the park or at the Delft'se Hout, for going to the beach or the movies, for beer tasting, playing cards, making music and sharing laughter with you. To the people in the UVT-Group, who render work being a very pleasant place: I am grateful for your thoughtfulness, your opinions, your discussions, your stubbornness, your support, your laughter and your enthusiasm.

Finally, I would like to thank my family and friends for their continuous sympathy and support even when time almost faded the necessity to finish what has been started. I am particularly indebted to my mother, who provided me throughout my life with all the love and support she could give.

Saving the best for last, I would like to thank my dear wife, soulmate and favorite human being: Swantje - simply for being there. Your company, patience, love and support is the ground I build upon.

About the author

Ulrich Mießner
born on Wednesday, July 9th, 1975
in Bremen, Germany

since 2010	Senior engineer at the Research Group Environmental Process Engineering (UVT) at the University of Bremen, Germany
2005 - 2009	PhD Student at the Laboratory for Aero- und Hydrodynamic at the TU Delft, Netherlands
1998 - 2005	University of Bremen, candidate for 'Diplom' in Production Engineering
1996 - 1998	Apprenticeship as industrial mechanic at 'Hansestadt Bremisches Amt Bremerhaven'. Maintenance of harbour equipment
1995 - 1996	Civil service at the 'Red Cross' near Bremen as an ambulance-driver. Subsequently completed apprenticeship as paramedic

Journal publications

- Helmers, T., Thöming, J., **Mießner, U.** Retrieving accurate temporal and spatial information about Taylor slug flows from non-invasive NIR photometry measurements. Exp Fluids 58, 160 (2017). https://doi.org/10.1007/s00348-017-2441-8

- **Mießner, U.**, Helmers, T., Lindken, R., Westerweel, J. An analytical interface shape approximation of microscopic Taylor flows. Exp Fluids 60, 75 (2019). https://doi.org/10.1007/s00348-019-2719-0

- Helmers, T., Kemper, P., Thöming, J., **Mießner, U.** Determining the flow-related cap deformation of Taylor droplets at low Ca numbers using ensemble-averaged high-speed images. Exp Fluids 60, 113 (2019). https://doi.org/10.1007/s00348-019-2757-7

- Helmers, T., Kemper, P., Thöming, J., **Mießner, U.** Modeling the Excess Velocity of Low-Viscous Taylor Droplets in Square Microchannels. Fluids 2019, 4, 162. https://doi.org/10.3390/fluids4030162

- Helmers, T., Kemper, P., **Mießner, U.**, Thöming, J. Refractive index matching (RIM) using double-binary liquid–liquid mixtures. Exp Fluids 61, 64 (2020). https://doi.org/10.1007/s00348-020-2892-1

- **Mießner, U.**, Helmers, T., Lindken, R., Westerweel, J. μPIV Measurement of the 3D velocity distribution of Taylor droplets moving in a square horizontal channel. Exp Fluids 61, 125 (2020). https://doi.org/10.1007/s00348-020-02949-z

- **Mießner, U.**, Helmers, T., Lindken, R., Westerweel, J. Experimental investigation of the 3D pressure field of Taylor droplets moving in a

square horizontal microchannel. Exp Fluids 62, 83 (2021). https://doi.org/10.1007/s00348-021-03189-5

- Helmers, T., Kemper, P., Thöming, J., **Mießner, U.** μPIV investigation of the flow-topology transition inside short Taylor droplets moving in square horizontal mircochannels. Exp Fluids (2021) - under review

Conference contributions

- **Miessner, U.**, Coyajee, E., Delfos, R., Lindken, R., Westerweel, J. Experimental investigation of an oil droplet colliding with an oil-water interface, 13th Int. Symp. on Applications of Laser Techniques to Fluid Mechanics, Lisbon, June 26-29, 2006 arXiv:1112.5759

- R. Delfos, E. Coyajee, **U. Miessner**, and J. Westerweel. An oil droplet colliding with an oil-water interface: An experimental flow facility for the validation of numerical simulation data. In Euromech Colloquium 479, Aug. 2006

- **Miessner, U.**, Lindken, R., Delfos, R., Westerweel, J. Untersuchung der Kollision eines Öltropfens mit einer Öl-Wasser Grenzfläche. Proc. of 14. Fachtagung Lasermethoden in der Strömungsmesstechnik, GALA, Braunschweig, Germany, September 5-7, 2006.

- Staicu, A., Bakker, R., **Miessner, U.**, Lindken, R., Westerweel, J., Mugele, F. Electrowetting induced mixing in micro-droplets. FOM-meeting Physics@Veldhoven 2007, PA14.03, Veldhoven, January 23-24 2007.

- **Miessner, U.**, Coyajee, E., Slot, H., Lindken, R., Boersma, BJ., Delfos, R., Westerweel, J. Simulation and experimental validation of an oil droplet colliding with an oil-water interface. FOM-meeting Physics@Veldhoven 2007, P07.11, Veldhoven, January 23-24, 2007

- **Miessner, U.**, Lindken, R., Westerweel, J. Brechungsindexanpassung für Ge-schwindigkeitsmessungen in Mikro-Fluidischen Zwei-Phasen-Systemen, Fachtagung “Lasermethoden in der Strömungsmesstechnik” 4. – 6. September 2007, Rostock

- **Miessner, U.**, Lindken, R., Westerweel, J. Investigation of flow structures in microfluidic two-phase flows. de Nationale MicroNano Conferentie 2007, Wageningen, 15-16 November 2007.
- **Miessner, U.**, Lindken, R., and Westerweel, J. Velocity Measurements in Microscopic Two-Phase Flows by Means of Micro PIV. Proceedings of the ASME 2008 6th International Conference on Nanochannels, Microchannels, and Minichannels. Darmstadt, Germany. June 23–25, 2008. pp. 1111-1118. ASME. https://doi.org/10.1115/ICNMM2008-62093
- **Miessner, U.**, Lindken, R., Westerweel, J. 3D - Velocity measurements in microscopic two-phase flows by means of micro PIV, 14th Int. Symp. on Applications of Laser Techniques to Fluid Mechanics, Lisbon, July2008
- **Miessner, U.**, Lindken, R., Westerweel, J. Simultaneous measurement of the internal circulation of two phases in a micr-channel, Proceedings of the 1st European Conference on Microfluidics - Microfluidics 2008 - Bologna, December 10-12, 2008
- **Miessner, U.**, , Räbiger, N., Lindken, R., Westerweel, J. Three Dimensional Flow Structures in Microfluidic Two-Phase Flows, 1st International Symposium on Multiscale Multiphase Process Engineering (MMPE), 2011

List of Symbols

The following symbols have been used in this thesis. Usually states or origins of the corresponding data is visualized via superscript. Subscript, however, give further information or details on the specified quantity. Symbol above the quantity show mathematical operations like averaging or filtered values.

Acronyms

1D	One dimensional
2C	Two components
2D	Two dimensional
3C	Three components
3D	Three dimensional
μPIV	Micro particle image velocimetry
CFD	Computational fluid dynamics
const	Constant
DMSO	Dimethylsulfoxide
DOC	Depth of correlation
DRIE	Deep reactive ion etching
FF	Flow-focussing
FFT	Fast-Fourier transform
Gly	Glycerin
MD	Measurement depth
MD*	Relative measurement depth
NA	Numerical aperture
PDF	Probability density function
PDMS	Polydimethylsiloxane

PS	Polystyrol
px	Pixel
RI	Refractive index
μPSV	Microscopic particle shadow velocimetry

Dimensionless Quantities

Bo	Bond number
Ca	Capillary number
Mo	Morton number
Oh	Ohnesorge number
Re	Reynolds number

Greek Symbols

α	Volume flow ratio
Δ	Difference
δ	Wall film thickness
η	Dynamic viscosity
Γ	Droplet interface
γ	Shear rate
κ	Curvature
λ	Viscosity ratio
λ_2	Criterion for vortex strength
λ_L	Wavelength of light
Φ	Φ-direction
ρ	Density
σ	Interfacial tension
τ	Shear
θ	Angular coordinate
ε	Disperse phase fraction

Roman Symbols

$\bar{U}$	Mean velocity
$\tilde{y}$	Dimensionless wall distance

$\vec{e}$	Unit vector
$\vec{n}$	Normal vector
A	Area
a	Semi-major axis
A_r	Channel aspect ratio
b	Semi-minor axis
c	Scaling factor of gutter radii ($L_\mathrm{d} < L_{crit}$)
d	Diameter
F	Force
g	Gravitation acceleration
H	Height
I	Intensity
k_b	Back - deformation ratio
k_f	Front - deformation ratio
k_g	Dimensionless gutter radius
L	Length
P	Power
p	Pressure
Q	Volume flow rate
R	Radius
r	Radial coordinate
s	Distance
t	Time
u	Velocity in x-direction
V	Volume
v	Velocity in y-direction
W	Width
w	Velocity in z-direction
x	x-coordinate
y	y-coordinate

z	z-coordinate
f	Frequency
M	Magnification
N	Number of points

Superscripts

$*$	Normalized
0	Superficial
$\perp$	Rotated component
j	Index
k	Index
dyn	Dynamic
max	Maximum
min	Minimum
shift	Shifted
stat	Static

Subscripts

1	Line 1, Fig. 4.1
2	Line 2, Fig. 4.1
3	Line 3, Fig. 4.1
4	Line 4, Fig. 4.1
a	Line a, Fig. 4.1
b	Line b, Fig. 4.1 $\&$ droplet back
i	Index
n	Image control variable
r	Radial direction
x	x-direction
xy	x-y plane at origin
y	y-direction
z	z-direction
zy	z-y plane at origin

c	Continuous phase
cam	Camera
ch	Channel
core	Core of the flow
crit	Critical
d	Disperse phase
drop	Droplet
dyn	Dynamic
f	Droplet front
g	Line g, Fig. 4.1 & gutter
HP	Hagen-Poiseuille
LP	Laplace
mean	Mean value
min	Minimum
p	Tracer particle
pin	Pinhole
rec	Recording
ref	Reference
res	Resulting
stat	Static
theo	Theoretical value
tot	Total

Other Symbols

$\mathcal{K}$	Density ratio
$\mathcal{R}$	Residue
$\mathcal{W}$	Work

Colophon

This thesis was typeset with LaTeX 2$_\varepsilon$. It uses the *Clean Thesis* style developed by Ricardo Langner. The design of the *Clean Thesis* style is inspired by user guide documents from Apple Inc.

Download the *Clean Thesis* style at `http://cleanthesis.der-ric.de/`.

Printing: Ridderprint | www.ridderprint.nl

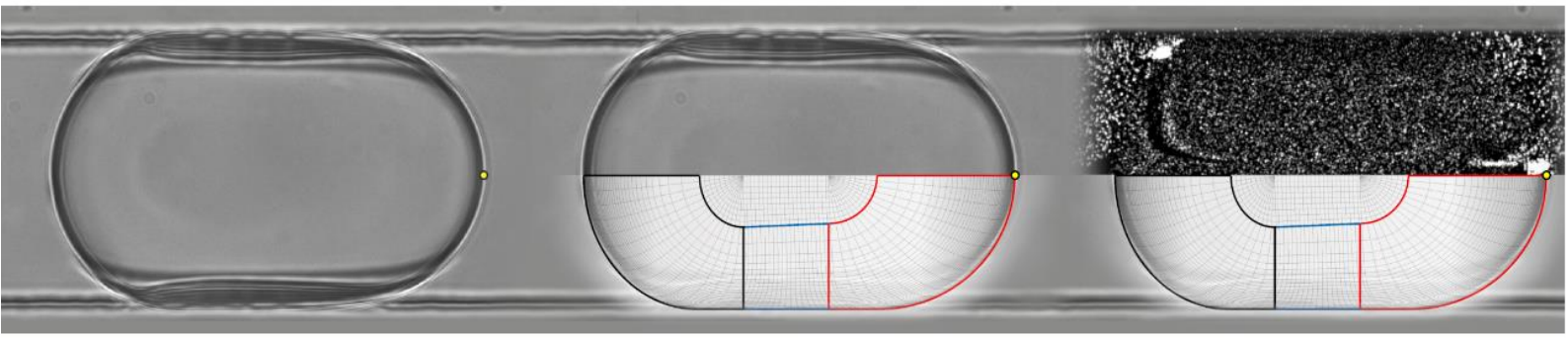

ISBN 978-94-6416-636-1